2006

Molecular simulations of Pd based hydrogen sensing materials

Ling Miao
University of South Florida

Molecular Simulations of Pd Based Hydrogen Sensing Materials

by

Ling Miao

A dissertation submitted in partial fulfillment
of the requirements for the degree of
Doctor of Philosophy
Department of Chemical and Biomedical Engineering
College of Engineering
University of South Florida

Co-Major Professor: Babu Joseph, Ph.D.
Co-Major Professor: Venkat R. Bhethanabotla, Ph.D.
Vinay Gupta, Ph.D.
Martin M. Ossowski, Ph.D.
Brian Space, Ph.D.
Lilia Woods, Ph.D.

Date of Approval:
August 10, 2006

Keywords: Palladium, hydrogen sensor, carbon nanotube, MD simulations, DFT

Dedication

To Sukit, without your constant love and support, none of this would have been possible.

Acknowledgments

The work contained in this dissertation would not be possible without the intellectual support of my advisers, professors, and fellow students. I would like to thank Professor Babu Joseph and Professor Venkat R. Bhethanabotla for their guidance and support that led to a better understanding of this study, and my committee members: Professors Vinay Gupta, Brian Space, Lilia Woods and Dr. Martin M. Ossowski. I am also grateful for the insight provided by my classmates and friends during the course of my studies at USF. I would also like to acknowledge the computational resources provided by USF Academic Computing. As one of the users of their systems, an unlimited time was granted for usage and a great support was provided for any technicial problems, without which, none of this dissertation would be possible. And last but not least, I also thank my parents. Your constant love and support are appreciated and I owe much of my success to you.

Table of Contents

List of Tables iv

List of Figures v

Abstract viii

Chapter One Introduction 1
1.1 Motivation and Goal 2
1.2 Organization of the Thesis 3

Chapter Two Hydrogen Sensor and Sensing Materials 5
2.1 What Is A Sensor? 5
2.2 Hydrogen Sensors 7
2.2.1 Chemiresistor Sensor 7
2.2.2 FET Sensor 8
2.2.3 SAW Sensor 8
2.3 Hydrogen Sensing Materials 10
2.3.1 Catalysis and Sensing 10
2.3.2 Palladium Based Sensor 10
2.3.3 Introduction to Carbon Nanotubes 11
2.3.4 Intrinsic Carbon Nanotube Based Sensor 13
2.3.5 Functionalized Carbon Nanotube Based Sensor 14

Chapter Three Molecular Dynamics Simulation 16
3.1 Equations of Motion for the Atomic Systems 16
3.2 Integrating the Equations of Motion 17
3.3 The Force Calculation 18
3.4 Simulation Convergence 20
3.5 Constraints 20
3.5.1 Thermodynamic Ensembles 20
3.5.2 Temperature Control 21
3.6 Properties Measurement 21
3.7 DL_POLY Package 22

Chapter Four Melting of Pd Clusters and Nanowires: A Comparison Study Using Molecular Dynamics Simulations 23
4.1 Abstract 23
4.2 Introduction 24
4.3 Potential Model and Computational Method 26
4.4 Results and Discussion 28
4.5 Melting Model Comparison 47
4.6 Conclusions 50

Chapter Five Molecular Dynamics Simulations of Graphite Supported Pd Nanocluster Melting 52
5.1 Abstract 52
5.2 Introduction 52
5.3 Potential Model and Computational Method 53
5.4 Results and Discussion 55
5.5 Conclusions 61

Chapter Six Density Functional Theory and the Pseudopotential Method 63
6.1 Density Functional Theory 63
6.1.1 The Hohenberg-Kohn Principle 63
6.1.2 The Self-Consistent Kohn-Sham Equations 64
6.1.3 Approximations for $E_{xc}\left[n(\mathbf{r})\right]$: LDA and GGA 65
6.2 Plane-Wave Basis Set and Pseudopotential 68
6.3 The Vienna *Ab-initio* Simulation Package 70

Chapter Seven Interactions of Hydrogen with Pd and Pd/Ni Alloy Chain Functionalized Single Walled Carbon Nanotubes from Density Functional Theory 71
7.1 Abstract 71
7.2 Introduction 72
7.3 Method of Calculations 74
7.4 Atomic Chain Structures 75
7.5 Chains on SWNTs 79
7.5.1 Pure Pd Chain on SWNT 79
7.5.2 Pd/Ni Alloy Chain on SWNT 85
7.6 H_2 Interactions with Chain-Functionalized SWNTs 89
7.7 Conclusions 96

Chapter Eight DFT Study of Pd Functionalized Carbon Nanotubes as Hydrogen Sensors 98
8.1 Abstract 98
8.2 Introduction 98
8.3 Method of Calculations 100

8.4 Results and Discussion 100
8.5 Conclusion 110

Chapter Nine Conclusions and Proposed Future Work 112
9.1 Conclusions 112
9.2 Major Contributions 114
9.3 Future Work 114
9.3.1 Sensor Poisoning 114
9.3.2 Multipurpose Gas Sensor 115
9.3.3 *Ab initio* MD Simulations 115

References 117

Appendices 133
Appendix A: DL_POLY Programs 134
A.1 The Input Files 134
A.1.1 The CONTROL File 134
A.1.2 The CONFIG File 136
A.1.3 The FIELD File 164
A.2 The Output Files 166
Appendix B: VASP Programs 167
B.1 The Input Files 167
B.1.1 The INCAR File 167
B.1.2 The POSCAR File 169
B.1.3 The POTCAR File 172
B.1.4 The KPOINTS File 172
B.2 The Output Files 173
B.3 Calculate Band Structure 173

About the Author End Page

List of Tables

Table 4-1. Sutton-Chen potential parameters for Pd. 27

Table 4-2. Thermodynamic properties for Pd bulk, cluster and nanowire. 31

Table 4-3. Bond-orientational order parameters for a number of simple cluster geometries. 43

Table 7-1. Binding energy of Pd atoms per unit cell on two SWNTs. 82

Table 7-2. Calculated binding energies, charge transfer, and magnetic moment for Pd/Ni chain-SWNT system. 86

Table 8-1. H_2 adsorption energies E_{ad}, averaged atomic distances $\bar{d}$, averaged nearest neighbor distances $\bar{nn}$, chain angles $\bar{\alpha}$, and magnetic moment μ for Pd radial chain-functionalized SWNT(10,0) systems with different H_2 coverage. 104

List of Figures

Figure 2-1. Schematic diagram of sensor principle. 5

Figure 2-2. Schematic view of a chemiresistor sensor. 8

Figure 2-3. Schematic view of a FET sensor with a SWNT transducer contacted by two electrodes (source and drain) and a silicon bottom gate. 9

Figure 2-4. Schematic view of a SAW sensor. 9

Figure 2-5. Structure of a multi-walled carbon nanotube made up of three shells of different chirality. 12

Figure 2-6. Illustration of zigzag and armchair SWNTs by rolling a graphene sheet. 13

Figure 3-1. The general procedure of leap-frog algorithm. 19

Figure 4-1. Potential energy and heat capacity of the Pd (a) nanocluster and (b) nanowire. 30

Figure 4-2. Radius of gyration vs. temperature for Pd cluster and Pd nanowire with repeating unit of length of 5.6 nm. 32

Figure 4-3. Snapshots of equilibrated atomic positions, shown as projected coordinates in planes parallel (upper) and perpendicular (lower) to (a) the nanowire axis. 34

Figure 4-4. Velocity autocorrelation functions (a) v_θ and (b) v_z for atoms in different shells of the Pd nanowire at 800 K. 36

Figure 4-5. Snapshots of the projected atomic positions of the (a) 456 Pd atom clusters at different T and (b) 1,568 atom Pd nanowire projected on to a plane perpendicular to the axis. 37

Figure 4-6. Self-diffusion coefficient for atoms in different radial shells at various temperatures for (a) Pd cluster and (b) Pd nanowire. 38

Figure 4-7. Comparison of Pd atomic distributions of Pd cluster along a Cartesian coordinate (z) at different temperatures. 41

Figure 4-8. Comparison of Pd atomic distribution along a Cartesian coordinate (z) in the Pd nanowire at (a) 600 K, (b) 1100 K, (c) 1190 K, and (d)1200 K. 42

Figure 4-9. Temperature dependence of average bond-orientational order parameters for (a) the atoms in Pd nanowire and (b) the Pd cluster with 456 atoms and Pd nanowire with 1,568 atoms during heating. 44

Figure 4-10. Correlation plot for bond-orientational order parameters $\hat{W}_6$ as a function of Q_6. 47

Figure 5-1. Potential energy and heat capacity unsupported and graphite-supported Pd clusters vs. temperature (d=2.3 nm). 54

Figure 5-2. Atomic distribution function along z coordinate perpendicular to the graphite substrate. 55

Figure 5-3. Velocity autocorrelation functions of the supported Pd cluster at 1000K. 57

Figure 5-4. Atom coordinates of (a) surface atoms (atoms in shell 1 and 2 as illustrated in Figure 5-3(d)) and (b) inner atoms (atoms in shell 3, 4 and 5) of graphite-supported Pd cluster at 1000 K (blue dots) and 1100 K (red dots). 59

Figure 5-5. (a) Radial distribution function and (b) angular correlation function for Pd clusters. 60

Figure 6-1. Schematic flow-chart for self-consistent density functional calculations. 66

Figure 7-1. Calculated binding energy of Pd and Pd/Ni chain atoms per unit cell as function of length of unit cell d. 76

Figure 7-2. Spin-polarized band structure and DOS of the Pd chains (a-c) and Pd-Ni chains (d-f). 78

Figure 7-3. Schematic drawing of top views of four possible sites for single Pd atom adsorption on SWNT(6,6) and SWNT(10,0). 80

Figure 7-4. 3D view of equilibrium geometries of the Pd chain SWNT structures. 81

Figure 7-5. Spin-polarized band structure and DOS of (a) SWNT(6,6) and (b) Pd narrow angle chain adsorbed SWNT(6,6). 83

Figure 7-6. Spin-polarized band structure and DOS of (a) SWNT(10,0), (b) Pd wide angle chain adsorbed on the bridge-1 sites of SWNT(10,0), and (c) Pd wide angle chain adsorbed on the bridge-2 site of SWNT(10,0). 84

Figure 7-7. 3D views of equilibrium geometries of the Pd/Ni chain-tube structures. 87

Figure 7-8. Spin-polarized band structure and DOS of (a) Pd/Ni narrow angle chain functionalized SWNT(6,6), and (b) Pd/Ni wide angle chain functionalized SWNT(10,0). 88

Figure 7-9. Atom projected density of state (PDOS) from (a) Pd atom with two nearest C atoms and (b) Ni atom with two nearest C atoms, on bridge-2 site functionalized SWNT(10,0). 88

Figure 7-10. Contour plot of total (spin-up and spin-down) valence charge density on three planes for Pd/Ni chain functionalized SWNT(10,0) (upper) and Pd/Ni chain functionalized SWNT(6,6) (lower). 89

Figure 7-11. Contour plot of magnetization density (spin-up and spin-down) on two planes through Pd or Ni and the tube for the same systems as in Figure 7-10. 90

Figure 7-12. 3D views of equilibrium geometries of the H_2 adsorbed Pd and Pd/Ni functionalized SWNTs. 93

Figure 7-13. Band structure and DOS for the four systems shown in Figure 7-12. 94

Figure 8-1. Equilibrium geometries of Pd radial chain-functionalized SWNT(10,0). 101

Figure 8-2. Spin-polarized band structure of (a) bare SWNT(10,0) and (b) Pd radial chain-functionalized SWNT(10,0). 101

Figure 8-3. 3D views of equilibrium geometries of hydrogen adsorbed Pd radial chain-functionalized SWNT(10,0). 103

Figure 8-4. Spin-polarized band structure of hydrogen adsorbed on Pd radial chain-functionalized SWNT(10,0). 105

Figure 8-5. 3D views of equilibrium geometry of Pd fully coated SWNT(10,0). 107

Figure 8-6. Band structure and total spin polarized density of states (DOS) of a Pd fully covered SWNT(10,0). 109

Figure 8-7. Local density of states of two Pd atoms in the fully coated SWNT(10,0). 111

Molecular Simulations of Pd Based Hydrogen Sensing Materials

Ling Miao

ABSTRACT

Hydrogen sensor technology is a crucial component for safety and many other practical concerns in the hydrogen economy. To achieve a desired sensor performance, proper choice of sensing material is critical, because it directly affects the main features of a sensor, such as response time, sensitivity, and selectivity. Palladium is well-known for its ability to sorb a large amount of hydrogen. Most hydrogen sensors use Pd-based sensing materials. Since hydrogen sensing is based on surface and interfacial interactions between the sensing material and hydrogen molecules, nanomaterials, a group of low dimensional systems with large surface to volume ratio, have become the focus of extensive studies in the potential application of hydrogen sensors. Pd nanowires and Pd-coated carbon nanotubes have been successfully used in hydrogen sensors and excellent results have been achieved. Motivated by this fact, in this dissertation, we perform theoretical modeling to achieve a complete and rigorous description of molecular interactions, which leads to the understanding of molecular behavior and sensing mechanisms.

To demonstrate the properties of Pd-based sensing materials, two separate modeling techniques, but with the same underlying aim, are presented in this dissertation. Molecular dynamic simulations are applied for the thermodynamic, structural and dynamic properties of Pd nanomaterials. *Ab initio* calculations are utilized for the study of sensing mechanism of Pd functionalized single wall carbon nanotubes. The studies reported in this dissertation show the applications of computational simulations in the area of hydrogen sensors. It is

expected that this work will lead to better understanding and design of molecular sensor devices.

Chapter One

Introduction

Due to the unusual properties of nanomaterials and their extraordinary performance in various applications, nanotechnology and its many different branches have become a very promising area for research in physics, chemistry, biology and materials science. Nanocluster, nanowire, and carbon nanotube constitute a new class of matter intermediate between atoms/molecules and condensed matter. They are currently the focus of intensive research due to both technological and theoretical interest. New developments in experimental techniques have made it possible to probe the properties of nanomaterials via high resolution spectroscopy. Theoretically, diverse classes of study ranging from *ab initio* calculations through classical simulations to rigorous quantum dynamical investigations have provided a wealth of information concerning the electronic structures, spectroscopic as well as dynamic properties of a variety of nanoparticles.

Among nanomaterials, carbon nanotubes and nanowires are particularly interesting from both fundamental and practical points of view, because of their unique geometric structures and remarkable mechanical, chemical, electronic, magnetic, and transport properties. Their small diameter and long length lead to such large aspect ratios that they both act as ideal one-dimensional systems. All these characteristics make carbon nanotubes and nanowires the focus of extensive studies for potential applications in various sensor devices.

A hydrogen sensor is essential for many purposes, such as industrial process control, combustion control, and in medical applications. Pd (Palladium) is an ideal hydrogen sensing material, because of its unique adsorptive capacity for hydrogen. Since chemical

sensing is based on surface and interface interactions between the analyte molecules and the sensing material, Pd nanomaterials with a large surface/bulk atomic ratio, such as Pd nanowires and Pd functionalized nanotubes, are potentially very efficient hydrogen sensing materials. Hydrogen sensors from highly crystalline Pd nanowire arrays or Pd functionalized carbon nanotube thin films have attracted much interest recently, and it is believed that arrays of thousands of the nanowires or nanotubes could be ultimately used, each tailored to react to a specific species in ambient gases. Therefore a clear understanding of the interaction between sensing material and gas molecules at molecular level is essential to unravel the sensing mechanism and to improve the performance of the sensor, which would ultimately lead to design of more efficient, novel gas sensors.

Computational modeling is a very useful tool in interpreting experimental data and predicting the material behavior through the use of techniques that consider small replications of the macroscopic system with manageable numbers of atoms or molecules. Among all the modeling approaches, Molecular Dynamics (MD) method is a classic simulation technique that calculates the "real" dynamic of the system, from which time averages of properties can be calculated. Density Functional Theory (DFT) method is a quantum approach for the study of structural, electronic properties in materials science. Both of them are valuable means for simulations in the field of chemistry and physics and have greatly contributed to the understanding of various properties of nanomaterials.

1.1 Motivation and Goal

This dissertation is focused on characterizing nanoscaled materials and probing their applications in the field of hydrogen gas sensor using both classical MD simulation method and quantum mechanical DFT calculations. This research aims to unravel the traditional gap between the atomic and the macroscopic world in mechanics and materials by explaining,

exploring and predicting chemical and physical phenomena with aid of the computational tools.

The goal of this research is to study Pd based nanomaterials as hydrogen sensing materials using both classical and quantum computational method. The dissertation is divided into two parts. First, the melting and thermal dynamic properties of Pd nanoclusters and nanowires are studied using MD simulations, with focus on the dynamics and structural evolution during the heating of the systems. This part of work is significant for the characterization of such materials. In the second part, the mechanism of Pd functionalized single walled carbon nanotube and hydrogen interactions are investigated using DFT method, where sensing mechanism is discussed and possible sensing material design is suggested.

1.2 Organization of the Thesis

This dissertation is organized as follows:

- Chapter 2 provides introduction to hydrogen sensors and hydrogen sensing materials, which includes general information of sensor, recent experimental studies and an introduction to carbon nanotubes.
- Chapter 3 describes the MD simulation method used in this study. The theory of the method and the development of computational algorithms employed here are briefly mentioned.
- Chapter 4 discusses the comparison study of thermodynamic, structural and dynamic properties of Pd nanowire and nanocluster. Simulations investigate the similarity and difference of the two systems in the melting process.
- Chapter 5 studies the melting and structural evolution of a graphite supported Pd nanocluster.

- Chapter 6 introduces DFT and pseudopotential plane wave method, as well as the simulation package used.
- Chapter 7 details the electronic study of Pd and Pd/Ni alloy functionalized SWNTs and their interactions with hydrogen molecules.
- Chapter 8 extends the study in the Chapter 7, where different ways of functionalization, including full coating are proposed, and the hydrogen sensing mechanism is explored.
- Chapter 9 summarizes the study contained in this dissertation and suggests possible future studies.

Chapter Two

Hydrogen Sensor and Sensing Materials

2.1 What Is A Sensor?

A sensor is a device or system that produces an output signal in responses to some input quantity, as indicated schematically in Figure 2-1. The input quantity can be physical, chemical or biochemical properties, and the output signal is usually electrical. Sensors are comprised of two basic parts: a sensing element and a transducer. The sensing element is the primary part of a sensor. It interacts with the environment, generates a response, and determines the nature, selectivity and sensitivity of the sensor. The transducer is a device which reads the response of the sensing element and converts it into an interpretable and quantifiable term, such as a voltage signal. Sensors aim at improving the reliability and efficiency of industrial operations by providing faster, more accurate feedback regarding product quality, and also at improving the quality of human life through better information of the environment.

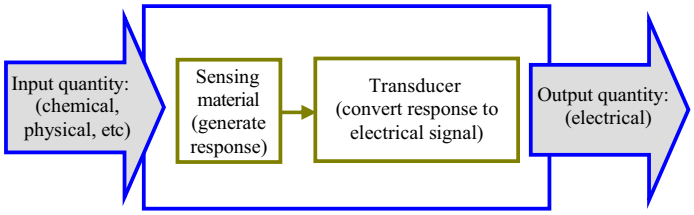

Figure 2-1. Schematic diagram of sensor principle.

Generally, sensors can be classified according to the nature of interaction into the groups [1]:

1. Physical sensors for properties like temperature, pressure, flow, or force;
2. Chemical sensors for specific chemicals or classes of chemicals;
3. Biosensors for biologically active substances.

Another way of classification is to consider the physcial principles and operation mechanism of the sensor, such as electrochemical sensor, mass sensor, acoustic wave sensor, and optical sensor, etc. There are various ways of characterizing a sensor [2, 3]. Some important features include:

- Sensitivity: a measure of magnitude of the output signal produced in response to an input quantity of given magnitude.
- Resolution: a measure of minimum change of input quantity to which the sensor can respond.
- Response time: the length of time required for the output to rise to a specified percentage of its final value.
- Selectivity: the degree to which the sensor can distinguish one input quantity from another.
- Repeatability: the ability of a sensor to reproduce output readings when the same measured value is applied to it consecutively, under same condition.

The rapid development of microelectronics, micromechanics, and other related high technologies enabled the miniaturization of sensor elements, as well as the physical integration of various functions and signal-processing elements onto the same substrate. Nanotechnology, novel materials and smaller, smarter, and more effective electronic systems

are playing an important role in the future of sensors, where higher sensitivity, greater selectivity, lower cost and further miniaturization have become the new wave of senor technology.

2.2 Hydrogen Sensors

Hydrogen is an extremely clean energy source for many purposes. Hydrogen's potential use in fuel and energy applications includes powering vehicles, running turbines or fuel cells to produce electricity, and generating heat and electricity for buildings [4–6]. However, it is explosive when the concentration is above the lower explosion limit in air of 4%. Therefore, safety remains a top priority in all aspects of hydrogen energy. To facilitate hydrogen safety, an important research area is the development of hydrogen sensors to detect leaks and monitor gas purity. In addition, a hydrogen sensor is also a critical component for other practical concerns in the proposed hydrogen economy.

Hydrogen sensor is a typical chemical gas sensor, which upon exposure to a gaseous chemical compound, alters one or more of its physical properties (e.g. mass, electrical conductivity, or capacitance) in a way that can be measured and quantified directly or indirectly. In the past decades, various types of hydrogen sensors have been developed [2]. According to the applied sensing technologies, some of the common sensors for hydrogen detection are: chemiresistor sensors [7, 8], FET (field-effect transistor) sensors [9–11], SAW (surface acoustic wave) sensors [12–14], and fiber optic sensors [15].

2.2.1 Chemiresistor Sensor

Chemiresistor is one of the simplest sensor structures. The schematic drawing of a chemiresistor is shown in Figure 2-2. It consists of a sensing material array or thin film exposed to ambient gases. The adsorption and diffusion of hydrogen into the sensing material result in

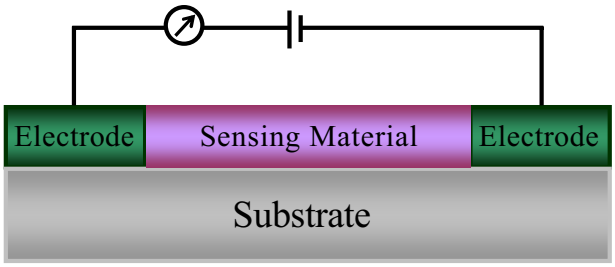

Figure 2-2. Schematic view of a chemiresistor sensor.

the variation of resistance of the device. The change in resistance is directly related to the amount of hydrogen present in the ambient gas.

2.2.2 FET Sensor

The field-effect transistor relies on an electric field to control the conductivity of a semiconductor material, or so-called channel. Most FETs have three terminals, where the output current flowing between the source and drain terminals is controlled by a variable electric field applied to the gate (the third) terminal.

Figure 2-3 gives a schematic drawing of a bottom-gated carbon nanotube FET gas sensor. The sensing material, also called channel, is placed between two metal electrodes, called source and drain. An insulating layer is used to separate sensing material and the silicon gate, which is patterned on an oxidized Si wafer. The gate voltage can be either negative or positive, depending on the nature of the channel, in order to keep the current through transistor constant. In practice, the response is measured when the source-drain current-gate voltage characteristics of the FET device shifts upon hydrogen gas.

2.2.3 SAW Sensor

A SAW device consists of two IDTs (interdigital transducers) of thin metal electrodes on a polished piezoelectric substrate separated by a delay line. The spacing of the IDT fingers

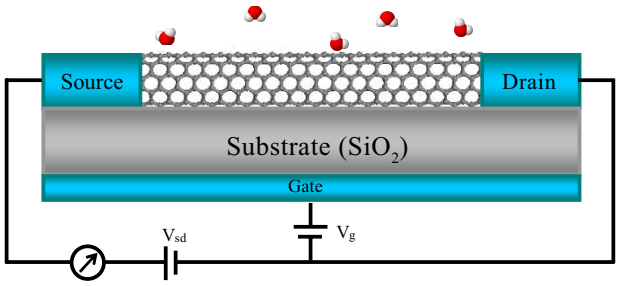

Figure 2-3. Schematic view of a FET sensor with a SWNT transducer contacted by two electrodes (source and drain) and a silicon bottom gate.

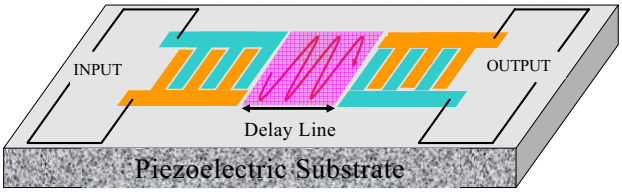

Figure 2-4. Schematic view of a SAW sensor.

determines the wave length. An alternating current applied to one IDT causes the surface to expand and contract. This motion generates surface acoustic waves, known as piezoelectric behavior, propagating across the substrate. Hydrogen reactions with sensing layer between two IDTs cause a frequency, phase, or amplitude shift in the acoustic wave traveling across delay line. These changes are received and converted to electrical signal by the other IDT. The basic structure of the SAW sensor is shown in Figure 2-4.

Unlike the previous two types of sensors, which is affected by resistance or conductance of sensing materials, SAW sensors are mostly based on mass change. However, due to the fact that wave properties depend on many parameters, SAW sensors are not only mass sensitive devices, but also affected by the elasticity, viscosity, and other properties of the sensing layer.

2.3 Hydrogen Sensing Materials

2.3.1 Catalysis and Sensing

Hydrogen detection in solid-state chemical sensors is directly related to the phenomenon of catalysis, which in most cases, are governed by two processes, namely, adsorption and dissociation of molecular hydrogen on the solid surface leading to formation of hydrogen atoms, and diffusion of hydrogen atoms into the bulk. These two processes not only control the response time, but also affect the selectivity in hydrogen detection.

Many group-VIII transition metals, such as Ni, Pd and Pt, have been widely used as in hydrogenation catalytic reactions [16–18] as well as in hydrogen sensors [19], due to the active chemisorption of hydrogen molecules. Among all the transition metals, Pd has been used as the sensing element of a vast majority of hydrogen sensors [2].

2.3.2 Palladium Based Sensor

Pd is an ideal material for hydrogen sensing because it is able to selectively absorb large quantities of hydrogen gas and forms a chemical species known as Pd hydride [20]. The measured diffusivity of hydrogen in Pd indicates that it is orders of magnitude larger than diffusivities of other gases. Because of the selectivity to hydrogen adsorption, Pd has been employed as a filter for hydrogen purification, and also has been used to provide hydrogen selectivity for various hydrogen detectors [20].

The response time for a Pd based hydrogen sensor is determined by the rate at which the Pd element equilibrates with hydrogen in the contacting gas phase [2]. Since the equilibration of pure Pd with hydrogen gas involves the fast dissociative adsorption at the Pd surface and relatively slower diffusion rate ($\sim$107 cm^2/s) [20] for hydrogen atoms into the Pd lattice, the diffusion process, not the adsorption process, tends to be rate-limiting. In principle, by reducing the thickness or the dimension of Pd sensing material, the equilibra-

tion time can be reduced, and the response of the sensor to hydrogen accelerated. Therefore, to achieve a fast response while increasing the sensitivity, nanometer sized Pd materials, such as Pd thin film, nanoclusters and nanowires are commonly applied in the current development of hydrogen sensors. Nanocluster or nanowire is a cluster of atoms/molecules or an extremely thin wire with a diameter on the order of a few nanometers or less. Due to the low dimensionality and special geometry, they have large surface/volume ratio and exhibit many chemical and physical properties different from the bulk. Hydrogen sensors fabricated from these materials have shown a significant improvement in response time, as well as sensitivity compared to the corresponding conventional Pd sensors [8, 21–23]. In addition, using nanomaterials also greatly facilitates sensor miniaturization and meet the requirement of a new generation hydrogen sensors that uses smallest sample and has lowest weight, power consumption and cost.

2.3.3 Introduction to Carbon Nanotubes

Carbon nanotubes were discovered in 1991 by Iijima during the direct current arching of graphite for the preparation of fullerenes [24]. Such self-assembled nanoscale tubular structures of carbon atoms can be obtained by rolling graphene sheets with various chiralities. A carbon nanotube can be either single walled (SW) or multi walled (MW), for example, double walled or triple walled as shown in Figure 2-5, depending on the number of graphene layers that is required to roll up a carbon tube [24, 25].

The chirality and diameter of a single walled SWNT are uniquely specified by the vector $\mathbf{c}_h$ shown in Equation 2-1,

$$\mathbf{c}_h = n_1\mathbf{a}_1 + n_2\mathbf{a}_2 \equiv (n_1, n_2) \tag{2-1}$$

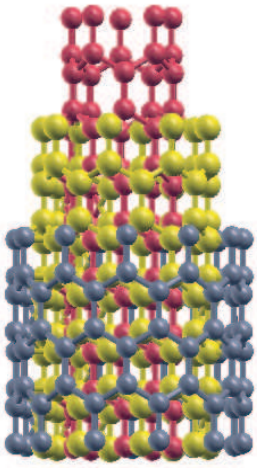

Figure 2-5. Structure of a multi-walled carbon nanotube made up of three shells of different chirality.

where n_1, n_2 are integers and a_1, a_2 the unit vectors of graphite, as shown in Figure 2-6. The SWNT is formed by connecting together the two crystallographically equivalent sites on the $\mathbf{c}_h$ vector [26]. The tube diameter d is defined by Equation 2-2.

$$d = |\mathbf{c}_h| / \pi = a\sqrt{{n_1}^2 + n_1 n_2 + {n_2}^2}/\pi \tag{2-2}$$

where a=1.42$\times\sqrt{3}$ Å is the lattice constant.

According to orientation for vector $\mathbf{c}_h$, carbon nanotubes can be categorized into three types:

1. armchair nanotubes: (n_1,n_2)=(n,0), n is an integer.
2. zigzag nanotubes: (n_1,n_2)=(n,n).
3. chiral nanotubes: all others.

Because of the symmetry and unique electronic structure of graphene, the chirality of a nanotube strongly affects it electrical properties. For a given SWNT(n_1,n_2), if $2n_1$+n_2=3q,

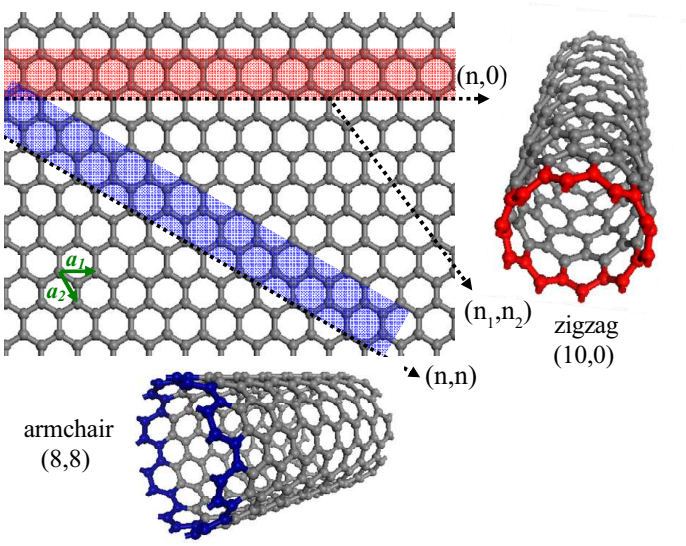

Figure 2-6. Illustration of zigzag and armchair SWNTs by rolling a graphene sheet.

then the nanotube is metallic, otherwise it is a semiconductor [26]. Experimentally, carbon nanotubes can be synthesized by laser vaporization, electric arc discharge, hydrocarbon vapor growth, and others [27]. Carbon nanotubes have many extraordinary properties, such as high modulus and strength, high chemical and thermal stabilities, and remarkable electronic and heat conduction [27]. These properties, together with the one-dimensional character make carbon nanotubes the perfect candidates for various next-generation micro electronic devices.

2.3.4 Intrinsic Carbon Nanotube Based Sensor

The discovery of carbon nanotubes has generated keen interest among researchers to develop carbon nanotubes sensors for many applications. Carbon nanotubes have been demonstrated to be promising nanoscale molecular sensors for detecting gas molecules with fast response time and high sensitivity at room temperature [28, 29]. Upon exposure to gaseous molecules, such as NO_2, NH_3 or O_2, the electrical resistance of the carbon nanotube is found to dramatically increase or decrease, which serves as the basis for nanotube molecu-

lar resistor sensor. These response were attributed to charge transfer between semiconducting SWNT surface and gas molecules.

However, the range of molecules that can be detected by intrinsic carbon nanotubes is very limited [25, 30–35]. Many important gases, such as H_2, CO, CH_4 and H_2O do not adsorb on the carbon nanotube surface. To overcome these limitations of intrinsic carbon nanotube as a sensing material, diverse external or internal functionalization schemes are used.

2.3.5 Functionalized Carbon Nanotube Based Sensor

The idea of functionalizing carbon nanotube is attractive because it allows persistent alteration of electronic properties of the tubes, as well as to chemically tailor their surface properties, whereby new functions can be implemented that can't otherwise be acquired by intrinsic carbon nanotubes. Functionalization process introduces additional chemical elements or groups to intrinsic carbon nanotube through doping, coating or chemical modification and solubilization [36, 37]. Experimentally, functionalized carbon nanotubes can be characterized by various techniques such as X-ray diffraction, ultraviolet (UV)/infrared (IR) spectroscopy, Raman spectroscopy, nuclear magnetic resonance (NMR), electron spin resonance (ESR), and so on [37].

The modification of carbon nanotube sidewalls with nanoparticles made of suitable metals has shown potential applications in sensors. In 2001, Kong *et al.* showed that excellent molecular hydrogen sensors can be enabled by electron-beam evaporation of Pd nanoparticles over the SWNT sidewall [22]. Pd modified SWNT samples exhibit significant electrical conductance modulation upon exposure to small concentration of H_2 in air at room temperature, showing Pd functionalized SWNT sensor has high sensitivity and fast response. Following this work, the Pd layer deposited SWNT films were fabricated and good sensitivity to H_2 with fast recovery and low power consumption were also demon-

strated [38, 39]. In addition to hydrogen detection, Pd coated SWNTs have been reported to be used as sensitive and recyclable methane sensor [40]. It is believed that SWNTs can be doped with other catalytic metals, thereby extending the range of gases the sensor can detect. Furthermore, a sensor device comprising more than one such SWNT doped by different chemicals is expected to respond to multiple molecular species at the same time.

Chapter Three

Molecular Dynamics Simulation

Vast majority of experimental techniques measure molecular properties as averages, either time averages or ensemble averages or both. Thus we seek computational techniques capable of accurately reproducing these aspects of molecular behavior. The focus of this chapter is on the brief overview of classical molecular dynamics (MD) simulation technique for the simulation of real systems.

3.1 Equations of Motion for the Atomic Systems

Classical molecular dynamics simulation is a technique for computing the equilibrium and transport properties of a classical many-body system, where the positions and velocities of atoms are allowed to evolve according to the Newtonian equation of motion shown in Equation 3-1 [41].

$$\nabla_i E_p(\mathbf{r}_1, \mathbf{r}_2, ..., \mathbf{r}_N) = m_i \frac{d^2\mathbf{r}_i}{dt^2} = m_i \frac{d\mathbf{v}_i}{dt},\ i = 1, 2, ..., N \tag{3-1}$$

Here, $\mathbf{r}_i$, $\mathbf{v}_i$, m_i and is the position, velocity and mass of atom i. E_p is the potential energy. The total energy is the sum of the potential energy E_p and kinetic energy E_k. The kinetic energy of the atoms determines the temperature of the system using Equation 3-2.

$$\langle E_k \rangle = \frac{3}{2}(N-1)k_B T \tag{3-2}$$

where k_B is Boltzman's constant. The angle brackets denote the ensemble average over all atoms in the systems.

To do a MD simulation, three things are required: the potential $E_p(\mathbf{r}_i)$, the positions $\mathbf{r}_i$, and the velocities $\mathbf{v}_i$. The particle initial positions should be chosen compatible with the structure that is aimed to simulate. The initial distribution of velocities are usually determined from a random distribution, for instance Maxwell-Boltzmann or Gaussian distribution, with the magnitudes conforming to the required temperature and corrected so there is no overall momentum.

3.2 Integrating the Equations of Motion

The differential equations of motion are integrated numerically according to which the particle positions or both positions and velocities are updated. The commonly applied methods are Verlet algorithm [42] and its modifications [43]. Verlet algorithm is a combination of two Taylor expansions for position from time t forward or backward to $t + \delta t$ or $t - \delta t$ according to Equation 3-3 and 3-4.

$$\mathbf{r}(t+\delta t) = \mathbf{r}(t) + \frac{\partial \mathbf{r}(t)}{\partial t}\delta t + \frac{1}{2}\frac{\partial^2 \mathbf{r}(t)}{\partial t^2}\delta t^2 + \frac{1}{3!}\frac{\partial^3 \mathbf{r}(t)}{\partial t^3}\delta t^3 + ... \tag{3-3}$$

$$\mathbf{r}(t-\delta t) = \mathbf{r}(t) - \frac{\partial \mathbf{r}(t)}{\partial t}\delta t + \frac{1}{2}\frac{\partial^2 \mathbf{r}(t)}{\partial t^2}\delta t^2 - \frac{1}{3!}\frac{\partial^3 \mathbf{r}(t)}{\partial t^3}\delta t^3 + ... \tag{3-4}$$

The new positions $\mathbf{r}(t + \delta t)$ are obtained by adding these two expansions shown in Equation 3-5.

$$\mathbf{r}(t+\delta t) = 2\mathbf{r}(t) - \mathbf{r}(t-\delta t) + \delta t^2 \mathbf{a}(t) \tag{3-5}$$

where **a** are accelerations. The current velocities are then derived from trajectory of previous and next time steps according to Equation 3-6.

$$\mathbf{v}(t) = \frac{\mathbf{r}(t+\delta t) - \mathbf{r}(t-\delta t)}{2\delta t} \tag{3-6}$$

Another equivalent scheme is so-called half step Leap Frog algorithm. In this algorithm, the stored quantities are the current positions $\mathbf{r}(t)$, accelerations $\mathbf{a}(t)$ together with the half-step velocities $\mathbf{v}(t - \frac{1}{2}\delta t)$. The future positions $\mathbf{r}(t+\delta t)$ and the velocities at $\mathbf{v}(t + \frac{1}{2}\delta t)$ are calculated from Equation 3-7 and 3-8.

$$\mathbf{r}(t+\delta t) = \mathbf{r}(t) + \delta t \mathbf{v}\left(t + \frac{1}{2}\delta t\right) \tag{3-7}$$

$$\mathbf{v}\left(t + \frac{1}{2}\delta t\right) = \mathbf{v}\left(t - \frac{1}{2}\delta t\right) + \delta t \mathbf{a}(t) \tag{3-8}$$

The current velocities are calculated using Equation 3-9.

$$\mathbf{v}(t) = \frac{1}{2}\left(\mathbf{v}\left(t + \frac{1}{2}\delta t\right) + \mathbf{v}\left(t - \frac{1}{2}\delta t\right)\right) \tag{3-9}$$

The term leap-frog reflects the positions being evaluated at t and the velocities at $t \pm \frac{1}{2}\delta t$.The general procedure of leap-frog algorithm is shown in Figure 3-1

3.3 The Force Calculation

No matter which algorithm is used, at each step, the force **F** on each atom must be calculated by differentiating the potential function, $E_p(\mathbf{r})$ using Equation 3-10.

$$\mathbf{F}(\mathbf{r}) = -\frac{dE_p(\mathbf{r})}{d\mathbf{r}} \tag{3-10}$$

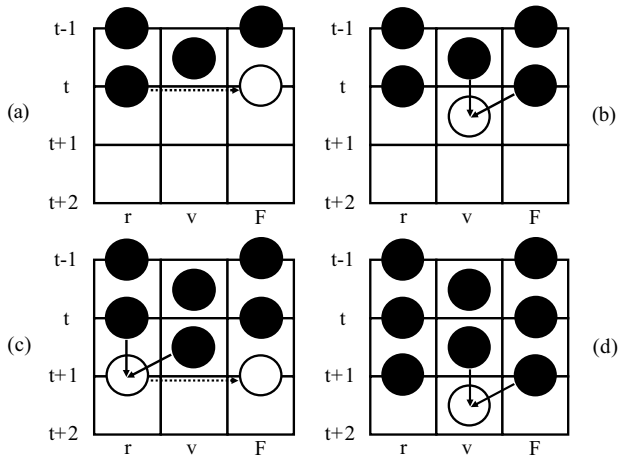

Figure 3-1. The general procedure of leap-frog algorithm. Briefly, (a) knowing the positions at time step t, one computes all of the forces. (b) Equation 3-8 is then used with the known force at step t and known velocities at step $t - \frac{1}{2}\delta t$ to advance the velocity to the next half step $t + \frac{1}{2}\delta t$. (c),(d) Equation 3-7 is then used to compute the position at time step $t + 1$ and the procedure repeats.

The potential energy function decides or approximates the interactions between all atoms in the system. In principle, potential function could be solved from the electronic structure of the atom, but if a complex system is involved, the Born-Oppenheimer approximation is applied where only nuclear motion are considered [43]. The potential function used in this research will be briefly introduced in the later chapter.

Typically potential energies decay rapidly with distances, therefore they are truncated outside a primary cutoff radius, r_c. In MD simulations, a second, larger cutoff radius, r_v, is introduced, and all neighbors separated by less than r_v are stored. This neighbor list is called Verlet list [42], which will only be updated if the maximum displacement of the particles is larger than $r_v - r_c$, thus the computational time is saved when the interactions are calculated.

3.4 Simulation Convergence

After the forces are computed, the future positions are determined, and the trajectories are updated. In order to know whether the system is running well, one should check that monitored quantities are in fact evolving in time. The convergence of the simulation can be demonstrated by calculation of energy, root-mean-square deviation (RMSD) or correlation function between two variables [43, 44]. If the quantities are "constant" over time with an acceptably small fluctuation, the system is then converged, or, in other word, equilibrated. Thermodynamic properties and other quantities can then be calculated after equilibration to analyze the results.

3.5 Constraints

To compare simulations and experiments, one needs to control and measure thermodynamic properties. The common constraints are thermodynamic variables that can be controlled in physical experiment, such as number of particles (N), temperature (T), pressure (P), volume (V) and energy (E). In simulation, these variables can also be controlled. Some methods used in this study are introduced below.

3.5.1 Thermodynamic Ensembles

An ensemble is a collection of all possible systems which have different microscopic states but have an identical macroscopic or thermodynamic state [45]. There exist different ensembles with different characteristics. For example, canonical ensemble has constant N, V and T, microcanonical ensemble has constant N, V and E. In the dissertation, NVT ensemble is employed. N and V are easily controlled in MD simulation by fixing the number of atoms and volume of the simulation box. T can be controlled by applying a thermostat to ensure the average system temperature is maintained close to the set temperature.

3.5.2 Temperature Control

The temperature calculated from the atomic velocities can be controlled by the Berendsen weak coupling technique, where the system is coupled to an external heat bath [46]. In MD simulations, this corresponds to adding frictional terms to the equation of motion shown in Equation 3-11.

$$m_i \frac{d\mathbf{v}_i}{dt} = \mathbf{F}_i + \frac{m_i}{2\tau_T}\left(\frac{T_0}{T} - 1\right)\mathbf{v}_i \tag{3-11}$$

τ_T is the coupling time constant that determines the strength of coupling and T_0 is the set temperature [46]. By choosing different values of T_0, the strength of the coupling can be made smaller to minimize the disturbance to the system, or it can be varied depending on the application. This method also has an advantage of maintaining a Maxwell type velocity distribution.

3.6 Properties Measurement

The basic thermodynamic properties can be calculated as time averages $\langle A \rangle_{time}$ from MD simulations after the system is equilibrated. That is, the average value of the property A over all time steps generated by the simulation in the production time according to Equation 3-12.

$$\langle A \rangle_{time} = \lim_{x\to\infty} \frac{1}{\tau} \int_{t_0}^{x+t_0} A\left(\mathbf{p}^N(t), \mathbf{r}^N(t)\right) dt \approx \frac{1}{M} \sum_{i=1}^{M} A_i\left(\mathbf{p}^N(t_i), \mathbf{r}^N(t_i)\right) \tag{3-12}$$

where τ is the simulation time, M is the number of time steps in the simulations, and A_i is the instantaneous value of A, expressed as a function of the momentum **p**, and the positions

r of the system. The ergodic hypothesis assumes $\langle A \rangle_{time}$ is independent of choice of t_0, and equivalent to ensemble average $\langle$A$\rangle$ in most molecular simulations [44].

3.7 DL_POLY Package

All the MD simulations in this dissertation are performed by DL_POLY, a parallel molecular simulation package developed at Daresbury Laboratory [47]. DL_POLY includes density dependent potentials suitable for calculating the properties of metals, such as Sutton-Chen potential used in the calculations [48]. The equation of motion integration algorithms in DL_POLY are based on Verlet scheme. DL_POLY also provides a multiple timestep algorithm to improve efficiency [49]. A brief description of how to set up a MD simulation for one particular system using DL_POLY can be seen in Appendix A.

Chapter Four

Melting of Pd Clusters and Nanowires: A Comparison Study Using Molecular Dynamics Simulations

* A portion of this chapter has been published in the *Physical Review B* 72, 134109, 2005

4.1 Abstract

We present results from a molecular dynamics simulation study of a Pd cluster and a nanowire, using the Sutton-Chen many body potential function. Changes in thermodynamic and structural properties of these two systems during heating were studied. We found that the melting temperature of the Pd nanowire of 1200 K is lower than the simulated bulk value (1760 K) but higher than that of the cluster at 1090 K. Melting behaviors were characterized by a number of thermodynamic, structural and dynamical parameters. Surface pre-melting at much lower temperatures than the near first-order transition temperatures noted above was observed in both Pd systems. The surface pre-melting temperature range was higher for the nanowire than for the cluster. Surface melting in nanowires manifests itself as large amplitude vibrations followed by free movement of atoms in the plane perpendicular to the nanowire axis, with axial movement arising at temperatures closer to the transition temperature. Increase in nanowire diameter as well as shape change is seen to result from this axial mixing. Bond-orientational order parameters indicated that the nanocluster retained the initial fcc structure at low temperatures. The nanowires, however, were seen to be stable at a solid structure that was close to hcp as established by bond-orientational order parameter calculations. Melting point depressions in both systems agree better with a liquid-drop model than with Pawlow's thermodynamic model.

4.2 Introduction

Studies of the melting process and thermodynamics properties of particles at nanometer length-scales have attracted both theoretical [50, 51], and experimental [51–53] interest because of their dramatically different behavior from bulk materials [54]. For example, it has been known that the melting temperature decreases with decreasing diameter of clusters [55]. Transition and noble metal [56–58] or alloy [59, 60] clusters and nanowires are getting more attention, mainly because of their extensive applications in catalysis and in electronic and opto-electronic nanodevices. However, many properties such as size, shape, and structure of nanomaterials affect their catalytic, optical and electronic properties in ways that are difficult to predict [61]. Experimentally, they have been studied using imaging [61–63] and spectroscopic [64, 65] methods. For example, recent advances in in-situ transmission electron microscope (TEM) techniques have allowed direct investigation of nanoparticles under realistic reaction conditions at atomic level [66]. Theoretically, the use of modeling and simulations has also substantially improved our understanding of nanomaterials in various applications. Theoretical investigations of the melting behavior of clusters and nanowires have been mostly by means of Monte Carlo (MC) and Molecular Dynamics (MD) computer simulations and are focused on the followings aspects:

1. Investigation of the melting temperature and thermal stability during the melting process [67, 68].

2. The structural evolutions and mechanical properties during heating [69].

3. Relationship of structural characteristics and size effects with temperature [50, 70, 71].

For example, Wang *et al.* found that for Ti nanowires thinner than 1.2 nm, there is no clear characteristic of first-order phase transition during the melting, but a coexistence of

the solid and liquid state does exist [68]. Liu *et al.* observed three characteristic time periods in the melting of gold isomers: disordering and reordering, surface melting, and overall melting [72]. Lee and co-workers used the potential energy distribution of atoms in clusters to explain many phenomena related to the phase changes of clusters, and also found a new type of pre-melting mechanism in Pd_{19} cluster [73].

Clusters are often considered as a bridge between individual atoms and bulk material. Recent experimental and theoretical studies demonstrated that metallic nanowires have helical multi-walled cylindrical structures which are different from those of bulk and clusters [74]. However, at the same time, nanowires also have some thermodynamic characteristics which are similar to either clusters or bulk, because of the large surface-to-volume ratio in these nanostructures. Therefore, a comparison of clusters and nanowires can provide an opportunity to better understand their behavior.

In this paper, melting characteristics of palladium nanoclusters and nanowires of comparable size are described. Pd nanoclusters and nanowires have been used widely in the design of high performance catalysts [75, 76] and nanoscale electronic devices, such as chemical sensors [7, 8, 22]. Several experiments clearly indicate that quantum behavior of metal nanoclusters is observable, and is most strongly expressed between 1 and 2 nm, therefore, particles in that size region should be of most interest [77]. For example, Volokitin *et al.* found that 2.2 nm Pd clusters show the most significant deviations from bulk behavior at very low temperatures compared with those of 3.0, 3.6 and 15 nm diameter [78]. Simulation study of Pd nanomaterial provides an opportunity for further understanding its unique role in experimental phenomena. Although the size of the metallic clusters being studied in the literature ranges from tens to several thousand atoms, most efforts have been focused on sizes below 150 atoms for both Pd and other metals [79]. To facilitate comparison with experimental data, we investigate both melting and structural behavior of the Pd cluster with 456 atoms and comparable-sized nanowire with 1,568 atoms.

4.3 Potential Model and Computational Method

Because of the delocalized electrons in metals, the potential functions, which describe the interactions of particles, should account for the repulsive interaction between atomic cores as well as the cohesive force due to the local electron density. Several many-atom potential models were developed during the 1980s by various workers, such as the Embedded Atom Model [80], the Glue Model [81], Tight-binding potential with a second-momentum approximation (TB-SMA) [82], and Sutton-Chen potential model [48], which was used in our MD simulation. The Sutton-Chen potential can be used to describe the interaction of various metals, such as Ag, Au, Ni, Cu, Pd, Pt, and Pb. It is expressed as a summation over atomic positions using Equation 4-1.

$$U = \varepsilon_{pp} \sum \left(\frac{1}{2} \sum_{j \neq i}^{N} \left(\frac{\sigma_{pp}}{r_{ij}} \right)^{n} - c\sqrt{\rho_i} \right) \tag{4-1}$$

where $\rho_i = \sum_{j \neq i}^{N} \left(\frac{\sigma_{pp}}{r_{ij}} \right)^{m}$ is a measure of the local particle density. Here r_{ij} is the separation distance between atoms, c is a dimensionless parameter, ε_{pp} is the energy parameter, σ_{pp} is the lattice constant, and m and n are positive integers with $n>m$. The first term of Equation 4-1 is a pair-wise repulsive potential, and the second term represents the metallic bonding energy between atomic cores due to the surrounding electrons. Therefore, it has the same basis as the Finnis-Sinclair potential and introduces an attractive many body contribution into the total energy. This potential can reproduce bulk properties with remarkable accuracy [83]. It provides a reasonable description of small cluster properties for various transition and noble metals [84, 85]. SC potential has also been applied to model the interaction and study the properties of bimetallic alloys and metal/substrate systems [60, 86, 87]. Recently, adsorbate effect of supported Pt nanoclusters was studied using the SC potential and it was found that the presence of adsorbed atoms stabilizes the surface cluster atoms

Table 4-1. Sutton-Chen potential parameters for Pd.

σ(Å)	$\varepsilon(10^{-3}$ eV)	c	n	m
3.8907	4.179	108.27	12	7

under an inert gas atmosphere [88]. Values of SC parameters for Pd simulations in this paper were taken from the original work of Sutton and Chen, as listed in Table 4-1 [48].

MD simulations were performed using the DL_POLY package [47]. The system was simulated under canonical (NVT) ensemble using the Verlet leapfrog algorithm [89]. Periodic boundary conditions were applied only in the axial direction of the nanowire. No boundary conditions were applied to the cluster. The bulk systems were studied with 3D periodic boundary conditions under constant pressure and temperature (NPT). Both cluster and nanowire were started from face-centered cubic (fcc) Pd bulk structure. A cutoff diameter of 2.3 nm is used to generate a spherical Pd cluster and cylindrical nanowire. This cutoff diameter is not the best way to specify the particle diameter. For the spherical cluster, the Guinier equation shown in Equation 4-2 provides a methodology for estimating the actual radius of the cluster [68].

$$R_{cluster} = R_g\sqrt{5/3} + R_{Pd} \tag{4-2}$$

where the first term is derived by equating the Rayleigh equation and an equation resulting from the Guinier approximation for particle scattering [90, 91]. R_g is the radius of gyration, given by Equation 4-3.

$$R_g = \sqrt{\frac{1}{N}\sum_i \left(R_i - R_{cm}\right)^2} \tag{4-3}$$

where R_i-R_{cm} is the distance from center to the coordination point, and the sum runs over all particles. The second term in equation 2 is half the atomic distance in the Pd bulk,

R_{Pd}=1.37 Å. The resulting diameter calculated from Equation 4-2 is about 2.6 nm, which is taken to be the diameter of the cluster in later calculations. The same 2.6 nm is taken to be the nanowire diameter.

In all the simulations reported here, a time step of 0.001ps was used. The initial samples with atoms in ideal face centered cubic (fcc) positions were first relaxed by simple quenching to 0 K. Each system was then heated with a temperature step of 50 K. The step-size was decreased to 10 K when close to the transition temperature.

4.4 Results and Discussion

The temperature of melting transition can be identified in many ways. We first employ the variations of total potential energy and heat capacity during heating. They are shown in Figure 4-1. Potential energies increase linearly with temperature in the early stage, but deviate from the linear dotted lines at higher temperatures. These deviations, associated with surface melting phenomena, will be discussed later. When close to the transition temperature, simple jumps in total potential energy, indicative of near first-order transitions, can be easily observed. Upon cooling, both the nanocluster and nanowire undergo sharp liquid-solid transitions and show rather strong hysteresis. The potential energies of the new solids are not very different from the initial ones, though structural differences are bound to prevail. We focus on the melting process in this contribution, and take the sharp jump in the energy (and the corresponding sharp peak in the heat capacity) to represent the melting temperature. Consistent with literature, we defined the melting point as the transition temperature corresponding to the temperature of observed phase change in the heating run, and the freezing point as the temperature of observed phase change in the cooling run. The presence of hysteresis in melting/freezing transition is not unusual and is expected both theoretically [92, 93] and experimentally, as reported in the cases of Pb [94] and Na [51]. The structural changes resulting from cooling and heating also influence the

phase transition and result in hysteresis as reported by Chausak and Bartell in their study on freezing of Ni-Al bimetallics [95]. From the potential energy curve, we estimate the melting transition of Pd cluster to occur at 1090 K, and that of the Pd nanowire at 1200 K. Both temperatures are much lower than the bulk melting temperature of 1760 K (also obtained from simulation).

The constant-volume specific heat capacity C_v is calculated by a standard formula shown in Equation 4-4.

$$C_v = \frac{\langle (\delta E)^2 \rangle}{k_b T^2} = \frac{\langle E^2 \rangle - \langle E \rangle^2}{k_b T^2} \tag{4-4}$$

where E is total potential energy from the heating curve of Figure 4-1, k_b is the Boltzman constant, and T is the temperature. Melting point is defined as the temperature with the maximum apparent heat capacity. The C_v curves in Figure 4-1(a) and (b) indicate the same melting temperatures as those from E_p curves. Compared to the C_v curve before melting for the Pd cluster, that of Pd nanowire shows more structure. We also observe a small upward jump in the nanowire heating curve, after which the slope increases quickly until the large jump appears. This deviation from linearity is a result of surface melting [96] or surface reconstruction [97], which implies that the melting process takes place in two stages, pre-melting and homogeneous melting. Even though this change is clearly visible from the plot for the Pd cluster, further characterization of the surface melting via dynamical variables such as the diffusion behavior and velocity auto-correlation functions revealed differences in the details of the pre-melting. These characterizations are discussed later in this paper. Based on the data shown in Figure 4-1, we can estimate the melting temperature to be 1090 K for the Pd cluster, and 1200 K for the infinitely long nanowire.

Using the above melting temperatures, the heat of fusion of Pd cluster and nanowire can be obtained using Equation 4-5.

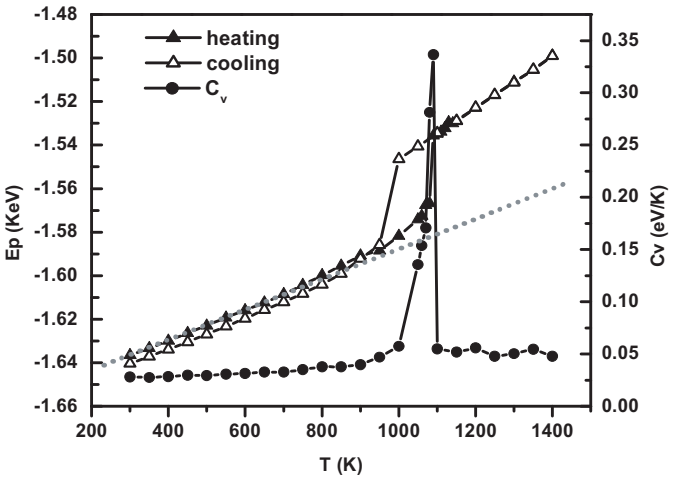

(a)

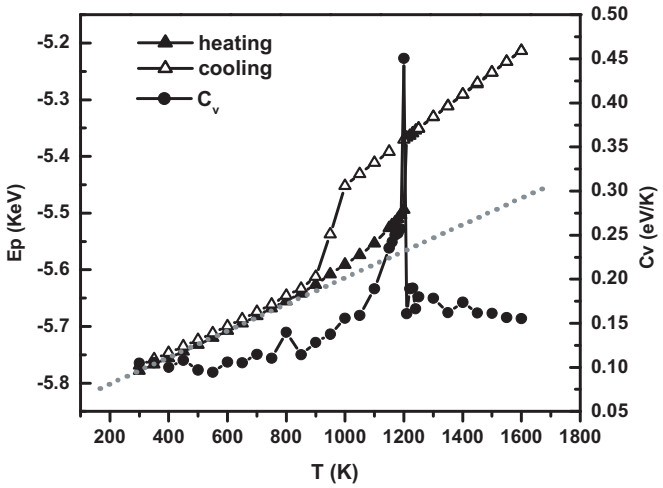

(b)

Figure 4-1. Potential energy and heat capacity of the Pd (a) nanocluster and (b) nanowire. Heating and cooling data points are on top of each other above the transition temperature, only cooling points are visible on the graphs.

Table 4-2. Thermodynamic properties for Pd bulk, cluster and nanowire.

	T_m (K)	ΔH_f(kJ/mol)	γ_{sv}†(J/m^2)
Bulk (simulation)	1760	16.83	–
Bulk (experiment)	1825[a]	16.70[b]	1.808[a]
Pd cluster	1090	6.71	1.328
Pd nanowire	1200	7.36	1.393

† Values measured at T=300 K.
[a] Values obtained from Vanselow and Howe [98]
[b] Values obtained from Iida and Guthrie [99]

$$\Delta H_f = H_l - H_s \tag{4-5}$$

where l and s stand for the enthalpy of the liquid and solid phases. The calculated value of the heat of fusion (ΔH_f) for bulk, cluster and nanowire are listed in Table 4-2. The total potential energy per atom is larger indicating the existence of a surface energy [96], which can be calculated by Equation 4-6.

$$\gamma_{sv} = \left(E_{p_{nano}} - E_{p_{bulk}}\right)/A \tag{4-6}$$

where E_p is the potential energy of cluster, nanowire or bulk. A is the surface area, calculated as surface area of perfect sphere or cylinder, which is approximately equal to the surface area of cluster and nanowire at 300 K. For the Pd cluster system, the difference of potential energy at 300 K is 29.873 kJ/mol. Hence, we obtain a surface energy of 1.328 J/m^2. Similarly for nanowire, we have γ_{sv}=1.393 J/m^2. Therefore, we see that the Pd nanowire has larger energy per unit surface and higher heat of fusion than the comparable Pd cluster, which in turn implies the higher melting temperature.

Shape changes of the Pd nanocluster and nanowire were monitored by calculating the radius of gyration using Equation 4-3. Considering that the infinitely long nanowire in symmetrical about the z-axis, and we are only interested in the shape variance in the xy-

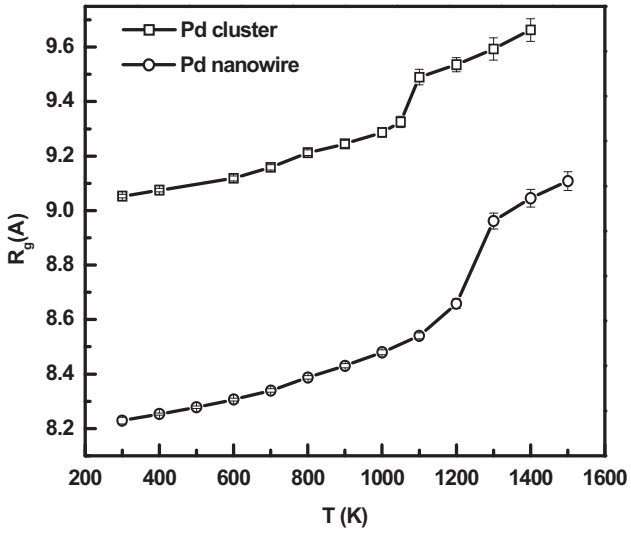

Figure 4-2. Radius of gyration vs. temperature for Pd cluster and Pd nanowire with repeating unit of length of 5.6 nm.

plane, we use 2 dimensional R_g for the Pd nanowire, which is to say only the distance from each atom to the z-axis is utilized.

Figure 4-2 shows the temperature dependence of the radius of gyration R_g of the Pd nanocluster and nanowire. In both cases, R_g has an upward jump at the melting transition, indicating that cluster and nanowire behave similarly in expanding to a wider shape.

The structural features of the nanowire upon heating were further explored by visualization through snap shots and trajectory plots to understand the differences in the surface pre-melting phenomenon between the nanowire and cluster. Figure 4-3(a) shows sample projected coordinates, on to the plane parallel to the nanowire axis, of each atom at two temperatures of 700 K and 800 K, as blue and red dots, as well as a dashed line connecting each of the atomic positions at the two temperatures. What is apparent is an oscillatory motion in the plane perpendicular to the nanowire axis, with atoms mostly retaining their positions through the simulation duration. Very few surface atoms exhibit large movement along the wire axis, crossing different planes. This surface atomic movement was found to

be rarer at temperatures lower than the 700-800 K shown in this figure. While a bit more difficult to see from Figure 4-3(b), similar behavior is exhibited at the slightly higher temperatures of 900 and 1000 K. The top view in Figure 4-3(b) shows more movement at the surface than towards the center of the wire. Analysis of these and similar plots along with trajectory visualizations have provided a picture of the surface pre-melting of one where the nanowire exhibits increasingly freer motion of the surface atoms in the plane perpendicular to the nanowire axis at temperatures much below the near first-order transition temperature, with the degree of freedom parallel to the nanowire axis available at higher temperatures, closer to the transition temperature. The surface pre-melting is further characterized by a shrinking solid-like core of the nanowire, as the temperature increases to the transition point. This physical picture is consistent with the deviation of the potential energy curve from linearity as shown in Figure 4-1(b), however, these details of the structural and dynamical changes are not apparent from that plot. Indeed, the potential energy curve for the near-spherical nanocluster shown in Figure 4-1(a) exhibits similar behavior, however, details of the surface pre-melting are quite different, a difference arising from the difference in the geometry. It should be noted here that both nanoclusters and nanowires of various metals have been synthesized by a variety of templating and other solution techniques, and it is possible to experimentally observe these differences in melting behavior upon heating of these nanomaterials. No such experiments have been reported in the literature to our knowledge.

Components of the velocity auto-correlation function in cylindrical coordinates were calculated as functions of distance from the nanowire axis to characterize atomic motion in the surface pre-melting regime. v_θ and v_z characterize movement in the xy-plane and in the z-direction. Figure 4-4 shows the correlation of v_θ and v_z with time at 800 K. The five curves in both plots represent correlated atoms at different distances from the center with 1 being the closest and 5 the farthest. The wire was partitioned into these 5 shells with

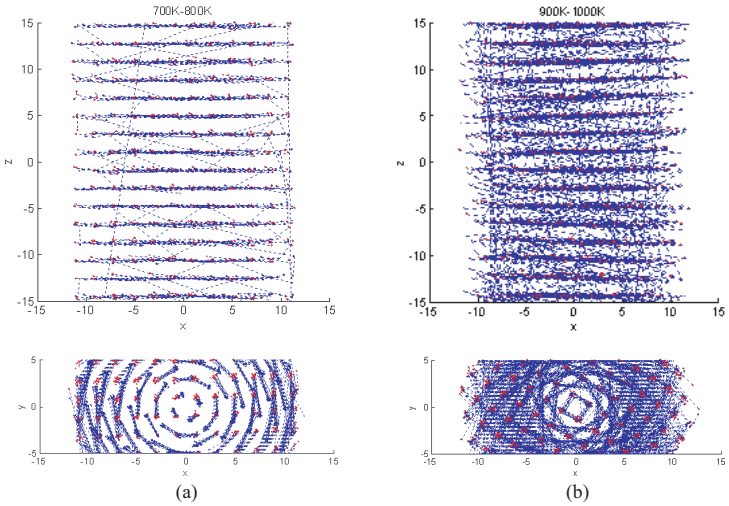

Figure 4-3. Snapshots of equilibrated atomic positions, shown as projected coordinates in planes parallel (upper) and perpendicular (lower) to (a) the nanowire axis. Blue dots are for 700 K and red dots are for 800 K, with the blue dashed lines connecting the same atoms at the two temperatures. Similar plot in (b) for 900 K and 1000 K, respectively.

dR=2.77 Å based on the initial equilibrium atomic positions (time origins of the time-correlation function calculations), with dR chosen to be close to the inter-atomic distance in bulk solid Pd of about 2.75 Å. Atoms stayed within their shells for the duration of the correlation time, and beyond, justifying these calculations to further understand the surface melting phenomenon.

Both components of the correlation functions for the inner shells exhibit rebounding oscillations that decay with time, indicative of localization at lattice sites. Comparing the two plots, v_θ has shorter correlation time and much larger depth of the minima than v_z, which implies larger amplitude tangential vibrations than axial. Behavior of atoms in the outer shells (especially, the outermost shell) is significantly different, at this temperature of 800 K, with surface pre-melting apparent. Nearly liquid-like motion is inferred from the single damped oscillation with one minimum before de-correlation with time occurs. While results at the one temperature of 800 K are shown in Figure 4-4 to illustrate the surface pre-melting phenomenon, v_θ and v_z calculated at other temperature corroborate the arguments

developed here. At temperatures higher than 900 K, axial movement is larger while the tangential oscillations are dampened. The wire diameter increases with temperature as a result of these movements.

Surface melting is observed frequently in simulations of nanoparticles. Surface atoms melt at temperatures below the transition temperature, and then the quasi-liquid skin continuously grows thicker as the temperature increases. The inner regions stay ordered until the transition temperature. The temperature at which the film thickness diverges to the entire system size is thought of as the cluster melting point. However, for ultra-thin gold nanowires, Wang *et al.* found the interior melting temperature to be lower than that of the surface, indicating that the melting actually starts from inside, exhibiting no surface melting behavior [74].

Snapshots of atomic positions projected on to a plane (perpendicular to the axis in the nanowire case) are shown in Figure 4-5. These provide evidence for surface melting in both the Pd cluster and nanowire cases.

Further evidence of surface melting in both cluster and wire is obtained from self-diffusion coefficients calculated as functions of radial distance using mean-square displacements. As in the calculation of the velocity auto-correlation functions, the atoms were assigned to bins based on their initial positions at the end of the equilibration period. The mean-square displacements for each shell were then generated by averaging over a 25 ps trajectory with sampling done every 0.1 ps. Averages taken over a 25 ps trajectory with different origins gave the same result which is indicative of a system that is truly in equilibrium. The self-diffusion coefficients were calculated for each radial shell at various temperatures using Equation 4-7.

$$D = \frac{1}{6N} \lim_{t \to \infty} \frac{d}{dt} \sum_{i} \left[r_i(t) - r_i(0) \right]^2 \tag{4-7}$$

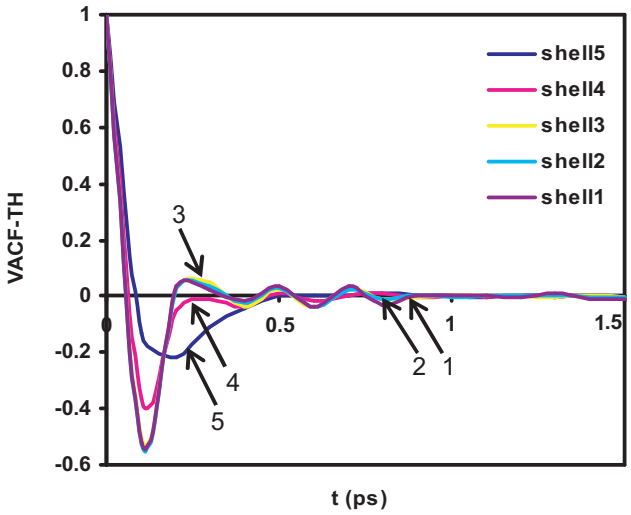

(a)

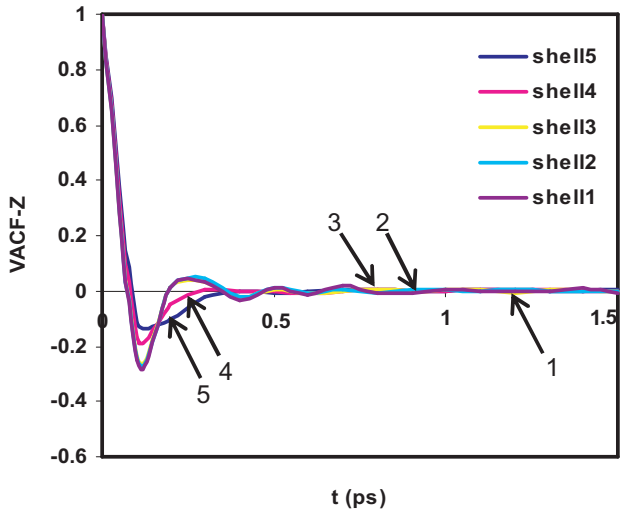

(b)

Figure 4-4. Velocity autocorrelation functions (a) v_θ and (b) v_z for atoms in different shells of the Pd nanowire at 800 K. Shell 1 is the closest to the wire axis and shell 5 is the farthest.

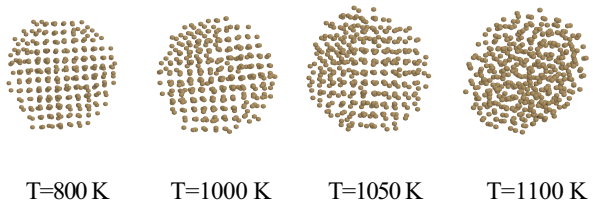

(a)

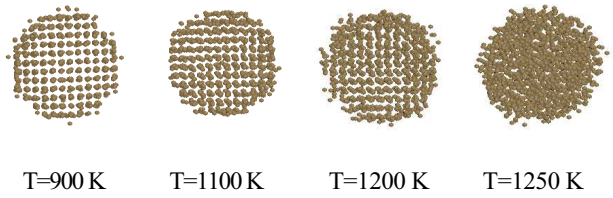

(b)

Figure 4-5. Snapshots of the projected atomic positions of the (a) 456 Pd atom clusters at different T and (b) 1,568 atom Pd nanowire projected on to a plane perpendicular to the axis.

These are shown in Figure 4-6. In all the cases, we find the diffusivities of outer shells to be higher than those of the inner ones. If $D_1 \sim D_5$ denote self-diffusion coefficients of these shells from inner to outer, we found that at lower temperatures, both clusters and nanowires have similar self-diffusion coefficients of the order of 10^{-3} Å^2/ps. Atoms in the outer shells have larger diffusion coefficient than the atoms closer to the core atoms. As the temperature increases further, the diffusion coefficient of the outermost shell, D_5, first starts to increase rapidly. This is followed by an increase of D_4, while D_1, D_2, D_3 retain their values from the lower temperatures. This state is maintained until the melting transition temperatures are approached. The larger diffusion coefficients in outer shells and relatively static state of inner shells at temperatures below the transition temperatures support the existence of surface melting in both Pd cluster and nanowire. Atoms on the surface have weaker restraining forces than the core atoms. Although surface melting in some sense is

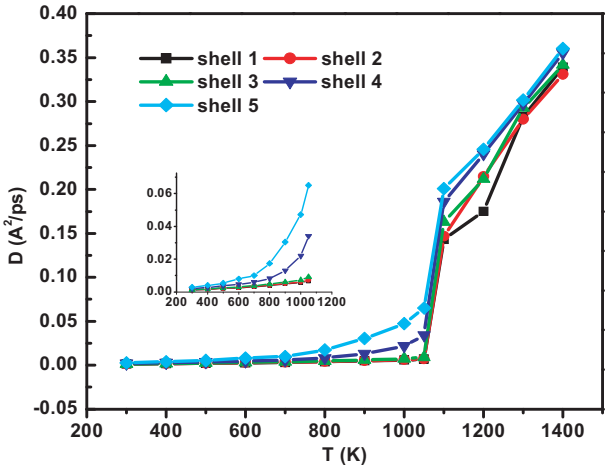

(a)

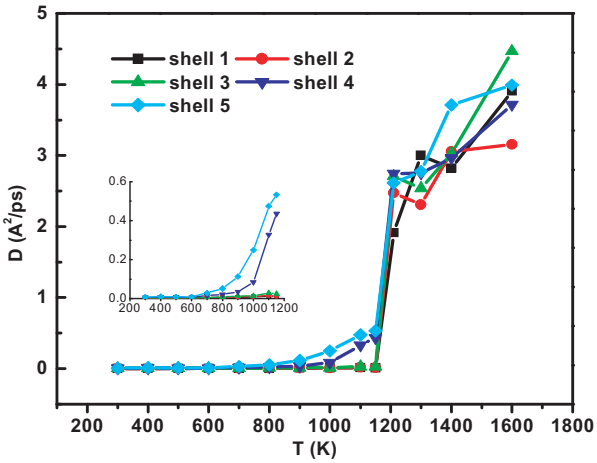

(b)

Figure 4-6. Self-diffusion coefficient for atoms in different radial shells at various temperatures for (a) Pd cluster and (b) Pd nanowire.

not necessarily a diffusive process, it can be considered a complex phenomenon involving cooperative motion [97]. According to the Lindemann criterion, the phase transition occurs when atomic motion exceeds 10-15% of inter-atomic distance. From the variation of the diffusion coefficients in various bins, we can infer a continuous layer-by-layer melting as the atomic displacements meet the Lindemann criterion in a layer-by-layer manner, until, the criterion is met for the remaining solid core all at once, at the near first order transition temperature. From the diffusion plots, together with the variations of potential energies and heat capacity curves in Figure 4-1, we estimate the surface melting regions of the Pd cluster and nanowire to start at about 700-800K, and 800-900K, respectively. At melting points, diffusion coefficients of all the shells exhibit large jumps of similar magnitude, indicating the phase transitions from solid to liquid.

Structural properties and changes in them during heating are of interest in understanding mechanical and catalytic properties of materials. Experimental observations include changes in the lattice parameter, surface coordination and structural fluctuations. Some theoretical calculations include detailed studies of the topology and structural stability. Many small clusters, with special numbers of atoms, so-called magic numbers, have proven to be more stable than others [100]. The change in crystallographic structure can be attributed to surface energy. Icosahedral Pd clusters with 13, 55, 147 atoms are examples. The geometry of these extremely small clusters with unique minimum energy has been extensively studied [69, 79]. In this work, we pay attention to the time evolution of the structures during heating by investigating two parameters: atomic number distribution along the z-direction (a Cartesian direction, along the wire axis for the nanowire) and bond-orientational order parameters.

The atomic number distribution $N(z)$ for each element is difined in Equation 4-8. $N(z)$ is a good way to look at the structural features during heating of the spherical cluster and one dimensional nanowire of similar diameter. Plots in Figure 4-7 show the distribution

of Pd atoms along z-axis at different temperatures. In the solid phase, atoms have higher distribution only at certain distances from the center, forming many sharp peaks. Those peaks become wider and shorter upon heating, and finally disappear due to the uniformly distributed atoms in liquid phase. This expected behavior in $N(z)$ is seen in the Pd cluster case, as shown in Figure 4-7. In contrast, Figure 4-8 for the nanowire exhibits complicated structural features. Longer wave-length variations in the $N(z)$ distribution are introduced due to increased amplitudes of oscillations of the atoms in ordered zones. The ordered zones appear to move along the wire as we approach the transition, with the possibility of such movement with time, at a single temperature. While the lowest temperature shown in Figure 4-8 is 600K, we have seen this behavior at the lowest temperature simulated, of 100K. This extremely interesting behavior could be an artifact of the periodic boundary conditions. To explore this further, we have repeated the simulations with a wire that is twice in length. Results indicated that the longer wave-length ordering of zones is possible in the surface-melting regime, and is enhanced as the transition temperature is approached. However, the periodic structures observed in the low temperature solid structures such as shown in Figure 4-8(a) have disappeared. None of the melting properties we report in this manuscript were affected by the doubling of the wire-length. We conclude that there exists the possibility of ordered zones in Pd nanowires at close-to-transition temperatures, and that this phenomenon should be explored with simulations of much longer wires, to eliminate all effects of periodic boundary conditions. To explore the possibility of lower density in the valley (and consequent higher density in the peaks) we have utilized the two dimensional radius of gyration, as defined previously for the nanowire. Calculations of these radii in the peaks and valleys yielded nearly the same numerical values in the solid-phase, indicating that these features are caused by larger amplitude oscillations of the atoms.

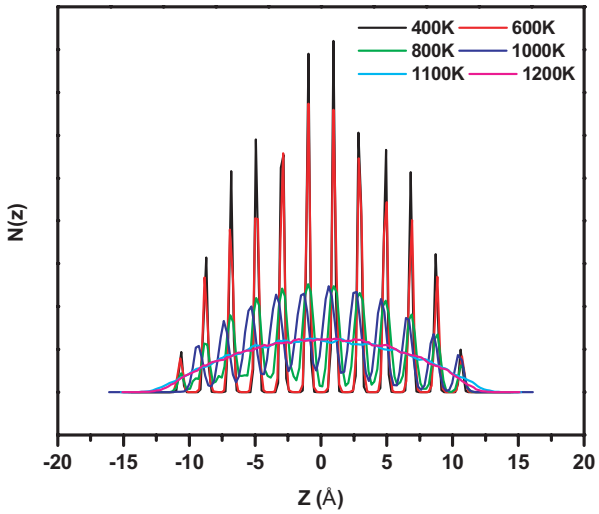

Figure 4-7. Comparison of Pd atomic distributions of Pd cluster along a Cartesian coordinate (z) at different temperatures.

$$N(z) = \left\langle \sum_i \delta(z_i - z) \right\rangle \tag{4-8}$$

The bond-orientational order parameters (BOP) method was applied to quantify structural evolution of the clusters and nanowries crystallographically, as well as to distinguish between liquid-like and solid-like states [101]. Bonds are defined as the vectors joining a pair of neighboring atoms with an inter-atomic distance less than a specified cutoff radius. The cutoff distance is usually chosen as the position of the first minimum in the pair correlation function, which is about 3.36 Å is this case. Associated with every bond are a set of numbers called local bond-orientational order parameters shown in Equation 4-9.

$$Q_{lm}(r) = Y_{lm}\left[\theta(r), \phi(r)\right] \tag{4-9}$$

where $Y_{lm}(\theta, \phi)$ are spherical harmonics and $\theta(r)$ and $\phi(r)$ are the polar angle and azimuthal angles of vector r with respect to an arbitrary reference frame. Only even-l spherical harmonics are considered, which are invariant under inversion. A global bond-orientational

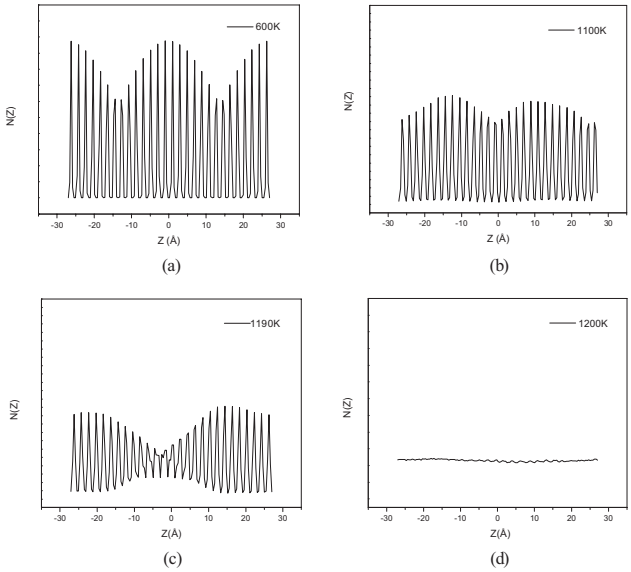

Figure 4-8. Comparison of Pd atomic distribution along a Cartesian coordinate (z) in the Pd nanowire at (a) 600 K, (b) 1100 K, (c) 1190 K, and (d)1200 K.

order parameter $\bar{Q}_{lm}(r)$ can be defined by averaging $\bar{Q}_{lm}(r)$ over all bonds in the system using Equation 4-10.

$$\bar{Q}_{lm} = \frac{1}{N_b}\sum Q_{lm}(r) \tag{4-10}$$

where N_b is the number of bonds. To let $\bar{Q}_{lm}(r)$ not depend on the choice of reference frame, a second-order invariant is constructed using Equation 4-11, and a third-order invariant is constructed using Equation 4-12.

$$Q_l = \left(\frac{4\pi}{2l+1}\sum\left|\bar{Q}_{lm}\right|^2\right)^{1/2} \tag{4-11}$$

$$W_l = \sum_{m_1,m_2,m_3}\begin{pmatrix} l & l & l \\ m_1 & m_2 & m_3 \end{pmatrix}\bar{Q}_{lm_1}\bar{Q}_{lm_2}\bar{Q}_{lm_3} \tag{4-12}$$

Table 4-3. Bond-orientational order parameters for a number of simple cluster geometries.

Geometry	Q_4	Q_6	$\hat{W}_4$	$\hat{W}_6$
Icosahedra	0.00000	0.66332	0.00000	0.16975
Fcc	0.19094	0.57452	0.15932	0.01316
Hcp	0.09722	0.48476	0.13410	0.01244
Bcc	0.03637	0.51069	0.15932	0.01316
Liquid	0.00000	0.00000	0.00000	0.00000

The term in the bracket is a Wigner-3j symbol [102]. Furthermore, a reduced order parameter $\hat{W}_l$ is defined in Equation 4-13 so that it is not sensitive to the precise definition of the nearest neighbor of a particle.

$$\hat{W}_l = W_l / \left(\sum \left| \bar{Q}_{lm} \right|^2 \right)^{3/2} \tag{4-13}$$

The values of these bond-orientational order parameters for some common crystal structures are listed in Table 4-3 [101]. Because of symmetry, the first nonzero values occur for l = 4 in the cluster with cubic symmetry and for l = 6 in clusters with icosahedral symmetry. We used the four bond-orientational order parameters Q_4, Q_6, $\hat{W}_4$, $\hat{W}_6$ together to identify structures. Note that Q is of the same order of magnitude for all crystal structures of interest, which makes it less useful for distinguishing different crystal structures compared to $\hat{W}$. But Q_6 is useful to identify phase transitions, since it has a larger value than other parameters and decrease quickly to zero when the system becomes liquid. Considering the surface effect in nanomaterials and to get more accurate answers to monitor global structural changes, we calculated bond-orientational order parameters for internal atoms, surface atoms and all atoms in the systems.

The time averaged bond-orientational order parameters of the internal atoms, surface atoms, and the entire Pd nanowire system are plotted in Figure 4-9(a). We see that only the second-order invariants (Q values) differ when the surface atoms are excluded, while

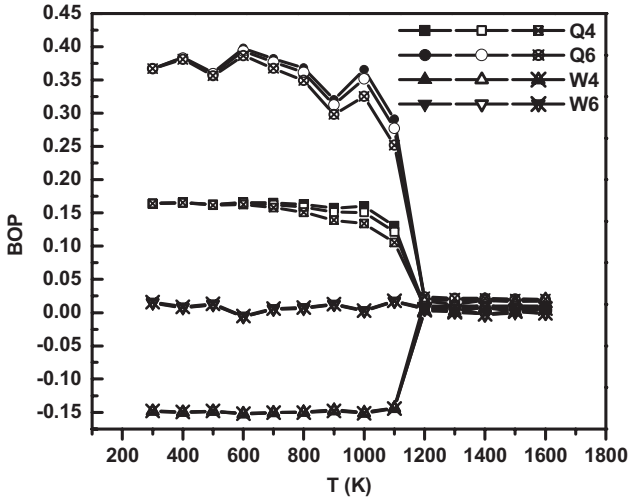

(a)

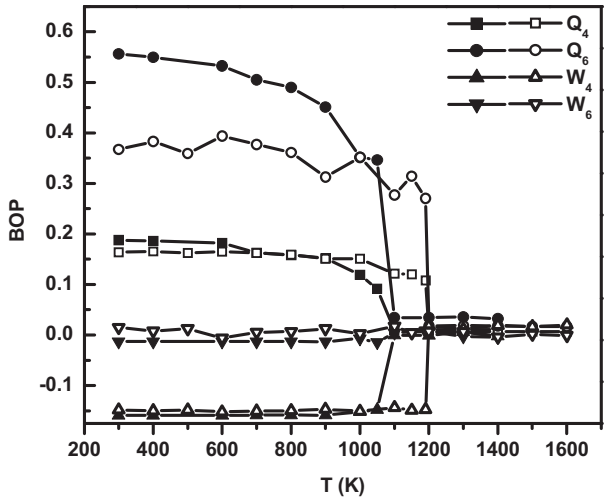

(b)

Figure 4-9. Temperature dependence of average bond-orientational order parameters for (a) the atoms in Pd nanowire and (b) the Pd cluster with 456 atoms and Pd nanowire with 1,568 atoms during heating. (a) Filled, unfilled and unfilled with a cross symbols correspond to the average bond-orientational order parameters for internal atoms, all atoms and surface atoms, respectively. (b) Filled and unfilled symbols represent cluster and nanowire, respectively.

the third-order invariants ($\hat{W}$ values) are not affected. This is because Q is more sensitive to the number of the nearest neighbors. Figure 4-9(b) shows the bond-orientational order parameter comparison between the Pd cluster and the Pd nanowire. All the parameters drop abruptly to zero at the transition temperature. These changes are more obvious in Q_6. Even though the Pd cluster retains the fcc structure at lower temperatures, the time averaged global bond-orientational order parameters show that the Pd nanowire moves away from the starting fcc structure, which is consistent with what we have seen in the $N(z)$ plots. The correlation plot for $\hat{W}_6$ as a function of Q_6 is shown in Figure 4-10, where the red dots are the values for perfect crystals. We use Q_6 because it changes significantly with temperature. We see from the time averaged bond-orientational order parameters that at low temperature, the Pd nanowire no longer has fcc structure, instead it forms some structure beyond regular crystal geometries. From Figure 4-10, we observe that the nanowire undergoes a rapid structural change during the annealing process, after that it maintains a non-regular structure at low temperatures before the phase transition. Unlike the nanowire, the cluster goes through possible structural changes in the same temperature range, reflected by the decreasing rate of change of Q_6. Calculated values of Q_6 are sensitive to the number and positions of the surface atoms. More rapid changes in the number and positions of these surface atoms in the cluster compared to the cylindrical wire with periodic boundary conditions could explain this behavior of Q_6. $\hat{W}_6$ has more fluctuations in the nanowire than the cluster, indicating frequent symmetry changes [101].

In our simulations, we have chosen the bulk, fcc structure for the starting configurations of the low temperature solid nanocluster and nanowire. It is difficult to establish the true low temperature solid structures of these nanomaterials from molecular dynamics simulations. One cannot be certain that the bulk fcc structure is a reasonable starting structure, although other studies have utilized bulk structures for starting configurations of nanomaterials [68, 96, 103]. Some insights can be gained by starting the simulations

from other hypothetical structures, such as the hcp, and a glassy structure that results from the first heating/cooling cycle of the fcc-started simulation. To establish the reasonableness of our fcc-started simulations, we have repeated the heating/cooling simulations with an hcp initial structure and the glassy structure obtained at 300 K upon completion of the first fcc-started MD run after a full heating/cooling cycle. Some experimental [104] and simulation [67] evidence for the possibility of hcp structures in nanoclusters exists in the literature, with less known about nanowires. With minor variations accounted for by the differences in numbers of atoms (mandated by the differences in starting configurations for different close packed structures of same diameter), we have found that the melting points are essentially the same as those obtained from the fcc-started simulation. While the hcp-started cluster appeared to be stable at low temperatures, it undergoes a less sharp transition (while yielding nearly the same melting point), perhaps, due to structural rearrangement in the solids near melting temperature and/or enhanced surface melting as compared to the fcc-started cluster. The hcp-started nanowire, on the other hand, rapidly rearranged to a less-ordered structure at low temperatures as in the fcc case, and showed a sharper melting transition, with an identical melting point as the fcc-started wire. The annealed solid structures during cooling, of both cluster and wire, did not track potential energies of the heating run, indicating that the fcc starting configuration is perhaps closer to the true structure of the both the cluster and the wire. Nearly identical melting points and potential energy curves were found from the second heating/cooling cycle of the fcc-started cluster and wire, indicating that the cycle, including hysteresis, is repeatable. This gives further support to the choice of the fcc structure in our low temperature solid starting configurations. Coupled with the results for the bond orientational order parameters presented in Figure 4-10, we conclude that the chosen fcc starting configurations are reasonable in this study. Generally, prior to melting, both systems have trends towards disorder as number of unclassified bond orientations increases. The classifications of local atoms during heating

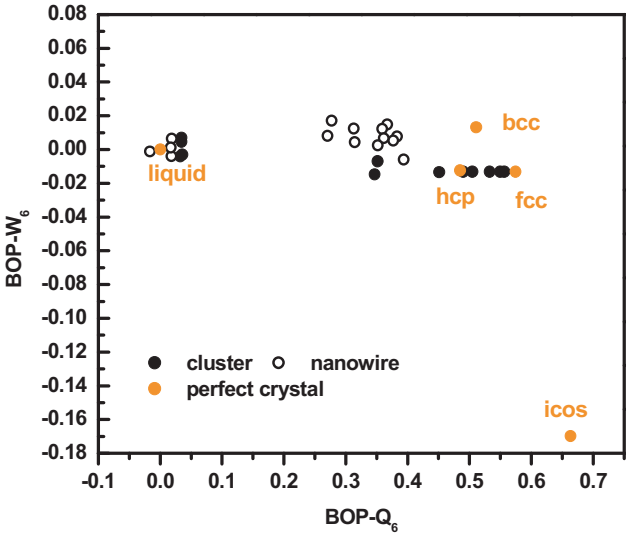

Figure 4-10. Correlation plot for bond-orientational order parameters $\hat{W}_6$ as a function of Q_6. Symbols are at 100 K intervals starting at 300 K.

can be improved by studying CNA (common neighbor analysis) signatures, as shown in the work from Hendy *et al.* [105].

4.5 Melting Model Comparison

Melting behavior, especially melting temperature, of clusters and nanowires will depend on their size. The study of size effects on melting of metallic nanoparticles has been explored both experimentally and theoretically [52, 106–108]. And a large number of data have been established. Models for the size-dependent melting point depression for different materials have been established based on various assumptions, such as many outstanding classic thermodynamics models [54, 109–113] and other models, like surface-phonon instability model [114], bond order-length-strength (OLS) model [36], and liquid-drop like model [115]. The general result of these theories is that melting temperature of small particles decreases linearly or quasi-linearly with the decreasing of their diameters. In this section, we compare our simulated results with two of the models.

The thermodynamics model was first proposed by Pawlow in 1909, it is based on equating the Gibbs free energies of solid and liquid spherical clusters, assuming constant pressure conditions, with the resulting equation [109, 110].

$$\frac{T^b - T_c(R)}{T^b} = \frac{2}{\rho_s L^b R}\left[\gamma_{sv} - \left(\frac{\rho_s}{\rho_l}\right)^{2/3}\gamma_{lv}\right] \tag{4-14}$$

where T^b and L^b are the bulk melting temperature and bulk latent heat of melting, ρ is the mass density, γ_{sv} and γ_{lv} are the solid-vapor and liquid-vapor bulk material interfacial energies, respectively. The simulated melting point depression (T_b-T_c (2.6 nm)) of 670 K is higher than the 278 K predicted by the above model. It has been pointed out in the literatures that the 1/R behavior is approximately correct for clusters of sufficiently large size [55, 94].

For a nanowire, a similar procedure can be applied by equating the Gibbs free energies per unit length of solid and liquid at constant temperature and pressure. Gülseren developed a model for the melting temperature $T_{nw}(R)$ of nanowires using Equation 4-15 [71].

$$\frac{T^b - T_{nw}(R)}{T^b} = \frac{1}{\rho_s L^b R}\left[\gamma_{sv} - \left(\frac{\rho_s}{\rho_l}\right)^{1/2}\gamma_{lv}\right] \tag{4-15}$$

These two models have been shown to agree with simulation results in Gülseren's Pb clusters and wires constructed from (110) planes with more than 1,100 atoms in the systems.

From Equation 4-14 and 4-15, we see that since ρ_s/ρ_l is close to 1, the depression of melting temperature of a spherical cluster should be approximately twice that of the corresponding amount for a nanowire. Using γ_{sv} =1.808 J/m^2, γ_{lv} =1.480 J/m^2, ρ_s = 0.0681 atom/Å^3, ρ_l = 0.0594 atom/Å^3, and L^b = 16.69 kJ/mole, the calculated depressions of melting temperatures are 160 K and 278 K for the Pd nanowire and cluster, respectively, giving a ratio of 1.7. However, our simulation results yield a ratio of 1.2. This discrepancy may be due to the many assumptions in the model and the simulation, for example, the surface

energy anisotropy of the solid is not taken into account, and the possibility of inhomogeneous phases is also neglected in the model. The same discrepancies between model and simulation results exist in other previous work [68, 103]. The accuracy of these models appears to be better for larger clusters and nanowires than simulated here. It should also be noted that significant variation exists in the literature for values of the interfacial energies. Also, using the simulated interfacial energies for the clusters and wires, and not the bulk values, would improve comparison with Pawlow's model.

The other scaling law [115] for size-dependent melting is based on the liquid-drop model and empirical relations between surface energy, cohesive energy and size-dependent melting temperature. According to this model, the cohesive energy of N-atom nanoparticles can be represented by volume and surface dependent terms. For a spherical nanoparticle of diameter d, the expression for the cohesive energy per atom is shown in Equation 4-16.

$$a_{v,d} = a_v - \frac{6v_0\gamma}{d} \tag{4-16}$$

where $a_{v,d}$ and a_v are the cohesive energy per atom in the cluster and in the bulk, v_0 is the atomic volume and γ is surface energy of solid-vapor interface. Using empirical relations between cohesive energy and melting temperature for both bulk and nanoparticles, the melting temperature of nanoparticles can be calculated by Equation 4-17.

$$\frac{T_c(R)}{T^b} = 1 - \frac{6v_0}{0.0005736d}\left(\frac{\gamma}{T^b}\right) = 1 - \frac{\beta}{d} \tag{4-17}$$

where $\beta = \frac{6v_0}{0.0005736}\left(\frac{\gamma}{T^b}\right)$. The value of β can be calculated from the known values of v_0, γ, and T^b. Using for Pd in Equation 4-17, we get the melting point depression of the Pd cluster of 669 K, which compares well with our simulated value of 670 K. This favorable comparison is consistent with other work mentioned previously [68, 103]. Using the same

model for the melting of thin wires, the size-dependent melting temperature of a nanowire can be described by Equation 4-18 [115].

$$\frac{T_{nw}(R)}{T^b} = 1 - \frac{2\beta}{3d} \tag{4-18}$$

From this, the depression of melting temperature of the nanowire is 446 K, smaller than our simulated result of 560 K. This relation described in Equation 4-18 has some similarity to the model of Gülseren, described previously, except that the depression of melting temperature of a nanowire is 2/3 of the depression of the spherical nanocluster.

$$\frac{T^b - T_c(R)}{T^b - T_{nw}(R)} = 1.5 \tag{4-19}$$

The result obtained from Equation 4-19 is closer to our simulation result of 1.2 than that from Pawlow's model.

4.6 Conclusions

The simulation studies of this work indicate that the Pd nanowire has lower melting temperature than Pd bulk but higher than the same diameter Pd cluster. Both Pd nanowires and nanoclusters exhibit surface pre-melting, the structural and dynamical nature of which is somewhat different. These differences are fully characterized by several thermodynamic, structural and dynamic variables in this study. The general picture that emerges is that the surface pre-melting behavior for the cluster is similar to that of other noble and transition metal nanoclusters. The nanowire exhibits a higher pre-melting temperature range, and dynamical behavior characterized by increased movement of atoms in the plane perpendicular to the axis followed by increased movement across these planes, as the temperature approaches the transition temperature. A quasi-liquid skin grows from the surface in the radial direction for both cluster and wire, in the surface pre-melting regime, followed by

the breakdown of order in the remaining solid core at the transition temperature. Bond-orientational order parameters indicated that the cluster retains the initial fcc structure, whereas, the nanowire appears stable in a structure close to the hcp, in the solid phase, before melting. Melting points of studied cluster and wire were characterized particularly well by the liquid-drop model for size-dependent melting.

Chapter Five

Molecular Dynamics Simulations of Graphite Supported Pd Na-nocluster Melting

5.1 Abstract

The thermal behavior of graphite supported and unsupported palladium nanoclusters were studied using molecular dynamics simulations. Due to interactions between Pd and C in the supported environment, differences in thermodynamic, geometric and structural properties were observed. As such, graphite supported Pd nanocluster had higher melting temperature than the unsupported cluster. At high temperatures, the motion and geometry of surface atoms are quantitatively different. Radial and angular correlation functions indicate very similar structural evolution of the two systems, but a stronger positional correlation with the nearest neighbors of supported Pd cluster.

5.2 Introduction

The study of melting process and thermodynamic properties of metallic clusters of nanometer length-scales has attracted much theoretical [50, 51, 116] and experimental [52, 53, 117] interest mainly because of their dramatically different behaviors from the bulk materials [54]. Transitional and noble metal [56–58] or alloy [59, 60] clusters are getting more attention, due their extensive applications. Theoretical investigations of their melting phenomena using various simulation methods are focused on the following:

1. The melting temperature and details of the melting process [67].

2. The structural evolutions and mechanical properties during heating [55, 69].

3. The effect of initial structure and size on the melting temperature [50, 106].

Pd has been widely used in heterogeneous catalysis as well as in microelectronic and optoelectronic devices [75, 76]. Normally Pd is supported on a graphite substrate when it is used as catalyst [118]. Recently, the significance of the support was investigated to improve the catalytic properties of Pd [119]. The structural and dynamic properties of metallic clusters on graphite surface have also attracted much attention lately [120, 121]. For example, Bardotti *et. al* reported rapid movement of large antimony clusters on graphite surfaces, and pointed out that study of these rapid motion mechanisms leads to an understanding of the interaction between nanoparticle and substrate [122].

Several experiments indicate that quantum behavior of metal nanoclusters is observable, and strongly expressed between 1 and 2 nanometers. Hence, particles in that size region should be of most interest [77, 78]. Simulation studies of Pd nanoparticle provide an opportunity for further understanding its unique role in various applications, and explaining experimental observations. Although the size of the metallic clusters being simulated ranged from tens to several thousand atoms, most efforts have been focused on size below 150 atoms [79]. In this paper, the melting behaviors of unsupported and graphite-supported Pd clusters of 2.3 nm diameter (456 atoms) are studied. The support-effects of graphite on both melting and structural properties are investigated in this study.

5.3 Potential Model and Computational Method

MD simulations were performed using the DL_POLY package [47]. The system was simulated under NVT ensemble using the Verlet leapfrog algorithm [89]. A time step of 1 fs was used and no boundary condition was applied. The clusters were constructed from face-centered cubic Pd bulk, using spherical cutoff radii to get desired size. A cluster size

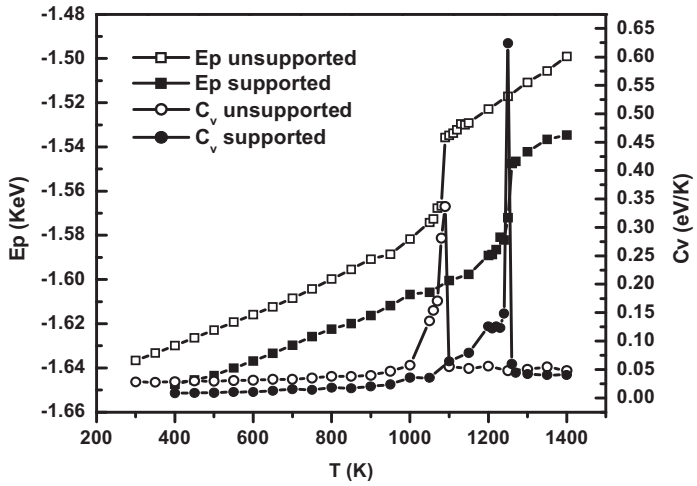

Figure 5-1. Potential energy and heat capacity unsupported and graphite-supported Pd clusters vs. temperature (d=2.3 nm). C_v is calculated by Equation 4-4.

of 2.3 nm with 456 atoms is used. A two layer AB stacked graphite substrate with dimensions of 73.8×73.8×6.7 Å was used to support Pd clusters. A distance of 2.0 Å is set as the initial distance between the cluster and graphite. Sutton-Chen potential (SC) [48] shown in Equation 4-1 is used to describe the Pd interactions. The Pd-graphite interaction potential was developed using DFT calculation with LDA approximations previously [123]. Due to the much smaller Pd-carbon interaction forces compared to Pd-Pd forces, the Lennard-Jones (LJ) potential was also deemed adequate to model the Pd-C interactions. The LJ well-depth ε and size σ for C and Pd are calculated to be 2.926 Å and 0.0335 eV using the Lorentz_Berthelot mixing rules [41, 124, 125]. A static graphite substrate with fixed C atomic positions is used to save a computational effort. The initial clusters were first relaxed by simple quenching, followed by annealing cycle. Each system was then heated with a temperature step of 50 K. The step size was decreased to 10 K when close to melting temperature.

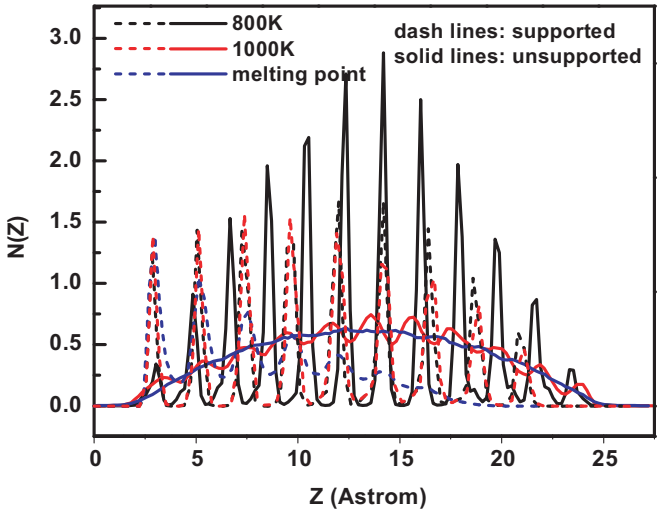

Figure 5-2. Atomic distribution function along z coordinate perpendicular to the graphite substrate.

5.4 Results and Discussion

We first calculate the total potential energy E_p and heat capacity C_v at various temperature to identify the melting temperature for both graphite-supported and -unsupported Pd cluster. As shown in Figure 5-1, the potential energies increase nearly linearly with temperature, while heat capacities remain mostly constant at low temperatures. Near the melting temperature, simple jumps in both E_p and C_v values can be easily observed as an indicative of the phase transition. According to the Figure 5-1, we estimate that the melting temperature of the unsupported and supported Pd cluster occur at 1090 K and 1260 K, respectively. Note that both clusters have much lower melting temperatures than the Pd bulk, which is 1760 K from our previous simulations [116]. The higher melting temperature of supported Pd cluster is due to the restraining movement of Pd atoms on the substrate, which also explains the lowering of potential energy compared to the unsupported cluster.

Atomic distribution function $N(z)$ is calculated to investigate the organization of Pd atoms in the clusters at various temperatures. Figure 5-2 describes the distribution of Pd

atoms along the axis perpendicular to the graphite surface, where z=0 is the position of the graphite surface. We observe that in the solid phase, atoms have higher density in the center area, indicated by sharp peaks. This is because at low temperatures, atoms oscillate around the lattice sites and retain the crystal-like structure. The peaks become wider and lower upon heating, and eventually disappear, leading to uniformly distributed atoms in the liquid phase. A different set of $N(z)$ distributions for the graphite-supported cluster were observed at the same temperatures. We see that although the temperature is well below melting temperature the supported Pd cluster has greatly changed its atomic distribution with enhanced peaks close to the substrate (black dashed lines), indicating substrate effect is evident even in the weak field of graphite.

The supported Pd cluster continues to maintain its crystal-like structure at the higher temperature of 1000 K (red dashed lines), as atomic layers separated by unit cell length can still be clearly seen, and a gradually decreasing density distribution with increasing z. At the melting temperature (blue dashed lines), the entire cluster collapses into a wider ellipsoidal shape, spreading over the substrate with the density reaching essentially zero at 20 Å above the substrate. Sharp peaks are evident in the lowest few layers, where the physical state is clearly liquid-like at this melting temperature. Similar density distributions are observed at higher temperatures, with the cluster seen to have essentially melted into a liquid but layered against the surface, as is typically observed in small molecular liquid physisorption. On the contrary, unsupported cluster has evenly atomic distribution implied by a smooth $N(z)$ curve.

We have noticed that the shape change of same sized unsupported Pd cluster and graphite supported cluster are much different due to the existence of the substrate. In order to characterize the support effect of graphite substrate on the motion of Pd atoms and the surface melting phenomena, we compute components of the velocity auto-correlation function in cylindrical coordinates for the lowest four Pd atomic layers. Both components of the

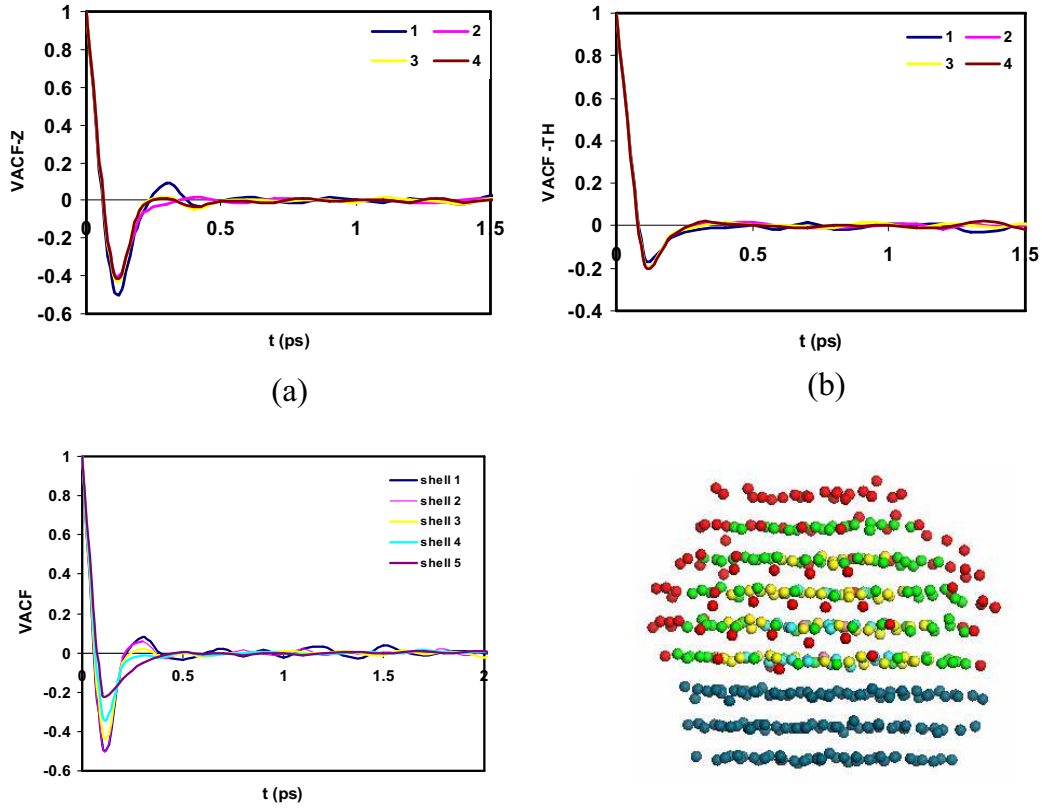

Figure 5-3. Velocity autocorrelation functions of the supported Pd cluster at 1000K. (a) and (b) are v_θ and v_z component correlations for the bottom four layers. Layer 1 is the closest to graphite, layer 4 is the farthest. (c) v correlations of different shells. Shell partition is shown in (d). from shell 5 to 1 are color red, green, yellow, light blue and purple. The three bottom layers are excluded in the shell partition.

correlation functions exhibit rebounding oscillations that decay with time in Figure 5-3(a) and (b). Comparing the two plots, v_z has longer correlation time and much larger depth of the minima than v_θ, which implies larger amplitude tangential vibrations than z axial. The correlation of v_z of lowest Pd layer is significantly different from the rest of three layers due to the strong interactions between Pd and carbon. The interatomic forces induced by carbon atoms restrict the large movement of Pd atoms along the z direction, forcing them to stay close to the graphite. This force is reduced with the increase in z distances, and has almost no effect on the Pd atoms above the third layer, where we notice that the third and fourth layer have almost the same correlations on v_z.

We again partitioned Pd atoms, excluding the bottom layers, into 5 shells, as illustrated in Figure 5-3, with r_{cut}=2.77 Å based on the initial equilibrium atomic positions. The calculation of velocity correlation for each shell shows the inner shells (shell 1, 2, 3) exhibit rebounding oscillations at lattice sites that decay with time, while outer shells (shell 4 and 5), have nearly liquid-like motion as inferred from the single damped oscillation with one minimum before decorrelating with time.

From velocity auto-correlation calculations, we observed that many Pd surface atoms (red dots) have liquid-like behavior at 1000 K, because of the smaller interatomic forces from neighbor atoms. This is further verified in the trajectory plot when temperature changes from 1000 K to 1100 K. The blue dash lines in Figure 5-4 indicate that atoms on close to the surface generally move downward, while inner atoms just exhibit xy planar oscillation without moving down toward graphite substrate. A clear change of the height of cluster center with respect to graphite substrate at higher temperatures indicates the supported cluster collapsed from a nearly ball shape to a half sphere with flat bottom on the substrate. This is quite different from unsupported case, where the nearly spherical cluster has an isotropic expansion to the oval shape [116].

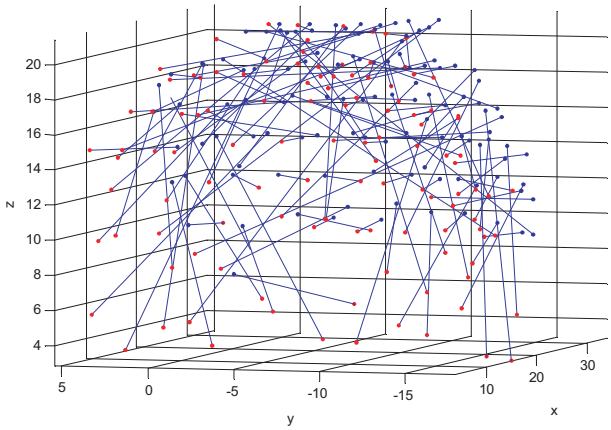

(a)

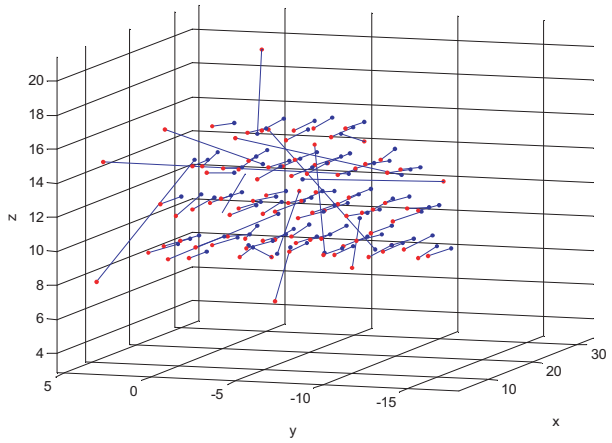

(b)

Figure 5-4. Atom coordinates of (a) surface atoms (atoms in shell 1 and 2 as illustrated in Figure 5-3(d)) and (b) inner atoms (atoms in shell 3, 4 and 5) of graphite-supported Pd cluster at 1000 K (blue dots) and 1100 K (red dots). Blue dots are connected to the corresponding red dots by blue dash lines to indicate the movement of each Pd atom.

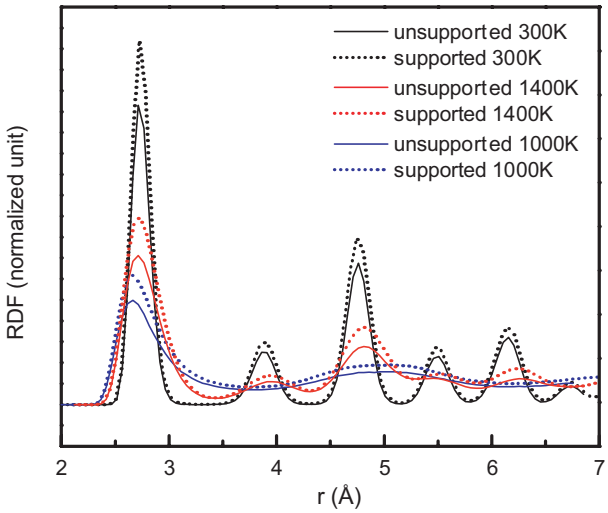

(a)

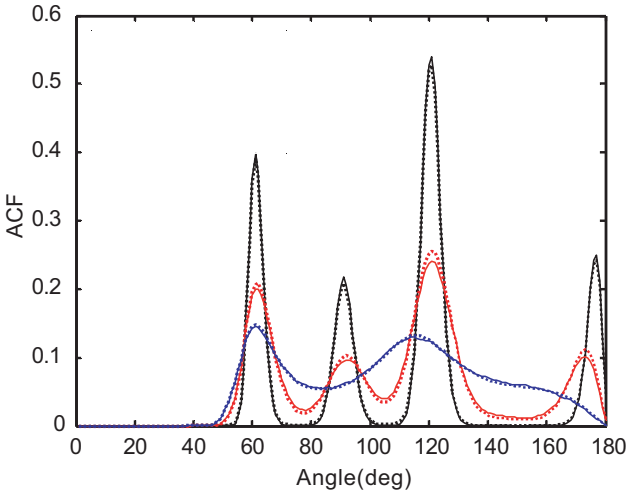

(b)

Figure 5-5. (a) Radial distribution function and (b) angular correlation function for Pd clusters.

Radial distribution functions (RDF) in Figure 5-5(a) implies very similar structural evolutions of Pd clusters with and without support. At room temperature, they both have sharp periodic multipeaks, which is a characteristic feature of fcc structures, and after melting both of them also show the amorphous feature of a disordered structure. RDF of supported Pd cluster have relatively higher and wider peak than the corresponding isolated cluster, indicating that the positional correlation of atoms is stronger within the near neighbor region. Angular correlation functions (ACF) [126] (Fig. 5-4(b)) are calculated to further illustrate the structural characters. It is obvious that Pd clusters went through almost the same structural evolution process, showing the support has little effect on the cluster internal structure change during the heating. As implied by the ACF, at lower temperatures, there are four peaks at 60°, 90°, 120°, 180° respectively, typical bond angles of regular fcc structure. At higher temperatures, the peaks at 90°, 180° gradually disappear, while other two major peaks are still located at 60° and 120°, showing a hexagonal closed packed related structure [74, 116]. After the entire cluster melts, the broad distribution of ACF at 60° and 116° demonstrate noncrystalline structure.

5.5 Conclusions

The simulation studies of this work indicate that the free Pd cluster has lower melting temperature than graphite supported Pd cluster. Surface melting is found in both cases, while several analysis reveal supported Pd cluster has a very different geometric evolution during heating. The supported cluster is seen to melt to a liquid that shows liquid multi-layer physisorbed structure, with sharp density peaks in the few Pd atomic layers near graphite. This structure is retained well into the liquid phase past the melting point. A downward movement of surface atoms of supported cluster is observed in the surface melting regime. Structural analysis implies both unsupported and supported Pd clusters have very similar structural evolutions, with a slightly more stable crystalline structure for supported cluster

at higher temperatures. This study is significant for the investigation of interaction between Pd and sensor substrate under different temperatures.

Chapter Six

Density Functional Theory and the Pseudopotential Method

In principle, the complete knowledge about a system can be obtained from the quantum mechanical wave function. This is obtained by solving the Schrödinger equation of the complete many electron system. However, in practice solving such a many-body problem proves to be computationally difficult. To make is computationally feasible, it is necessary to use density functional theory to model the electron-electron interactions and pseudopotential (PP) theory to model the electron-ion interactions. In this chapter, the essential concepts for total energy calculation using these techniques are introduced.

6.1 Density Functional Theory

6.1.1 The Hohenberg-Kohn Principle

DFT is based on the principle proven by Hohenberg and Kohn in 1964 that the total energy, including exchange and correlation, of an electron gas is a unique functional of the electron density $n(\mathbf{r})$ [127]. The minimum value of the total-energy functional is the ground-state energy of the system, and the density that yields this minimum value is the exact single-particle ground-state density. The Hohenberg-Kohn theorem can be stated as follows:

Every observable of a stationary quantum mechanical system can be calculated from ground-state density alone, i.e., every observable can be written as a functional of the ground-state density.

6.1.2 The Self-Consistent Kohn-Sham Equations

Kohn and Sham, in the following year, showed it is possible to replace the many-electron problem by an exactly equivalent set of self-consistent one-electron equations [128].

According to the Kohn-Sham approach, the total energy functional of electronic states ψ_i can be written according to Equation 6-1.

$$E[\psi_i] = \int V_{ion}(\mathbf{r}) n(\mathbf{r}) d^3\mathbf{r} + \frac{e^2}{2} \int \int \frac{n(\mathbf{r}) n(\mathbf{r}')}{|\mathbf{r} - \mathbf{r}'|} d^3\mathbf{r} d^3\mathbf{r}' + E_{xc}[n(\mathbf{r})] + T[n(\mathbf{r})] \quad (6\text{-}1)$$

where $n(\mathbf{r})$ is the electronic density given by $n(\mathbf{r}) = \sum_i |\psi_i(\mathbf{r})|^2$. V_{ion} is the static total electron-ion potential, E_{xc} is the exchange-correlation functional and T is the kinetic energy functional.

The set of wave function ψ_i that minimize the Kohn-Sham total energy functional are given by the self-consistent solutions to the Kohn-Sham equations shown in Equation 6-2 and 6-3.

$$\left[\frac{-h^2}{2m} \nabla^2 + V_{eff} \right] \psi_i(\mathbf{r}) = \varepsilon_i \psi_i(\mathbf{r}) \quad (6\text{-}2)$$

$$V_{eff} = V_{ion}(\mathbf{r}) + V_H(\mathbf{r}) + V_{xc}(\mathbf{r}) \quad (6\text{-}3)$$

where ε_i is the Kohn-Sham eigenvalue of electronic state i, V_{eff} is called effective potential expressed as total of all the potential terms, $V_H(\mathbf{r})$ is the Hartree potential of the electrons given by Equation 6-4.

$$V_H = e^2 \int \frac{n(\mathbf{r}) n(\mathbf{r}')}{|\mathbf{r} - \mathbf{r}'|} d^3\mathbf{r}' \quad (6\text{-}4)$$

V_{xc} is the exchange-correlation potential given by taking the functional derivative with respect to density shown in Equation 6-5.

$$V_{xc}(\mathbf{r}) = \frac{\delta E_{xc}[n(\mathbf{r})]}{\delta n(\mathbf{r})} \tag{6-5}$$

A schematic map over the iterative process to obtain self-consistency is provided in Figure 6-1. If the density equals the initial trial density, then the self-consistency is obtained. Otherwise, more iteration will be performed until a satisfactory result is reached.

As can be seen, the Kohn-Sham equations represent a mapping of the interacting many-electron system onto a system of noninteracting electrons moving in an effective potential due to all the other electrons. If the exchange-correlation energy functional were known, the exchange and correlation effects would be exactly provided.

6.1.3 Approximations for $E_{xc}\,[n(\mathbf{r})]$: LDA and GGA

The commonly used methods of describing the exchange-correlation energy are the local density approximation (LDA) and generalized gradient approximation (GGA). In LDA, it is assumed that exchange-correlation energy of an electron at point ε_{xc} is equal to that of an electron in a homogeneous electron gas of the same density [128]. Thus,

$$E_{xc}^{LDA}[n(\mathbf{r})] = \int \varepsilon_{xc}[n(\mathbf{r})]n(\mathbf{r})d^3\mathbf{r} \tag{6-6}$$

with $\varepsilon_{xc}[n(r)] = \varepsilon_{xc}^{hom}[n(r)]$. The exchange part is elementary and given by Equation 6-7 [128]

$$\varepsilon_x(n) \equiv -0.458/r_s \tag{6-7}$$

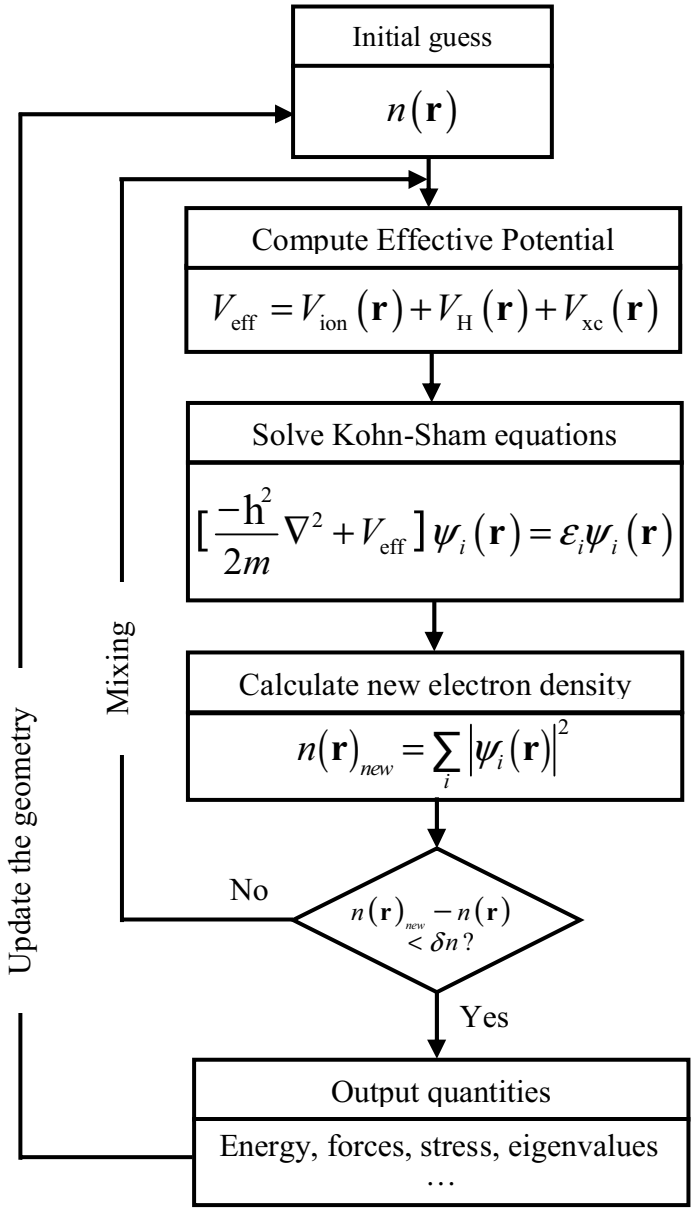

Figure 6-1. Schematic flow-chart for self-consistent density functional calculations.

where r_s is the radius of a sphere containing one electron. The correlation part was first estimated by Wigner shown in Equation 6-8 [129].

$$\varepsilon_c(n) \equiv -0.44/(r_s + 0.78) \tag{6-8}$$

and more recently with a high precision of about $\pm 1\%$ by Ceperley [130], Ceperley and Alder [131].

GGA goes beyond 'local' density approximation. The exchange-correlation functional in GGA not only depends on density $n(\mathbf{r})$, but also on gradient of the density $\nabla n(\mathbf{r})$ in account for the non-homogeneity of the true electron density. These functionals can be generally written according to Equation 6-9.

$$E_{xc}^{GGA}[n(\mathbf{r})] = \int f(n(\mathbf{r}), \nabla n(\mathbf{r}))d^3\mathbf{r} \tag{6-9}$$

Several suggestions for the explicit dependence of the integrand f on densities and their gradients exist, including semiempirical functionals which contain parameters that are calibrated against reference values rather than being derived from first principles. In principle, E_{xc}^{GGA} is usually split into its exchange and correlation contributions shown in Equation 6-10.

$$E_{xc}^{GGA} = E_x^{GGA} + E_c^{GGA} \tag{6-10}$$

The commonly used exchange functionals are functionals B88 and B86 [132, 133], P86 [134], PW91 [135, 136], and PBE [137]. The most widely used correlation functionals are P86, PW91, and LYP [138]. In principle, each exchange functional could be combined with any of the correlation functionals, but only a few combination s are currently in use,

for example, BP86 (Becke's exchange functional with Perdew's correlation functional) and BLYP (Becke's exchange functional with LYP correlation functional).

Another improvement of LDA is called hybrid approximation, introduced by Becke in 1996, where the E_{xc}^{hybrid} is calculated by linear interpolation of the exchange energy calculated with the exact Kohn-Sham wave function E_x^{KS} and an appropriate GGA E_{xc}^{GGA} [139]. The use of GGA and hybrid approximations instead of the LDA has reduced errors of atomization energies of standard sets of small molecules by factors of typically 3$\sim$5 [140]. This improved accuracy, together with the previously emphasized capability of DFT to deal with systems of very many atoms, has made DFT become the method of choice for calculating electron densities and energies of most condensed-matter systems, as well as large, complex molecules and clusters.

6.2 Plane-Wave Basis Set and Pseudopotential

Plane waves have many advantages over other types of basis sets [141]. Slater or Gaussian functions are mathematically simple to implement, and the convergence of the calculations can be easily controlled by using plane-wave method. The plane-wave basis is also independent of atomic positions, which is very convenient for coding.

According to Bloch's theorem, the electronic wave function can be written as a sum of discrete plane-wave basis set shown in Equation 6-11 [142].

$$\psi_i(\mathbf{r}) = \sum_{\mathbf{G}} C_{i,\mathbf{k}+\mathbf{G}} \mathbf{exp}[i(\mathbf{k}+\mathbf{G})\cdot\mathbf{r}] \tag{6-11}$$

where **k** is wave vector, and **G** is reciprocal lattice vector. The plane-wave basis set can be truncated to include only plane waves that have kinetic energies less than some particular cutoff energy, $(h/2m)\left|\mathbf{k}+\mathbf{G}_c\right|^2$, to achieve a finite basis set. However the basis set will still be intractably large for systems that contain both valence and core electrons.

The pseudopotential approximation overcomes this problem by allowing the wave functions to be expanded in a much smaller number of plane-wave basis states. This is because in the pseudopotential approximation, the core electrons are removed and the strong ionic potential is replaced by a weaker pseudopotential that acts on a set of pseudo wave functions rather than the true wave function [143–145]. There is no need for a very large number of plane waves to expand the tightly bound core orbitals and to follow the rapid oscillations of the wave functions of core electrons. The calculation is performed with a low cutoff energy and small the plane-wave basis set. Beyond the core region, the pseudo wave function and pseudopotential are identical to the actual valence wave function and potential.
The construction of a pseudopotential is overall motivated by the following goals:

1. The pseudopotential should be as soft as possible, meaning that it should allow expansion of the valence pseudo wave functions using as few plane waves as possible.

2. It should be transferable as possible, thereby helping to assure that the results will be reliable in solid state applications.

3. The pseudo charge density should reproduce the valence charge density as accurately as possible.

There are a number of different schemes for generating a pseudopotential, two of the most commonly used including the Kleinman-Bylander pseudopotential [146] and Vanderbilt or ultrasoft pseudopotential(US-PP) [147]. The latter one allows the pseudopotential inside core region to be as soft as possible, thus greatly reduces the plane-wave cutoff needed in calculations. Despite the complication of generating the US-PP, the computational cost is negligible compared with the cost of the large scale calculations. In this thesis, US-PP is used in all DFT calculations.

6.3 The Vienna *Ab-initio* Simulation Package

The calculations in the following chapters are performed with the Vienna *Ab-initio* Simulation Package (VASP) [148–151]. VASP is a complex package for performing *ab initio* quantum mechanical/molecular dynamics (QM/MD) simulations using pseudopotential or the projector-augmented wave method and a plane wave basis set. The expression *ab initio* means that only first principles are used in the simulations, no experimental data are needed.

VASP has a large amount of settings and specifications available for tailoring the calculations. Some of the features that I have used will be briefly described in the appendix B as an example of how to start a pseudopotential plane-wave DFT calculation for a particular system using VASP.

Chapter Seven

Interactions of Hydrogen with Pd and Pd/Ni Alloy Chain Functionalized Single Walled Carbon Nanotubes from Density Functional Theory

* Accepted by the *Journal of Physical Chemistry B*

7.1 Abstract

Density functional theory is employed to study Pd and Pd/Ni alloy monatomic chain-functionalized metallic single walled carbon nanotubes SWNT(6,6) and semi-conducting SWNT(10,0), and their interactions with hydrogen molecules. The stable geometries and binding energies have been determined for both isolated chains and chains on SWNT surfaces. We found that continuous Pd and Pd/Ni chains form on SWNTs with geometries close to stable geometries in the isolated chains. Ni alloying improves stability of the chains owing to a higher binding energy to both Pd and C atoms. The physical properties of SWNTs are significantly modified by chain-functionalization. SWNT(10,0) is transformed to metal by either Pd or alloy chains, or to a smaller gap semiconductor, depending on the Pd binding site. From calculations for H_2 interactions with the optimized chain SWNT systems, the adsorption energy per H atom is found to be about 2.6 times larger for Pd/Ni chain-functionalized SWNTs than for pure Pd chain-functionalized SWNTs. Band structure calculations show that the SWNT(10,0) reverts back to semiconductor and SWNT(6,6) has reduced density of states at Fermi level upon H_2 adsorption. This result is consistent with the experimentally observed increase of electrical resistance when Pd coated SWNTs are used as H_2 sensing materials. Finally, our results suggest that Pd/Ni-SWNT materials are potentially good H_2 sensing materials.

7.2 Introduction

Recently, modifications of single walled carbon nanotubes (SWNTs) have attracted much interest because they allow control of the properties of bare tubes [36, 37]. A carbon nanotube with adsorbed metals can significantly change its physical properties, thereby providing a useful means for manipulating electron transport, which is of value in microelectronic device design [152]. Our interest is in gas sensing materials. For example, Pd nanoparticle modified SWNT based sensors are shown to exhibit high sensitivity and fast response to hydrogen at room temperature [22, 39]. Pd coated SWNTs have also shown some advantages over conventional sensors for methane detection, while bare SWNTs show no response to methane [40]. It is expected that advanced gas sensors can be constructed from these metal functionalized carbon nanotubes. Thus, theoretical studies of interactions of metal atoms with SWNTs and their response to hydrogen gas are useful to understand and evaluate their potential for fabricating microelectronic gas sensor devices. The interaction of single metallic atoms with SWNTs has been systematically studied lately, using density functional theory (DFT) [153, 154]. However, not much attention has been given to the continuous metal atom functionalized, especially metal alloy functionalized SWNTs [155, 156]. Gas interactions with metal and alloy functionalized SWNTs have also received very little theoretical treatment so far. Such studies have the potential of not only explaining sensors mechanisms but also of suggesting improved sensing materials. Issues such as the stability and structure of sensing material upon gas adsorption and nature of bonding can be addressed with DFT calculations using pseudopotential and plane wave methods. The pseudopotential approach is based on the discrimination between core and valence electrons. It considers the chemically inert core electrons together with the nuclei as rigid non-polarizable ionic cores, so that only the valence electrons have to be dealt with explicitly, and thereby significantly reduces the computational cost [157]. The pseudopotential plane

wave method for DFT calculations has been developed and perfected over many years into a reliable tool for predicting static and dynamic properties of molecules and solids [158]. This method has been widely used in the theoretical calculations of SWNT systems, including functionalizations and interactions with gas molecules [159–161].

In this paper, we use DFT methods to study both pure Pd and Pd/Ni alloy monatomic chain-functionalized SWNTs and their interactions with H_2 molecules, because Pd is a well known element used in H_2 sensing materials [2, 7, 162]. Prior research has shown the possibility of forming isolated single atomic chains [163–170]. Electron beam evaporated Pd and Ni were shown to coat SWNTs with reasonable adhesion, indicating the possibility of experimentally realizing chain and cluster functionalized SWNTs with these metals [171]. Therefore, a chain-functionalization study by DFT can be used to examine the stability of chain-SWNT materials as well as to demonstrate a higher adatom coverage, compared to single atom functionalization, thus better mimicking systems used in experiments. Ni is used as Pd-alloying element because, like Pd, Ni can also quickly adsorb H_2, hence is widely used in hydrogenation catalytic reactions [172]. Moreover, Ni has been shown to be important for hydrogen sensors for improving reliability and speed of the sensor response in detecting hydrogen [173, 174]. Theoretically, Ni is found to also have higher binding energy on SWNT than Pd [153]. The effect of Ni on the performance of Pd functionalized CNTs is therefore of particular interest.

In this work, we perform DFT calculations on both semiconducting SWNT(10,0) and metallic SWNT(6,6), with similar diameters of 7.83 Å and 8.14 Å. First, geometries and stability of free standing infinite Pd and Pd/Ni monatomic chains are analyzed. Then, Pd and Pd/Ni chains are constructed on the tube surface to examine the formation of chain-functionalized SWNTs. Finally, H_2 molecules are added to study the interactions and sensing mechanisms. Our primary goal is to reveal the character and geometries of Pd and

Pd/Ni atomic chain-functionalized SWNTs and to understand the hydrogen interactions with these materials.

7.3 Method of Calculations

The Vienna *ab initio* simulation package (VASP) [148–151] was used to perform calculations within the generalized gradient approximation of PW91 [136] using optimized ultrasoft pseudopotentials [147, 175] and a plane wave basis set. The plane wave basis set assumes a supercell geometry that is periodic in all three directions. The single atomic chains and SWNTs were considered to be isolated and infinite in length, with lateral separation of more than 1 nm. The Brillouin zone of the supercell was sampled by Monkhorst-Pack special $1\times1\times31$ k-points [176]. Structural configurations of isolated SWNTs were fully relaxed, and all atomic positions of adsorbate and adsorbing SWNTs were optimized until residual forces were within 0.05 eV/Å.

The binding energy E_b of chain atoms per unit cell can be calculated in terms of total energy of isolated atom and the chain formed by the same atoms, see Equation 7-1 and 7-2.

$$E_b^{(Pd\ chain)} = E_T^{(Pd\ chain)} - 2E_T^{(Pd)} \tag{7-1}$$

$$E_b^{(Pd/Ni\ chain)} = E_T^{(Pd/Ni\ chain)} - E_T^{(Pd)} - E_T^{(Ni)} \tag{7-2}$$

$$E_b^{(Pd\ chain+SWNT)} = E_T^{(Pd\ chain+SWNT)} - E_T^{(SWNT)} - 2E_T^{(Pd)} \tag{7-3}$$

Similarly, the binding energies of chain atoms per unit cell on SWNTs are calculated using Equation 7-3 and 7-4. E_T is the ground state total energy for the different fully-relaxed systems, and the factor 2 accounts for the number of Pd atoms in the unit cell. In

all these calculations, there are two Pd atoms or one Pd and one Ni atoms per unit cell. Negative binding energies correspond to energetically bound species.

$$E_b^{(Pd/Ni\ chain+SWNT)} = E_T^{(Pd/Ni\ chain+SWNT)} - E_T^{(SWNT)} - E_T^{(Pd)} - E_T^{(Ni)} \qquad (7\text{-}4)$$

Pd and Ni adsorbed SWNT systems have been reported as having a zero or very small magnetic moment [153, 177]. Even so, we employed fully spin-polarized DFT calculations to observe any change in the magnetic moment of Pd and Pd/Ni chain-functionalized SWNTs.

7.4 Atomic Chain Structures

We first studied the Pd and Pd/Ni monatomic chain structures. Two configurations of chains were studied, namely, linear chain and zigzag chains. In the alloy chains, Pd and Ni atoms were located alternately. Results are shown in Figure 7-1, where the binding energy is plotted as a function of the chain unit cell length d in the chain direction. These curves show that Pd and Pd/Ni chains at local minima have larger-magnitude binding energies than in their own bulk systems, which is about -0.7 eV/bond for Pd face-centered cubic (fcc) bulk and -0.9 eV/bond for Ni fcc bulk, indicating the many atom effect in the bulk [168]. The largest-magnitude binding energy of Pd linear chain is -1.21 eV/bond, close to the -1.20 eV/bond calculated by Bahn and Jacobsen [168]. The binding energy of Pd/Ni linear chain at local minima is calculated to be larger in magnitude than that of the Pd linear chain, indicating a stonger binding of Pd-Ni than Pd-Pd.

We observe that zigzag chains have much stronger binding than the corresponding linear chains, which indicates that the preferred geometry of single atomic chain is not linear. The largest-magnitude binding energy of Pd zigzag chain can be found when Pd bonds form

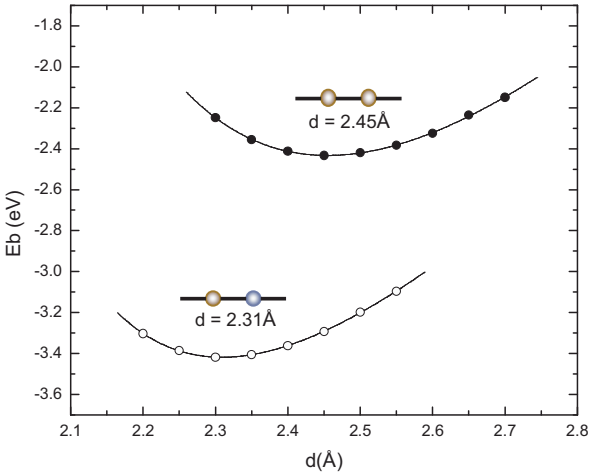

(a)

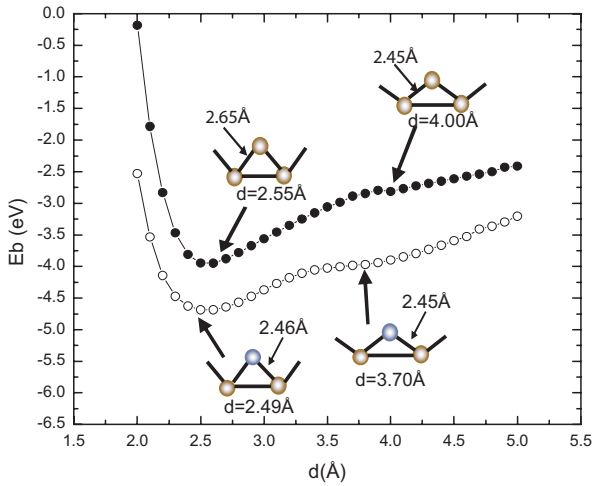

(b)

Figure 7-1. Calculated binding energy of Pd and Pd/Ni chain atoms per unit cell as function of length of unit cell d. Two geometries: (a) straight, (b) zigzag chains are shown as functions of d.The stable narrow angle and metastable wide angle zigzag chains are marked in the right figure. Black and white filled circles are for Pd and Pd/Ni chains, respectively. The binding energy is calculated from total energy difference between atomic chain and isolated atoms.

a narrow angle of 57.5°, with d=2.55 Å, corresponding to the Pd-Pd nearest neighbor (nn) distance of r_{nn}=2.55 Å, and Pd-Pd next near neighbor (nnn) distance of r_{nnn}=2.65 Å. The other meta stable state is located at d=4.00 Å, corresponding to the Pd-Pd nn distance of 2.45 Å and Pd-Pd nnn distance of 4.00 Å, with a wide bond angle of 109.1°. As seen in Figure 7-1, the Pd/Ni linear and zigzag chains have overall larger binding energies than those of pure Pd. The difference between the binding energies is about 0.25 eV smaller for the zigzag than for the linear chains. The first minimum for Pd/Ni zigzag chain appears at d=2.49 Å, which corresponds to the Pd-Pd and Ni-Ni distance of 2.49 Å, and Pd-Ni distance of 2.46 Å. The bond angle is 60.5°. The second local minimum appears for d=3.70 Å, corresponding to the Pd-Pd and Ni-Ni distance of 3.70 Å, and Pd-Ni distance of 2.45 Å, with a smaller bond angle of 98.1°.

To understand the stability and character of bonding of these three types of chains, we studied their electronic band structures and densities of states (DOS), which are shown in Figure 7-2. According to the band structure calculations, all three chains, linear, wide angle and narrow angle of both Pd and Pd/Ni species, are metallic. However, the chains undergo large changes in their band structures upon going from linear (Fig. 7-2(a) and (d)) to wide angle (Fig. 7-2(b) and (e)), to narrow angle geometry. In particular, the high density of states near the Fermi level due to d bands approaching and crossing the Fermi level in the linear Pd chain significantly reduces the magnitude of its binding energy relative to those of the zigzag geometries which, due to their larger atomic seperations, and consequently smaller d state overlap, do not form such broad d bands. A similar effect has been observed by Sen *et al.* [166] and Sanchez-Portal *et al.* [167] for monatomic gold wires. The narrower d bands of metastable broad angle Pd chain also approach the Fermi level, although they do so at the zone boundaries. Finally, the band structure of the narrow angle Pd chain reveals flat d bands lying well below the Fermi level. This geometry, which forms almost equilateral triangles, is characterized by 4 nearest neighbors, as opposed to 2 nearest neighbors in

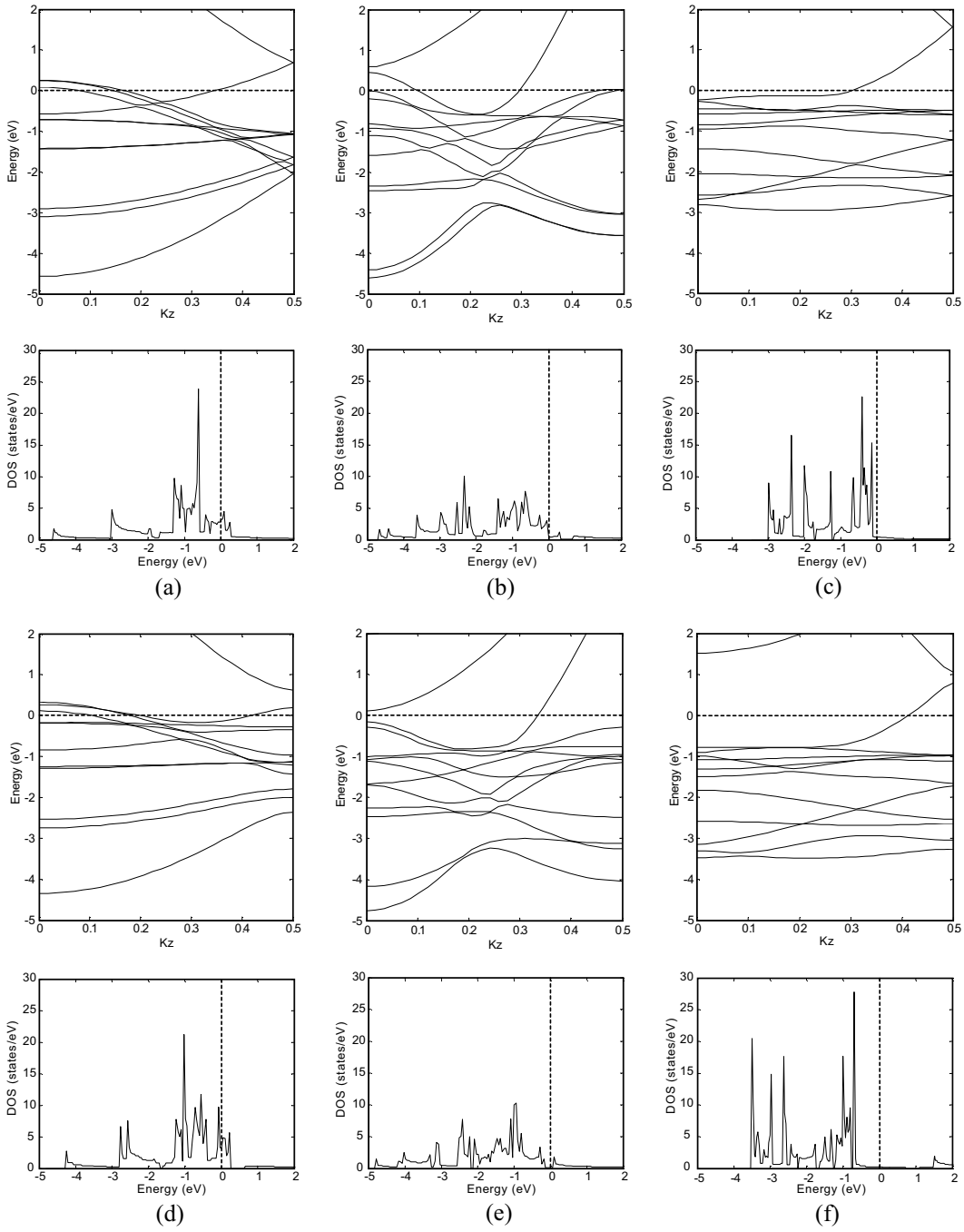

Figure 7-2. Spin-polarized band structure and DOS of the Pd chains (a-c) and Pd-Ni chains (d-f). From left to right: linear chains (a and d), narrow angle zigzag chains (b and e), and wide angle zigzag chains (c and f) shown in Figure 7-1. Bands of linear chains are folded to compare with the zigzag structures. Fermi level is set at zero energy.

the linear and wide angle chains. This fact contributes to the increase in the magnitude of the binding energy in the narrow angle Pd chain. A similar picture emerges for the Pd/Ni species with exception that now the narrow angle chain does not have d bands approaching the Fermi level. This may be reflected by its shallower local total energy minimum in Figure 7-1 compared with that for the corresponding Pd species. The overall lower lying energy bands in the Pd/Ni systems compared to the Pd result in the Pd/Ni species having relatively larger-magnitude binding energy. During the calculation, we did not observe obvious dimerization effects, such as Peierls distortion [178]. The calculations were repeated with the full-potential linearized augmented plane wave (FPLAPW) method [179, 180], and equivalent results for band structures were obtained.

7.5 Chains on SWNTs

7.5.1 Pure Pd Chain on SWNT

To form continuous chains on isolated SWNTs, each supercell contains two metal atoms along the tube direction. Due to different symmetries of (6,6) and (10,0) tubes, there are limited possibilities for placing chains on the SWNTs. Four sites were considered for Pd adsorption, as shown in Figure 7-3.

Calculations of adsorption energies have shown that for the (6,6) tube, adsorption on bridge-1 site is the strongest, while for the (10,0) tube, the strongest adsorption site appears to be the bridge-2 site. From Figure 7-1, we see that the narrow angle chain is most stable and a wide angle chain is metastable. Based on this, we decided to add Pd wide angle chains on both bridge-1 and bridge-2 sites of the (10,0) tube and Pd narrow angle chains on top sites of (6,6) tube. The bond length and bond angle of the chains are slightly changed due to the curvature of the tubes. In the calculations, we did not observe magnetic moment in the Pd chain-SWNT systems.

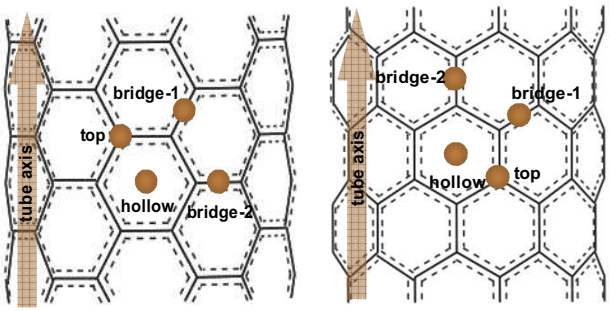

Figure 7-3. Schematic drawing of top views of four possible sites for single Pd atom adsorption on SWNT(6,6) and SWNT(10,0). Brown dots represent Pd atoms. Bridge-2 site differs from bridge-1 site in that the C-C bond is perpendicular to the tube axis at this site. In the SWNT(10,0) case, bridge-2 site is located on a C-C bond parallel to the tube axis.

The Pd chains maintain their overall initial geometries after relaxations. The angle between Pd atoms on (6,6) tube is 53.0°, with the nn distance of d=2.46 Å as in Figure 7-1. The curvature of the (6,6) tube and the stronger interactions of Pd-Pd atoms induce unequal Pd-C distance of 2.21 Å and 2.26 Å between the Pd atoms and their nearest carbon atoms. These distances are larger than the Pd-C distance of 2.10 Å formed by single Pd atom on the top site of the (6,6) tube. The bridge-1 site adsorbed Pd atoms on (10,0) tube form an angle of 107.7° with d=4.26 Å. This angle and distance d are close to those for the isolated wide angle chain, shown in Figure 7-1(109.1° and 4.0 Å). We also observed that the Pd adatoms rise above the bridge-1 site, with the Pd$-$C distance of 2.40 Å. For the (10,0) tube, the distances between the Pd atoms and their nearest C atoms are 2.13 Å and 2.12 Å, which are smaller than the 2.17 Å obtained for single Pd atom adsorbed on the bridge-1 site. The Pd chain on the bridge-2 site stabilizes at a bond angle 99.6° and $d = 4.27$ Å in its most energetically favorable geometry. Unlike bridge-1 site adsorption, both C atoms on bridge-2 sites of this (10,0) tube are only slightly further away (2.18 Å) from the carbon atoms than in the case of single Pd atom adsorption (2.14 Å). As also can be seen from cross sectional views in Figure 7-4, both types of SWNTs have slight radial

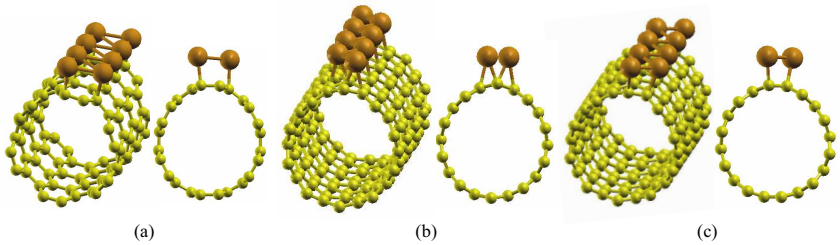

Figure 7-4. 3D view of equilibrium geometries of the Pd chain SWNT structures. (a) Pd narrow angle chain on top site of SWNT(6,6), (b) Pd wide angle chain on bridge-1 site of SWNT(10,0), (c) Pd wide angle chain on bridge-2 sites of SWNT(10,0). In all cases, changes in the tube shape are seen from the cross sectional views.

distortions from circular shape to an elliptical shape with major and minor axes of R_1 and R_2, respectivly. We calculated radial strain parameters using Equation 7-5 and 7-6 defined in terms of magnitude of changes for the tubes.

$$\epsilon_{R_1} = \frac{R_1 - R_{0_1}}{R_{0_1}} \tag{7-5}$$

$$\epsilon_{R_2} = \frac{R_2 - R_{0_2}}{R_{0_2}} \tag{7-6}$$

R_0 is radius of the undeformed (zero-strain) nanotube in the absence of Pd. It is found that the Pd chain introduces tensional strain along R_1 and compressional strain along R_2. The Pd wide angle chains on the two different bridge sites of SWNT(10,0) introduce a different radial strain with bridge-1 site producing a much larger tensional strain (for which, ϵ_{R_1}=+0.052) and compressional strain (ϵ_{R_2}=−0.020) than bridge-2 site (ϵ_{R_1} and ϵ_{R_1} are +0.027 and −0.003, respectively). The Pd narrow angle chain has a negligible effect on SWNT(6,6) with ϵ_{R_1}=6.5×10^{-4} and ϵ_{R_2}=0.

The calculated binding energies per unit cell for the chain atoms on SWNT(6,6) and SWNT (10,0) are listed in Table 7-1. The adsorption energies for the single Pd atom on

Table 7-1. Binding energy of Pd atoms per unit cell on two SWNTs. d_{Pd-C} is the distance between Pd and its nearest neighbor C atom. ΔQ is the electron charge transfer from tube to adatoms, where positive represents charge transfer to tube.

System	E_b(eV)	d_{Pd-C}(Å)	d_{Pd-C}(Å)	ΔQ(e)
Pd chain + SWNT(6,6)	-4.01	2.26	2.21	0.11
Pd chain + SWNT(10,0)†	-3.75	2.13	2.12	0.20
Pd chain + SWNT(10,0)‡	-3.81	2.18	2.18	0.22

† Values measured on bridge-1.
‡ Values measured on bridge-2.

four different sites range from ~-1.20 eV to ~-1.50 eV, and the average Pd-tube distance length is in the range of 2.10-2.18 Å [181]. In this case of Pd chain formation on carbon nanotube, due to the strong Pd-Pd binding in the chain, the binding energy per Pd atom is ~-1.88 eV to ~-2.00 eV, much larger in magnitude than that of the single atom adsorption. These values are compared with the binding energy of Ti chain on SWNTs, reported as ~-3.24 eV to ~-4.08 eV [155]. Ti shows stronger binding with SWNTs than many other metals, and can form continous wires. From results of this work, we conclude that Pd/Ni chain formation on SWNTs is energetically favored. The Pd atoms have larger binding energy on the (6,6) tube than on the (10,0) tube partially because of the stronger binding of Pd atoms in the narrow angle geometry. Comparing the two studied wide angle chains of similar geometry on bridge-1 and bridge-2 sites on the (10,0) tube, we see that although bridge-1 site chain is closer in geometry to the meta-stable isolated chain structure, the larger-magnitude binding energy appears for bridge-2 site binding. We attribute this to the larger-magnitude adsorption energy of Pd atom on bridge-2 site than on bridge-1 site of (10,0) tube as seen in our recent calculations [181].

The electronic structures of the bare as well as Pd chain decorated SWNTs for both the (6,6) and (10,0) tubes are presented in Figure 7-5 and 7-6, respectively. Figure 7-5(a) shows the band structure and electron density of state of a (6,6) tube. The conduction band

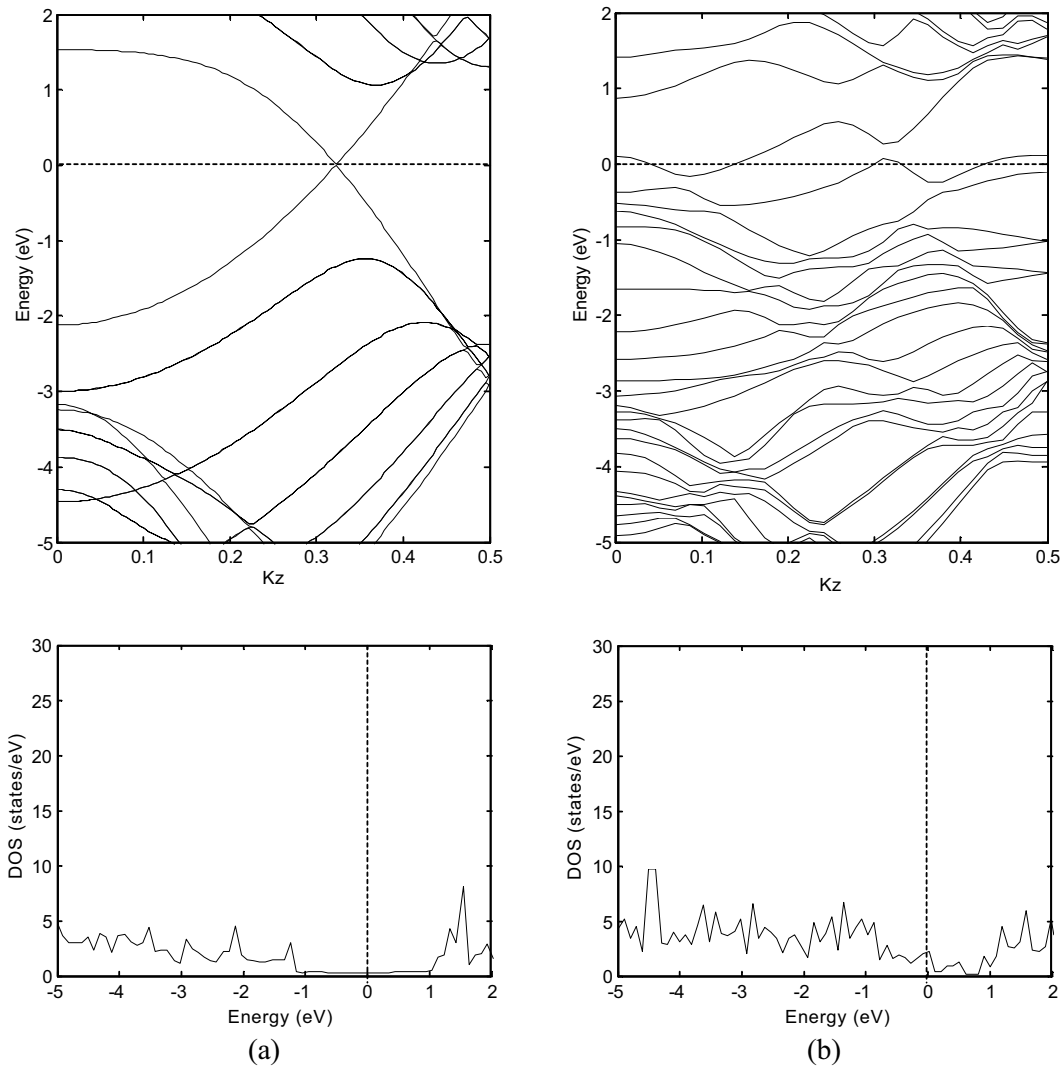

Figure 7-5. Spin-polarized band structure and DOS of (a) SWNT(6,6) and (b) Pd narrow angle chain adsorbed SWNT(6,6). Fermi level is set as zero.

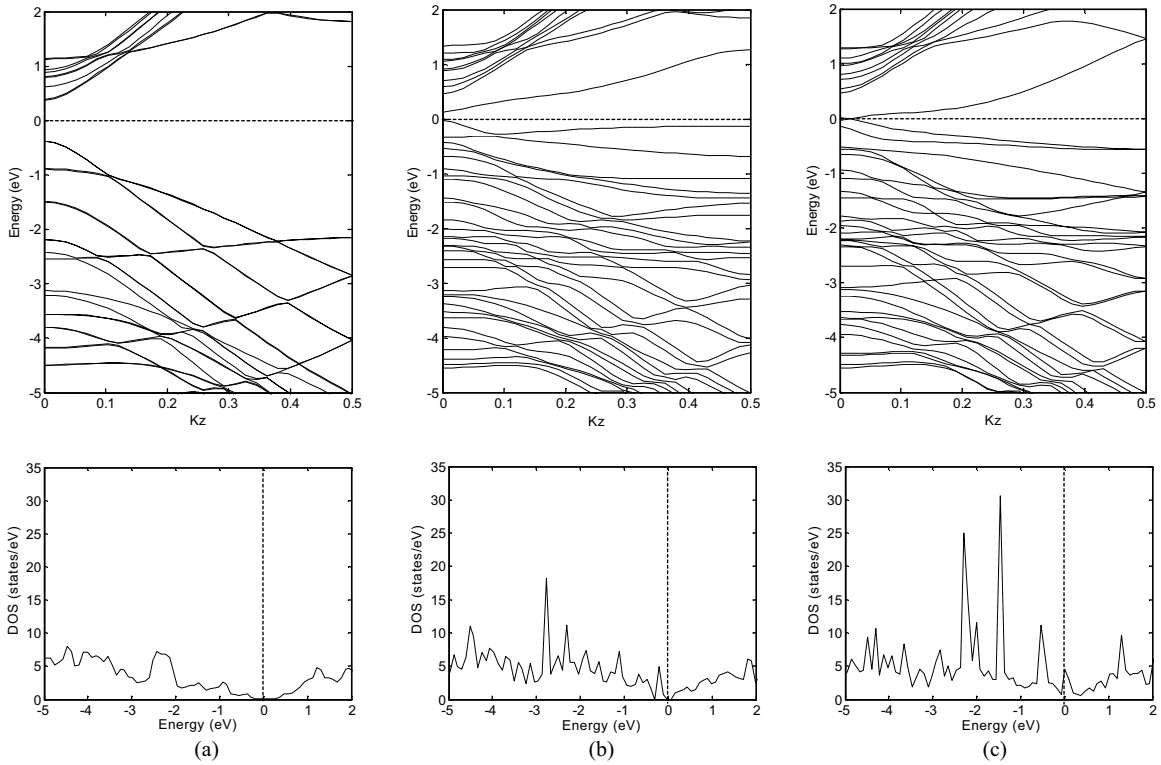

Figure 7-6. Spin-polarized band structure and DOS of (a) SWNT(10,0), (b) Pd wide angle chain adsorbed on the bridge-1 sites of SWNT(10,0), and (c) Pd wide angle chain adsorbed on the bridge-2 site of SWNT(10,0). Fermi level is set as zero.

and valence band meet at Fermi level indicating that the tube is metallic. The separation between two van Hove singularities around Fermi level is 3.65 eV, which is in agreement with results of Reich *et al.* [182]. Figure 7-6a shows the band structure and DOS of the semiconducting (10,0) tube. The band gap between the bottom of the conduction band and top of the valence band at Γ point is about 0.75 eV, also in agreement with previous results [183].

Figure 7-5(b), 7-6(b), and 7-6(c) show that upon adsorption of Pd chains, the electronic properties of both SWNTs undergo many significant changes. The originally degenerated states are split in both valance and conduction bands due to symmetry breaking of the wave function. As shown in Figure 7-5(b), the Pd-SWNT(6,6) system remains metallic. In fact,

an increase in density of states around Fermi level leads to a higher electrical conductivity of the Pd-SWNT(6,6) system. The charge transfer study [184] shows there is about 0.1 eV per unit cell electron transferred from Pd chain to the (6,6) tube. As shown in Figure 7-6(b) and 7-6(c), the band structures of (10,0) tube show different electrical property changes upon the adsorption of Pd chains on different sites. In the bridge-1 site adsorption, band gap of the bare tube is significantly reduced to a low 0.15 eV. The existence of this small gap suggests that the system is a narrow gap semiconductor material. However, when Pd chain is added on the bridge-2 sites, metallic character is observed through crossing of the Fermi level near Γ point, with DOS at the Fermi level of 4.5 states/eV. Approximately 0.20 and 0.22 electrons transfer from bridge-1 and bridge-2 site Pd chains to the (10,0) tubes, respectivly. All this suggests that different electronic properties of a carbon nanotube can be achieved through decorations of the tube by the same element on different sites.

7.5.2 Pd/Ni Alloy Chain on SWNT

Pd/Ni alloy chain-functionalized on the same tubes were studied by substituting alternate Pd atoms with Ni atoms, and then relaxing the systems. Ni atom is reported to have stronger binding with semiconducting tube (8,0) than Pd atom [153], and Ni can also improve the reliability of Pd nanomaterials, especially in hydrogen sensing applications [173, 174]. Here, we used the same initial configurations as the pure Pd chains functionalized SWNT systems, however we found the total energy was not converging during relaxation of the bridge-1 site adsorbed Pd/Ni chain+SWNT(10,0) system. Therefore, in the study of Pd/Ni alloy chains on SWNTs, we considered only two configurations, namely the narrow angle alloy chain on top site of SWNT(6,6) and wide angle chain on bridge-2 site of SWNT(10,0). Their equilibrium geometries are shown in Figure 7-7. Significant changes in the cross sectional shape of tubes are observed as shown in Figure 7-7(b). SWNT(6,6) mostly retains its circular cross sectional geometry because of the weakened Pd-C interactions induced by

Table 7-2. Calculated binding energies, charge transfer, and magnetic moment for Pd/Ni chain-SWNT system. d_{Pd-C} is the distance between Pd and its nearest neighbor carbon atom. d_{Ni-C} is the distance between Ni and its nearest neighbor carbon atom. ΔQ is the electron charge transfer from tube to adatoms, where positive value means tube gains charge.

System	E_b (eV)	d_{Pd-C} (Å)	d_{Ni-C} (Å)	ΔQ(e)	$\mu(\mu_B)$
Pd/Ni chain + SWNT(6,6)	-4.98	2.36	1.97	0.18	0.76
Pd/Ni chain + SWNT(10,0)†	-4.34	2.24	1.99	0.30	0.08

† Values measured on bridge-2.

strong Pd-Ni coupling. Again, radial strain calculation shows a negligible strain effect introduced by Pd/Ni narrow angle chain on SWNT(6,6). However the Pd/Ni wide angle chain produces +0.056 tensional strain along R_1 and -0.037 compressional strain along R_2 of SWNT(10,0), which are both much larger than for the pure Pd wide angle chain on the same site shown in Figure 7-4(c). A larger binding energy was observed than in the case of pure Pd atoms on the same tubes, as shown in Table 7-2. In both cases, we observed a much smaller distance between Ni and C atoms than between Pd and C atoms. The bond angles of Pd/Ni chain on (6,6) tube and (10,0) tube are 57.5^o and 112.3^o, respectively, very close to the angles of 60.5^o and 98.1^o in their stable geometries as isolated chains, as shown in Figure 7-1.

The spin polarized band structures shown in Figure 7-8 are similar in form to the ones obtained for SWNT(6,6) and SWNT(10,0) decorated with Pd chains, cf. Figure 7-5 and 7-6. However, we now observe splitting of the spin bands, more so in the case of Pd/Ni chain adsorbed SWNT(6,6) than in case of Pd/Ni adsorbed SWNT(10,0). We therefore conclude that the introduction of Ni atoms produces magnetic moment in the systems, higher in the case of metallic SWNT(6,6). Table 7-2 lists corresponding values for μ.

The additional bands in the band gap region are related to the delocalized states from the Pd/Ni chain. For instance, from the atom projected DOS in Figure 7-9, we can clearly

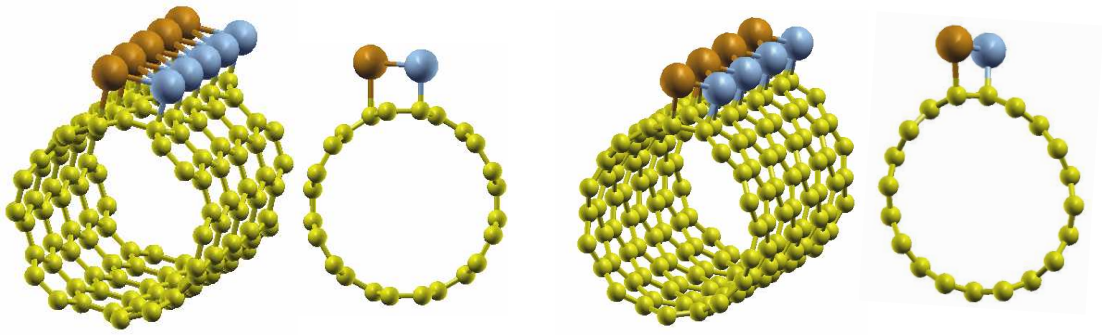

(a) (b)

Figure 7-7. 3D views of equilibrium geometries of the Pd/Ni chain-tube structures. (a) Pd/Ni narrow angle chain on top site of SWNT(6,6), (b) Pd/Ni wide angle chain on bridge-2 site of SWNT(10,0).

see that they are contributed by the states from both Ni and Pd, and the neighboring C atoms. The major binding state of Pd and Ni with their nearest C atoms appears at about -0.75 eV and -2.00 eV, respectively. This suggests a stronger binding between Ni and C than between Pd and C. To further explore the electronic interactions and delocalization of electrons belonging to Pd, Ni and SWNT, we have plotted the total electron density across various cross-sections of the Pd/Ni chain functionalized SWNTs in Figure 7-10. As shown in Figure 7-10, electrons in the area under chains are delocalized and distribute on both metal and carbon atoms. The charge transfer shown in Table 7-2 indicates that a larger number of electrons were transferred upon alloying, more onto the SWNT(10,0) than onto the SWNT(6,6). The magnetization density, defined as the difference between spin up and spin down density, shown in Figure 7-11 shows that a strong positive magnetization density located on Ni atom, indicating the magnetic moment is mostly carried by Ni, but not by Pd or tubes. Comparing the two tube systems, we notice that no magnetization density is found at SWNT(10,0) C atoms, but a low magnetization is found distributed on the C atoms on the SWNT(6,6), showing the delocalization of the magnetic moment. The distribution

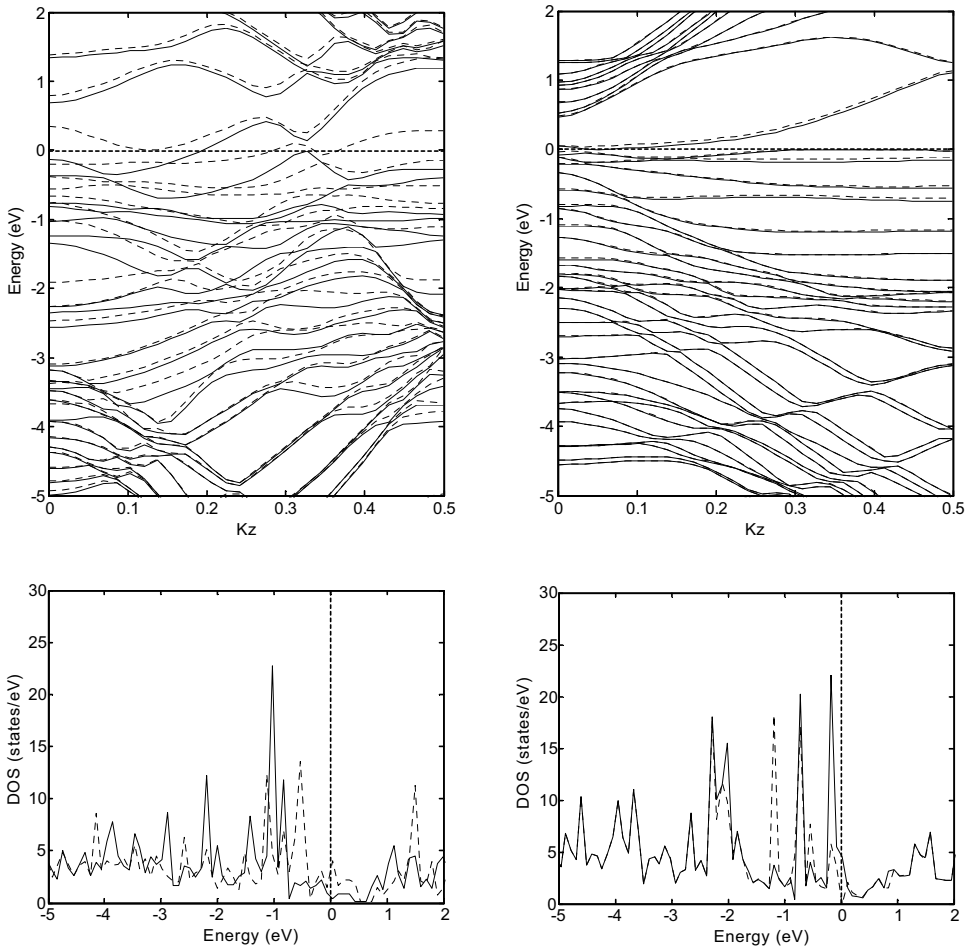

Figure 7-8. Spin-polarized band structure and DOS of (a) Pd/Ni narrow angle chain functionalized SWNT(6,6), and (b) Pd/Ni wide angle chain functionalized SWNT(10,0). Fermi level is set as zero.

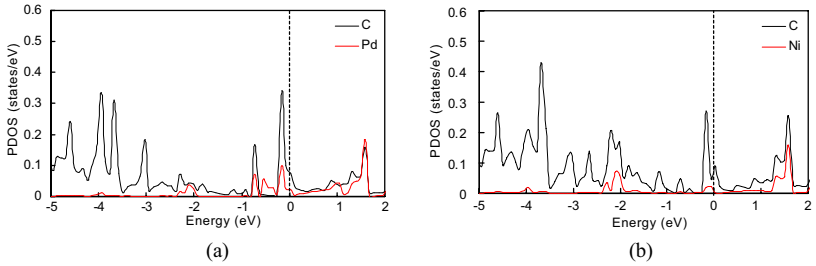

Figure 7-9. Atom projected density of state (PDOS) from (a) Pd atom with two nearest C atoms and (b) Ni atom with two nearest C atoms, on bridge-2 site functionalized SWNT(10,0).

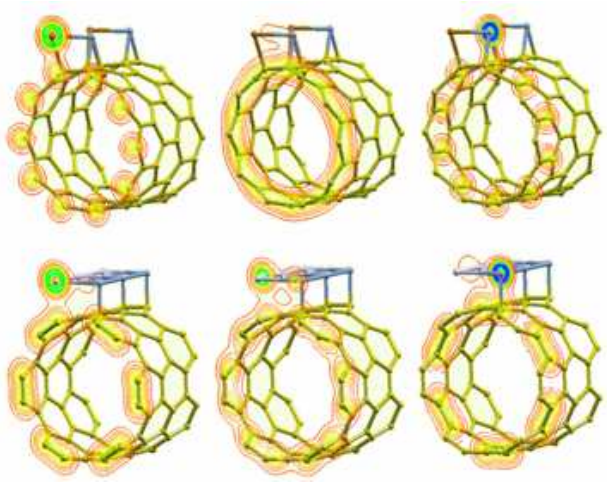

Figure 7-10. Contour plot of total (spin-up and spin-down) valence charge density on three planes for Pd/Ni chain functionalized SWNT(10,0) (upper) and Pd/Ni chain functionalized SWNT(6,6) (lower). The planes are through the cross section of the tube and different location on the Pd/Ni chain.

of the magnetization density around the Ni atom resembles different shapes in two chain-SWNT systems: a d-like orbital shape on (10,0) tube and a p-like orbital shape on (6,6) tube.

7.6 H_2 Interactions with Chain-Functionalized SWNTs

Experimentally, Pd functionalized SWNT have been studied as H_2 sensors, and good response have been observed through a large change in resistance [39]. Theoretical [185, 186] and experimental [187, 188], studies have shown that molecular hydrogen interaction with bare carbon nanotubes is a weak physisorption process, with low adsorption energy. The chemisorption state with molecule dissociation has been found as hydrogen molecule is very close to the tube surface, however approximate energy barriers of 2.5 eV [28, 189] and 3.4 eV [190] are needed to be overcome for SWNT(6,6) and (10,0), respectively, to dissociatively chemisorb a H_2 molecule onto the tube. In this section, we study the interactions between H_2 molecules and functionalized SWNTs by placing one H_2 molecule on

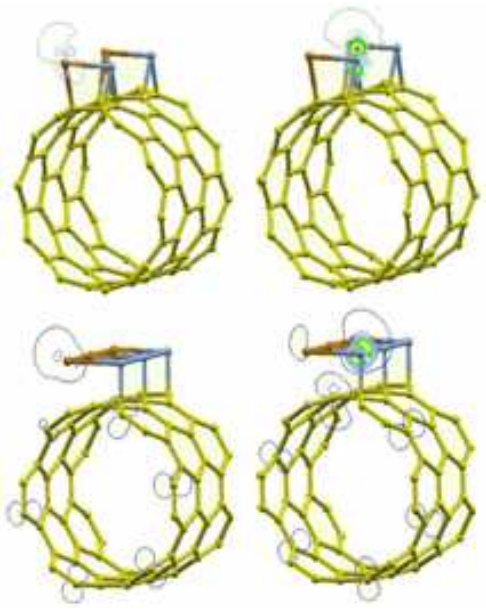

Figure 7-11. Contour plot of magnetization density (spin-up and spin-down) on two planes through Pd or Ni and the tube for the same systems as in Figure 7-10.

top of both Pd and Ni atoms. We have tried two different ways of placing H_2 molecules by letting H-H bond either parallel or perpendicular to chain-SWNT axis. After relaxing the systems, we did not observe any significant differences in final geometry or binding energy. The results shown here are from the initial structures where H-H bonds are parallel to the tube axis as shown in Figure 7-12. For a comparison of the different interactions between pure Pd chain and Pd/Ni alloy chain functionalized SWNTs, we study four out of five systems shown in Figure 7-4 and 7-7, except for the bridge-1 site Pd functionalized SWNT(10,0).

The dihydrogen complex of H_2 and Pd was reported to have an H-H bond length of 0.86 Å, and a Pd-H bond length of 1.67 Å [191]. Our calculation of a free PdH_2 gave the same result. In investigating the adsorption of a H_2 molecule on Pd and Pd/Ni chain functionalized SWNT(6,6) and SWNT(10,0), we observed the dissociation of H_2. The distance between the two dissociated H atoms is 0.83 Å on Pd and 0.86 Å on Ni on both

types of carbon nanotubes, therefore we conclude that the final geometry of individual H_2 molecule on Pd is not affected by the species of its neighbor atoms. We have calculated the adsorption energy of one H atom with respect to the H_2 molecule according to Equation 7-7.

$$E_{ad}^{(H)} = -\frac{1}{4}\left[E_T^{(chain+SWNT+4H)} - E_T^{(chain+SWNT)} - 2E_T^{(H_2)}\right] \quad (7\text{-}7)$$

We obtained the binding energies of -0.13 eV and -0.33 eV for pure Pd functionalized SWNT(6,6) and SWNT(10,0),respectively, and -0.17 eV and -0.48 eV for the same alloy functionalized systems. The negative values of these binding energies could be compared with the adsorption energy per H atom(energy gain per H atom upon adsorption of a H_2 molecule on the surface) at low to medium hydrogen coverage ($\Theta<1$) on Pd single crystal surfaces of 0.45$\sim$0.5 eV. [192, 193] Differences between our calculated values for the Pd-SWNT cases and the literature values for the Pd surfaces are from the differences in the surface coordination of adsorption sites in these different systems. Stronger adsorption is seen in the alloy functionalized systems. The adsorption energy decreases strongly with increasing hydrogen coverage. [193, 194] For example, at Θ=1.25, the adsorption energy can be as low as about half of the adsorption energy at Θ=1. Our results show that a Pd narrow angle chain functionalized SWNT(6,6) has much lower H_2 adsorption energy than a Pd wide angle chain functionalized SWNT(10,0). This is mainly because of the higher Pd local density of the narrow angle chain, which provides less open space for H_2 adsorption. We also find that Ni alloyed Pd chain functionalized tubes have higher H_2 adsorption energy compared to the pure Pd functionalized tubes. This seems to conflict with the fact that Ni-alloying decreases H_2 sensitivity in sensor application. However, an alloying induced sensitivity decrease is usually seen in the experiments where film thickness is from about 50 to about 2000 nm. In that case, a H_2 diffusional transport is mainly responsible for the

sensitivity, in other words, the magnitude of the response. Since the diffusion coefficient for H atoms in Pd is about 10^2 times larger than in Ni at room temperature [195], we usually see a decreased sensitivity of hydrogen sensors when Pd is replaced by Ni. If the hydrogen diffusion process is not a limitation, such as when an atomically thin film is used, then we would see a better H_2 sensitivity on Ni, as Ni has a higher H_2 adsorption energy than Pd [192, 196, 197]. This is also why we see larger adsorption energy when Pd/Ni alloy chains are decorated on both types of SWNTs.

Adsorption of H_2 molecules changes the geometry of chains on the tubes in two aspects, as shown in Figure 7-12: the bond angle of metal chains and the distance between metal atoms and carbon atoms. From the calculations, we have seen the overall bond angles of atomic chains decrease with an almost unvaried d. For example, the bond angle of pure Pd chain on SWNT(6,6) and (10,0) decrease to 49.3^o and 97.6^o from 53.0^o and 99.6^o, and alloy chains decrease to 52.8^o and 106.0^o from 57.5^o and 112.3^o. Upon H_2 adsorption, the Pd chain on SWNT(6,6) shows a large expansion, nearly separating the zigzag chain into linear chains. Other systems also have shown different degrees of chain expansion toward two different directions. This is mainly caused by the H repulsion, which is larger on narrow angle chains. On the other hand, we find the introduction of H_2 molecules strengthens the metal-carbon binding by lowering the chains on the tube surface. We have observed that with H_2, Pd$-$C distances from pure Pd wide angle chain-SWNT(10,0) system increase about 1.7%, but the Pd$-$C and Ni$-$C distances from Pd/Ni chain on the same (10,0) tube show no length change. In the narrow angle chain$-$SWNT(6,6) systems, due to the significant change of the chain geometry, Pd-C distances have a slight decrease of 0.6% compared to chain-SWNT(6,6) without H_2, while Pd-C and Ni-C distances in alloy chain decrease about 3.1% and 2.2%, respectively after H_2 is adsorbed on the (6,6) tube. These observations indicate that the presence of H_2 affects the chain geometry and adatom binding with SWNT differently. For different systems, large morphology changes are observed in

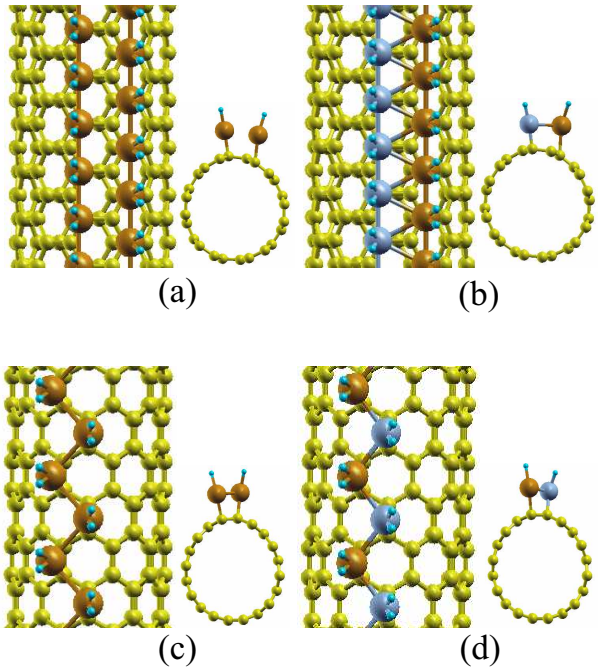

Figure 7-12. 3D views of equilibrium geometries of the H_2 adsorbed Pd and Pd/Ni functionalized SWNTs. The color scheme is same as previous figures. Small bright blue dots are hydrogen atoms. (a) and (b) are SWNT(6,6) systems, (c) and (d) are SWNT(10,0) systems.

narrow angle chain-tube systems. A strong Ni-Pd binding from Ni alloying prevents narrow angle chain from splitting and peeling from tube surface upon exposure to H_2. As for the carbon nanotube geometry, from Figure 7-12 and axial strain parameter calculations, we find that H_2 produces less strain to functionalized (10,0) tubes, where the initial distortion by Pd and Pd/Ni functionalization shown are maintained. The largest H_2 induced tube geometry change is observed on pure Pd chain functionalized (6,6) tube due to the chain splitting, where tensional strain along R_1 is $+0.025$ and compressional strain along R_2 is -0.033.

In Figure 7-13, we present the band structure and DOS for the four systems. We note that the adsorption of hydrogen changes the electronic properties of chain functionalized SWNTs. The electron density of states of the (6,6) tubes around Fermi level (Fig. 7-13(a)

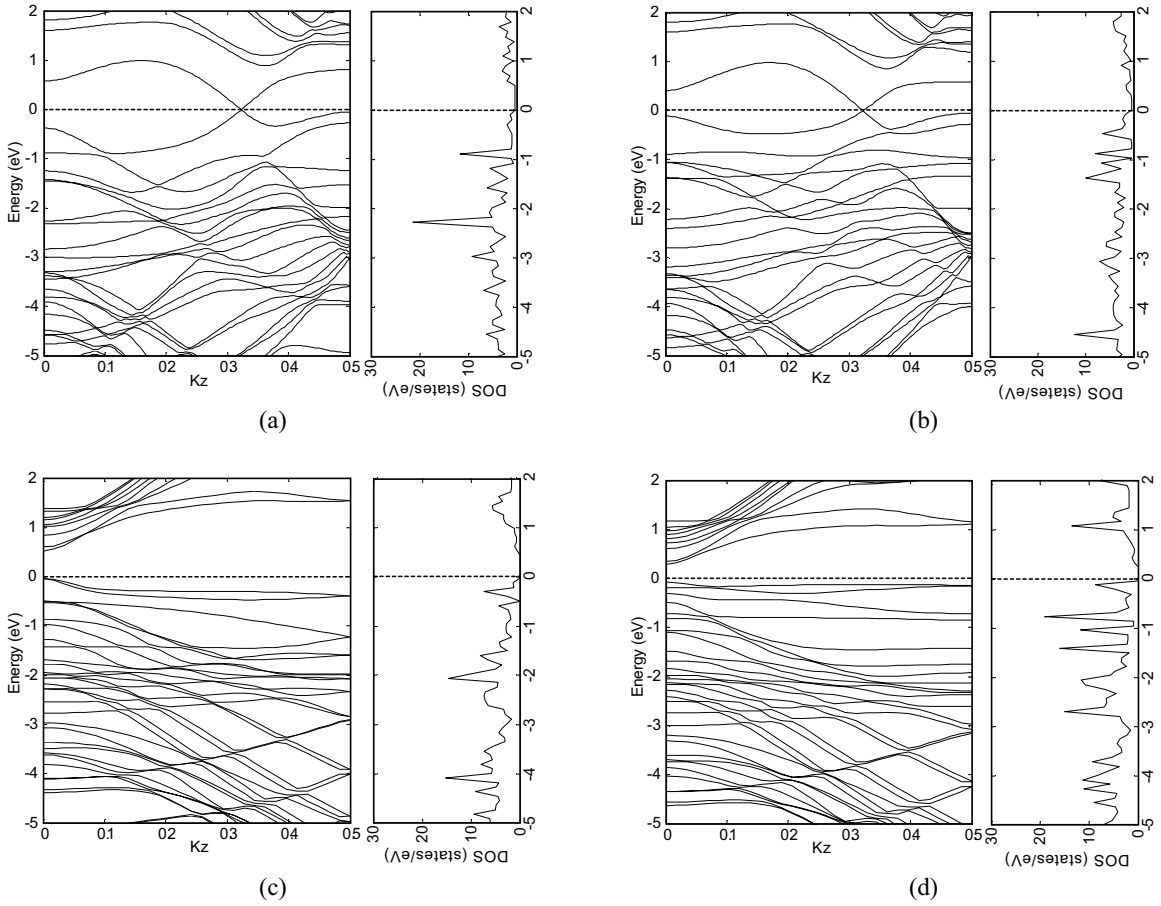

Figure 7-13. Band structure and DOS for the four systems shown in Figure 7-12.

and 7-13(b)) decreases significantly compared to the DOS of Pd-chain-SWNT(6,6) (Fig. 7-5(b)) and of Pd/Ni-chain-SWNT(6,6) (Fig. 7-8(a)). In Figure 7-13(c) and 7-13(d), we see the band gap of 0.58 eV and 0.35 eV at Fermi level in Pd and Pd/Ni chain functionalized (10,0) tubes, indicating the systems are transformed back from metal to semiconductor. Both the decrease of electron density of states in the SWNT(6,6) systems and the band gap opening in the SWNT(10,0) systems imply a significant increase of electrical resistance of the material. This result is consistent with experimental observations from other groups, where Pd coated SWNTs have been utilized in H_2 sensing [22, 39]. In these experiments, an individual Pd coated semiconducting SWNT [22] and a Pd coated thin, uniform SWNT film [39] were used, respectively. Both experimental results show dramatic, reversible increase of resistance of the sensing materials upon exposure to hydrogen gas flow, indicating Pd coated SWNTs have very good sensitivity for H_2 detection. The single tube sensor configuration utilized by Kong *et al.* [22] consists of discrete Pd particles decorating the tube surface, while the random matrix of surface-dispersed SWNTs [39] were connected with a more or less continuous Pd film. In comparison, our calculations are for a continuous monatomic wire on the SWNT. Both the literature reported experimental results and our DFT calculations show that the resistance increases upon H_2 exposure. If we construct a series-parallel array of resistances composed of metal and SWNT segments as an equivalent circuit, then our DFT calculations can be interpreted to indicate that both continuous coating by metal and decoration by discrete particles of both metallic and semi-conducting SWNTs lead to the same response of increased resistance in hydrogen sensor applications. However, the magnitudes of response depend on the nature of the tube, being larger for semi-conducting SWNTs. Charge transfer upon H_2 adsorption would indicate whether the resistance change is primarily in the tube or coating. Our analysis shows that H atoms are slightly negatively charged and the originally negatively charged SWNTs gain more charge. Pd and Pd/Ni functionalized SWNT(6,6) both gain 0.14 e, and SWNTs(10,0) gain 0.03 e

and 0.06 e, respectively. Thus, upon H_2 adsorption, the two functionalized SWNT(6,6) gain about 0.1 e more charge than the two functionalized SWNT(10,0). Pd/Ni chains do not bring significantly larger amount of charge transfer to both types of SWNTs than Pd chains. The extra charge transfer from chains to SWNTs is due to the H_2 adsorption, which readjusts the positions of Pd and Ni atoms on the tube surface and cause charge redistributions between chains and SWNTs. This is especially true for the SWNT(6,6), where the narrow angle geometry yields a large chain expansion or splitting after adsorbing H and induces a significant charge redistribution. These charge transfer results suggest that H_2 sorption brings more electrons to the initially negatively charged SWNT from the chain functionalization. While this may indicate a decrease in tube resistance, the overall system resistance is indicated to increase from the band structure and DOS results. Hydrogenating of the metal appears to increase resistance significantly.

Finally, we note that after H_2 adsorption, the initial magnetic moment carried by the Pd/Ni systems disappear and the systems turn nonmagnetic. The demagnetization of Ni bulk and surface by H_2 adsorption were understood as the involvement of the Ni d-states with H s-state, which tends to make d-shell more nearly full and as a consequence considerably reduces the magnetic moment [198, 199].

7.7 Conclusions

In this work, we have presented a detailed analysis of formation of atomic Pd and Pd/Ni chain structures and their interactions with SWNT(6,6) and SWNT(10,0). We found that zigzag chains are energetically more favorable than linear chains, and the overall binding energy is higher in the Pd/Ni alloy chains than in the pure Pd chains. The addition of Pd and its alloy chains on the tube surface modifies the electronic structure of both types of SWNTs. The chains have similar geometry on the tube surface as in their isolated states, showing stable continuous Pd and Pd/Ni monatomic chains can be formed on SWNTs.

The increase of electron density of states around Fermi level enhances the conductivity of SWNT(6,6), whereas the additional states from chains at band gap region effectively transforms SWNT(10,0) into a metal. Charge transfer phenomenon is observed from chain to the tube in all the cases, with a larger amount being transferred from the alloy chain. The Pd/Ni chain also induces a magnetic moment in the tube. We observe that the Pd/Ni narrow angle chain functionalized SWNT(6,6) has much larger magnetic moment than the wide angle chain functionalized SWNT(10,0). Spin density shows the magnetic moment to be mostly concentrated on Ni atoms but on different orbitals determined by the interactions between Pd and Ni in the chains.

Calculations of H_2 interactions with these metal and alloy chain functionalized SWNTs show different degrees of geometrical changes. Due to repulsion between H atoms, the Pd-chain-SWNT(6,6) shows the largest expansion. Our results show that Ni can improve the stability of Pd chain on tube surface, as well as increase the hydrogen adsorption energy. The electronic property calculations indicate a decrease of electron density of states at Fermi level in the functionalized SWNT(6,6), and band gap reopening in the functionalized SWNT(10,0) which turns a metallized (10,0) tube back to semiconductor. These electronic property changes can significantly reduce the conductance of the tubes, which explains the reported experimental observation on Pd functionalized SWNTs in hydrogen sensor applications.

Chapter Eight

DFT Study of Pd Functionalized Carbon Nanotubes as Hydrogen Sensors

8.1 Abstract

Density functional theory is employed to study the performance of Pd functionalized single walled carbon nanotube as hydrogen sensors. Our results demonstrate that axially discrete Pd monatomic coating is able to metallize the semiconducting SWNT. A significant decrease of electrical conductance upon hydrogen adsorption is observed due to the electron saturation of Pd d state, which brings it below Fermi level. An examination of SWNT fully coated with Pd indicates Pd atoms are able to distribute evenly on the SWNT surface without destroying the morphology of the tube. It is expected that both Pd partially functionalized and fully coated SWNTs can be used as hydrogen sensor.

8.2 Introduction

Recently, great advances have been made in demonstrating the viability of using carbon nanotubes as a valuable platform for the development of sensitive gas detectors. Surface functionalization of carbon nanotube has been of much interest because it enhances the properties of bare SWNT for many purposes. The functionalization of carbon nanotube offers further scope for improving the sensing performance and for detecting wide range of gas species that are not detectable by bare carbon nanotubes [22, 39, 40, 200–203]. For example, bare single walled carbon nanotube (SWNT) has no response to hydrogen, however, Pd nanoparticle modified SWNTs are shown to exhibit high sensitivity and fast

response to hydrogen at room temperature, seen by a significant electrical conductance drop upon exposure to small concentrations of H_2 [22, 39]. Even though these recent work have shown that functionalized SWNTs achieve much success in gas sensing, it also raises many unanswered questions, such as: whether the sensing capability is permanent [160]; how the gas interaction affects the functionalized carbon nanotube and if the advantages of intrinsic carbon nanotube maintained; if charge transfer theory can explain for the electrical properties change; etc. Theoretical studies of functionalized SWNT and its interaction with gas molecules can help develop a better understanding of the sensing mechanism and evaluate the potential for fabricating molecular sensor devices from these sensing materials.

In our previous study, we found a Pd chain metallizes semiconducting SWNT(10,0). This metallicity disappear upon H_2 adsorption, which would imply a conductance modulation consistent with experimental observations [22, 39]. In this previous study, the continuous Pd monatomic chain was placed along the axial direction of the SWNT. Both of the chain and tube were considered to be infinitely long. In this paper, we study another class of chain-functionalized SWNT systems, where Pd atoms are distributed discretely along the nanotube axis, but form continuously along the nanotube circumference.

In addition, we also study a SWNT fully coated with Pd. Experimentally, SWNTs fully coated with various metals have been demonstrated by Zhang *et al.*, where Pd is shown to be able to form a semicontinuous coating on SWNT [171]. Theoretically, Ga or Ti fully coated SWNT systems have been studied [204, 205]. The metal atoms attached on each hollow site of SWNT (8,0) exhibit a nonuniform distribution. The interactions between metal and carbon nanotube were severely weakened and the tube cross section had an obvious deformation to either an elliptical or square-like shape. Here, we show that Pd monatomic layer can be formed evenly on SWNT(10,0) without obvious distortion of the intrinsic tube. A potential of using fully coated SWNT and regional functionalized SWNT as hydrogen sensor is also discussed.

8.3 Method of Calculations

The Vienna *Ab-initio* Simulation Package (VASP) [148–151] was used to perform calculations within the generalized gradient approximation of PW91 [136] using optimized ultrasoft pseudopotentials [147, 175] and a plane wave basis set. The functionalized SWNT was considered to be isolated and infinite in length, with lateral separation of more than 1 nm. The Brillouin zone of the supercell was sampled by Monkhorst-Pack [176] special $1\times1\times31$ k-points. Structural configurations were optimized until residual forces were within 0.05 eV/Å.

8.4 Results and Discussion

In order to construct an axially noncontinuous Pd chain-functionalized SWNT system, the Pd monatomic chain, containing 20 Pd atoms per supercell, is placed around carbon nanotube on bridge-2 sites, as shown in Figure 8-1. Two carbon nanotube primitive unit cells containing 80 C atoms are used in each supercell. Each radial chain is separated of about 8 Åon the SWNT surface, therefore is considered noncontinuous along nanotube axis. In this chapter, only semiconducting SWNT(10,0) is studied. (According to our previous study, Pd chain-functionalized SWNT(6,6) show similar behavior as chain-functionalized SWNT(10,0).) Semiconducting carbon nanotubes are more commonly used in conductivity based hydrogen sensors rather than metallic carbon nanotubes [22, 28, 206].

The calculated electronic band structures near Fermi level are presented in Figure 8-2(a) and (b). A bare SWNT(10,0) is a semiconductor having a band gap of 0.75 eV. Pd radial chain increases the Fermi energy and yield additional flat spin-up and spin-down bands in the band gap of the bare SWNT. This agrees with the calculated magnetic moment of 1.2 μB of the system. The SWNT(10,0) is metallized upon on Pd adsorption in the form of a radial chain because the bands cross the Fermi level due to increase of Fermi energy

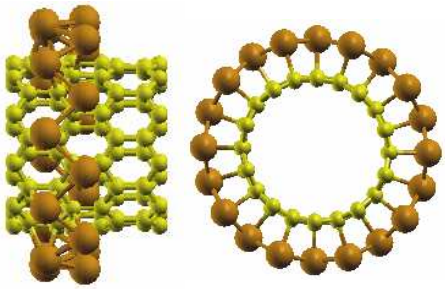

Figure 8-1. Equilibrium geometries of Pd radial chain-functionalized SWNT(10,0).

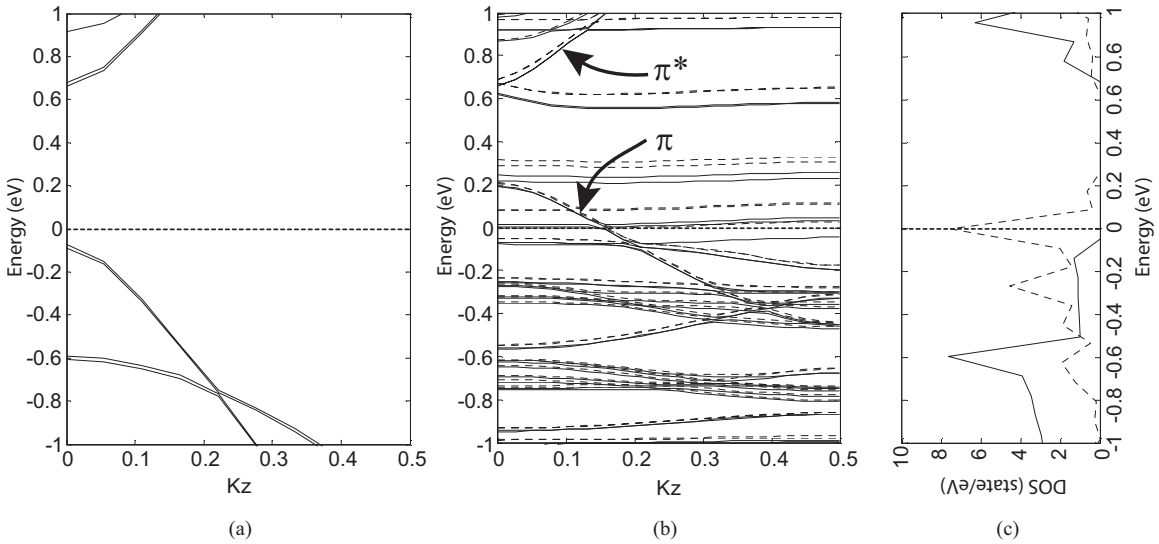

Figure 8-2. Spin-polarized band structure of (a) bare SWNT(10,0) and (b) Pd radial chain-functionalized SWNT(10,0). (c) The density of states of C atoms in a bare SWNT(10,0) and functionalized SWNT(10,0) are shown as solid and dotted line, respectively . Fermi level is set at 0 eV (horizontal dotted line).

and the hybridization between C p states and Pd d states. The original gap between the SWNT(10,0) binding (π) and anti-binding (π^*) bands reduce to $\sim$0.45 eV. The summation of DOS of 80 C atoms in Figure 8-2(c) exhibiting high density at Fermi level, implies such a transform is contributed by the carbon nanotube. Charge transfer analysis shows a total of 2.1 electrons were transferred from Pd to the SWNT, which is accordance with the band structure and DOS results.

The binding energy per Pd atom per super cell, calculated from Equation 8-1, is -1.9 eV. This indicates Pd atoms in radial chain-functionalized SWNT have stronger binding energy than that of a single Pd functionalized SWNT, which is known to be -1.5eV from previous calculations. We note that this value of -1.9 eV is almost same as the binding energy of Pd in a axial chain-functionalized SWNT, implying the chain geometry has negligible effect on binding energy when the Pd are placed in the same sites, such as the bridge-2 site in this case.

$$E_b^{(Pd)} = \frac{1}{N}\left[E_T^{(SWNT+NPd)} - E_T^{(SWNT)} - NE_T^{(Pd)}\right], N = 20 \tag{8-1}$$

A shorter average nn Pd-C distance of 2.13 Å is observed in the radial chain-SWNT, compared to the corresponding distance in the axial chain-SWNT. However, the average nnn Pd-C distance increases, namely each Pd atom is no longer equally bounded by the two bridge-2 C atoms as it is in the axial chain. The average angle between Pd atoms is 88.6°, with the average nn and nnn Pd-Pd distance of 2.72 Å and 3.83 Å. The decreases of nn and nnn distance and chain angle compared to the SWNT supported axial chain can be attributed to the curvature of the chain induced by the SWNT. From the cross sectional view in Figure 8-1, the tube does not appear to be distorted as shown in Figure 7-4, where an elliptical shape with a major axis under Pd chain is seen. The measurement of radial distance along the circumference of the SWNT indicates the adsorption of Pd atoms slightly

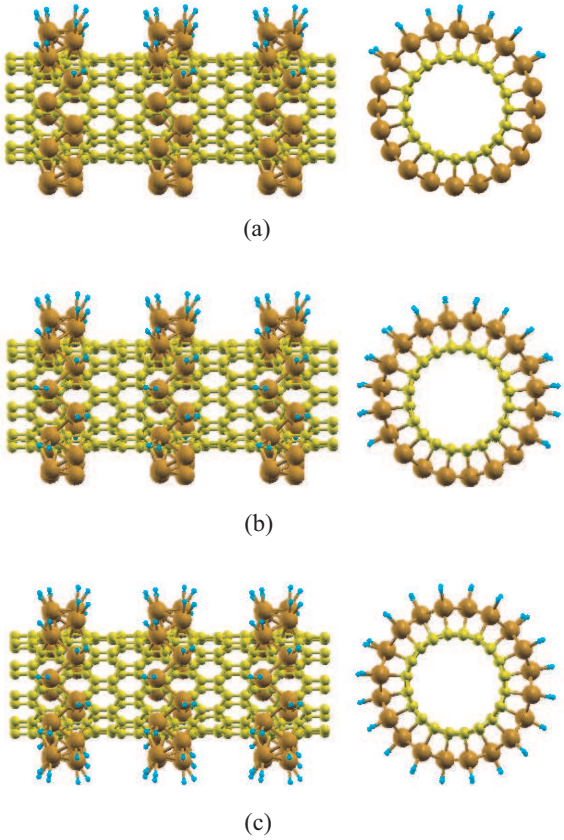

Figure 8-3. 3D views of equilibrium geometries of hydrogen adsorbed Pd radial chain-functionalized SWNT(10,0). From top to bottom: Θ=0.35, 0.60, 1.00.

expands the tube diameter, where Pd radial chain is placed, by ~1%, while the diameter of the cross section not adsorbed by Pd chain is not affected.

Next we study the H_2 interactions with Pd radial chain-functionalized SWNT. Different hydrogen coverages, Θ, (Θ is calculated by the ratio of the number of H_2 molecules to Pd atoms) of 35%, 60% and 100%, are used. Their equilibrated structures are illustrated in Figure 8-3.

The adsorption energy of one H atom with respect to H_2 molecule is calculated by Equation 8-2.

Table 8-1. H_2 adsorption energies E_{ad}, averaged atomic distances $\bar{d}$, averaged nearest neighbor distances $\bar{nn}$, chain angles $\bar{\alpha}$, and magnetic moment μ for Pd radial chain-functionalized SWNT(10,0) systems with different H_2 coverage. $\bar{d}$, $\bar{nn}$ and $\bar{\alpha}$ are measured for H adsorbed Pd atoms only. The results are averaged over the number of adsorbed H_2 molecules.

Θ	E_{ad} (eV)	$d_{H-H}{}^{\dagger}$	$d_{Pd-H}{}^{\dagger}$	$\bar{nn}_{Pd-C}{}^{\dagger}$	$\bar{nn}_{Pd-Pd}{}^{\dagger}$	$\bar{\alpha}^{\ddagger}$	μ (μB)
0.00	–	–	–	2.13	2.72	89.3	1.22
0.35	0.38	0.84	1.76	2.15	2.79	88.5	0.96
0.60	0.37	0.84	1.77	2.15	2.78	86.1	–
1.00	0.37	0.84	1.77	2.15	2.79	86.3	0.00

† Values reported in angstrom.
‡ Values reported in degree.

$$E_{ad} = -\frac{1}{N}\left[E_T^{(SWNT+chain+NH)} - E_T^{(SWNT+chain)} - \frac{N}{2}E_T^{(H_2)}\right] \tag{8-2}$$

where N is the total number of H atoms. The results of H adsorption energy are shown in Table 8-1. Comparing with the axial chain-functionalized SWNT, H_2 has higher dissociative adsorption energy on the radial chain-functionalized SWNT. This can be contributed to the fact that the radial chain geometry has a smaller surface relaxation upon H_2 adsorption. This is seen from the comparison of axial and radial chain structure change before and after H_2 adsorption. Table 8-1 indicates that the distance between two dissociated H atoms and Pd-H bond length are not affected by the coverage, because every H_2 is adsorbed on different Pd atoms.

For partially adsorbed H_2 on radial chain-functionalized tubes (Θ=0.35, Θ=0.60), the nn distance of Pd radial chain in the part that is covered by hydrogen is larger than the part that is not covered, which is about the same as $\bar{nn}_{Pd-Pd}$ at Θ= 0. At the Θ=1.00, the nn of the Pd radial chain is larger than that of the unabsorbed Pd radial chain-functionalized tube. This is most likely caused by the repulsion of H atoms as also seen in the previous chapter of axial chain-functionalized tubes. Due to the adsorption of H_2 molecules, Pd atoms show a

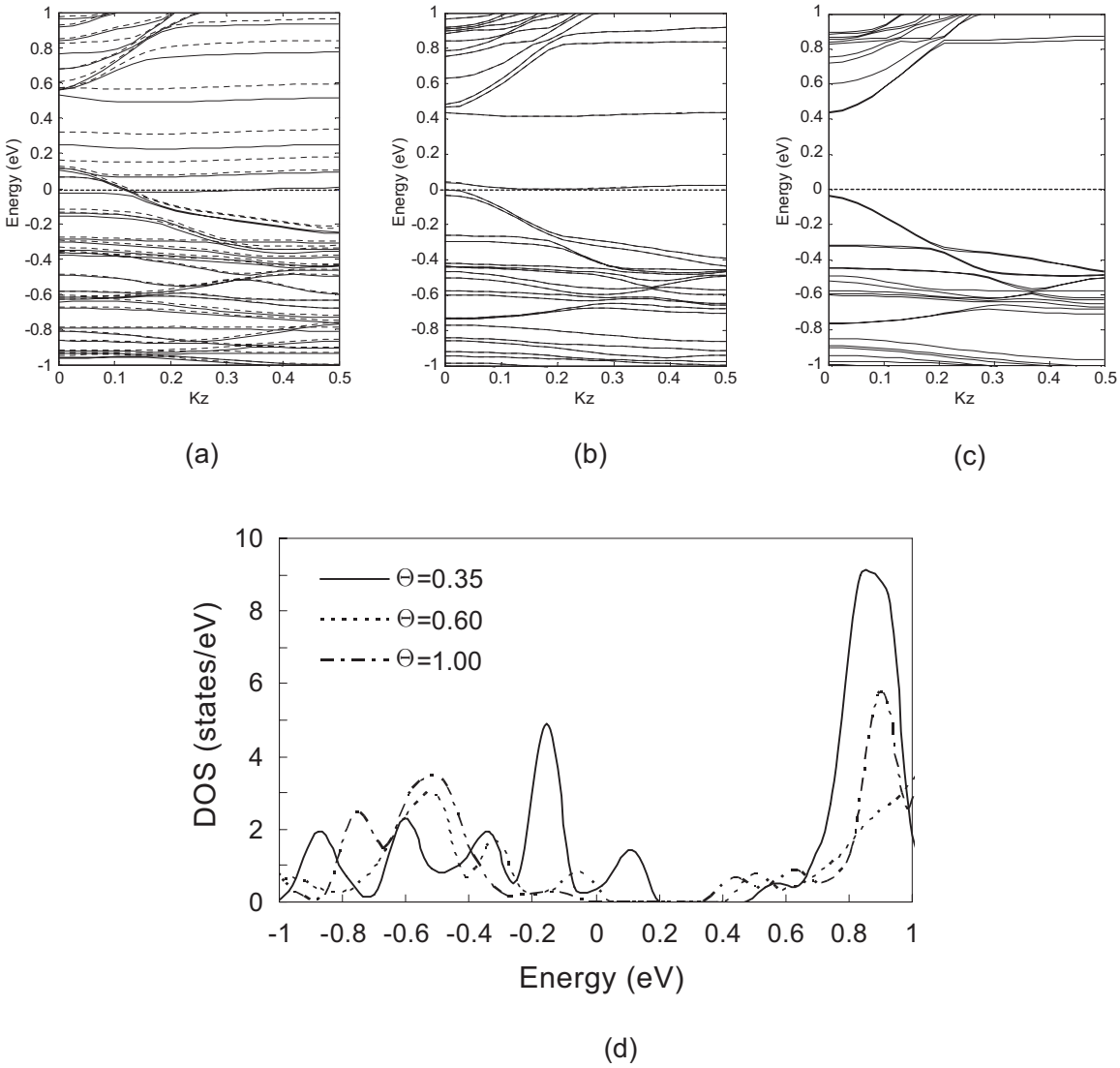

Figure 8-4. Spin-polarized band structure of hydrogen adsorbed on Pd radial chain-functionalized SWNT(10,0). From (a) to (c): Θ=0.35, 0.60, 1.00. (d) Local DOS of Pd atoms at different Θ.

slight displacement on the SWNT(10,0), however the Pd-C nn distances increase less than 1.0% with respect to the corresponding distances before H_2 adsorption. This observation is different from the axial chain-functionalized SWNT(10,0), where a larger increase of 1.7% of Pd-C distances was seen upon H_2 adsorption. Pd atoms in the radial chain have less freedom of motion than in the one dimensional axial chain on the SWNT, and this prevents these Pd atoms from moving on H_2 adsorption.

Unlike Pd axial chain-functionalized SWNT(10,0), Pd radial chain-functionalized tube has magnetic moment of 1.22 μB. The onset of magnetism is associated with the increase of density of states at Fermi level, caused by the local symmetry change, or by the increasing the percentage of Pd atoms, as discussed by Sampedro *et al.* [207]. The magnetic moment carried by the system decreases as the hydrogen coverage increases, as a results of the filled-up 4d states and the consequent reduction of density of states at Fermi level [208]. Charge density calculations show 0.005 electrons per H atom are transferred from Pd to H atoms. The electron density associated with the Pd functionalized SWNT increases by $\sim$0.2 eV at Θ=1.

According to the band structure, the hydrogen-induced band appears $\sim$8 eV below Fermi level of the Pd-SWNT system, in agreement with the value reported in the Pd-H system [209, 210]. Due to the presence of H atoms in the Pd, the Fermi energy is shifted upward relative to the d band of Pd. Prior to H_2 adsorption, the Pd d band is mostly filled. The adsorption of H atoms drastically reduces the DOS at the Fermi level with a corresponding decrease in the number of anti-bonding bands near Fermi level as shown in Figure 8-4(a) and (b). At high H coverage, the d band becomes completely occupied, resulting in a zero DOS at Fermi level. As a consequence, the band gap from the SWNT reappears at Fermi level. The gradual decrease of DOS of Pd atoms with increasing Θ can be clearly seen from the summation of local DOS of each Pd atom in Figure 8-4(d). The band structure and DOS change of Pd due to Pd hydride formation upon hydrogen

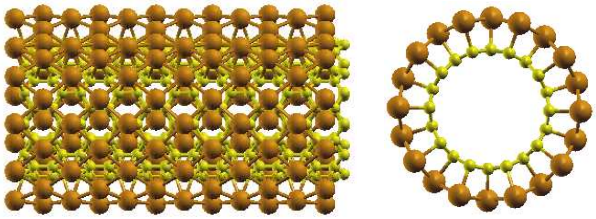

Figure 8-5. 3D views of equilibrium geometry of Pd fully coated SWNT(10,0).

adsorption has been discussed by Chan and Louie [211]. As shown in Figure 8-4(a)-(c), the metallic nature is maintained at Θ=0.35, 0.60, and band gap of $\sim$0.48 eV appears at Θ=1.00, indicating that the metallic Pd radial chain-functionalized SWNT has been transformed to a semiconductor. The resulting band gap is about the same size as the π-π^* gap of Pd functionalized SWNT before H_2 adsorption as shown in Figure 8-2(b), consistent with the charge preservation of the tube during H_2 adsorption. The reappearance of the band gap would imply a significant response in the sensor application. Since it is clear that the Pd atoms are discrete along the tube direction, our DFT calculations can be interpreted to indicate that both continuous and noncontinuous decorations by Pd of SWNT(10,0) lead to the same response of increased resistance in hydrogen sensor applications. This is in agreement with experimental observations of Kong *et al.* [22] and Sippel-Oakley *et al.* [39], where a noncontinuous Pd coated semiconducting SWNT were used [22].

We next investigate the possibility of fully coating the carbon nanotube with one Pd atomic layer. Previous experimental results reported by Zhang *et al.* reveal that for a 0.5 nm Pd coating, the discontinuity in the coating is apparent [171]. However, they also pointed out that metal coating on nanotubes could be influenced by various deposition conditions including temperature. Our calculations show that a Pd monatomic layer can be coated uniformly on SWNT(10,0) at 0 K.

Fully coated SWNT systems have been studied by Durgun *et al.* where Ga or Ti atoms attached on each hollow site of SWNT (8,0) exhibit nonuniform distribution [204, 205]. In the both studies, the interactions between metal and the tube were severely weakened and the tube cross section showed an obvious deformation to either a elliptical or square-like shape. Here, a SWNT(10,0) fully coated with Pd is constructed by placing one Pd atom on each bridge-2 site, namely, 20 Pd atoms per carbon nanotube unit cell. The system is relaxed under the same criteria as previous calculations for chain-functionalized carbon nanotubes. From the equilibrated structure in Figure 8-5, we see that Pd atoms are able to form evenly on the tube surface without any tube distortion. The binding energy per Pd atom is 2.31 eV, higher than that of chain-functionalized SWNT(10,0), owing to the stronger Pd-Pd coupling. The Pd-C distance range between 2.21 Å and 2.24 Å, indicating that the Pd is bound strongly with the C atoms. The average nn distance of Pd-Pd is 2.87 Å. Two bond angles are defined here: axial bond angle, α_1, equivalent to the bond angle described in the axial chain, and circumferential bond angle, α_2, equivalent to the bond angle of a radial chain described in this chapter. The two average bond angles in the Pd fully covered SWNT(10,0) are α_1=96.2° and α_2=82.3°, smaller than the corresponding individual bond angles of 99.6° and 89.3° calculated previously. Thus, we believe that the morphology of Pd atoms is affected by both the curvature of the carbon nanotube and the number of near neighbor atoms. The charge transfer is 0.06 electrons per Pd atom to carbon nanotube, which is about the same as the charge transferred in Pd chain-functionalized SWNTs.

The electronic structure having several band crossing the Fermi level, as shown in Figure 8-6, indicates that Pd fully coated SWNT(10,0) is highly conducting. The conductance associated with the ballistic electron transport of a 1D system is given by Landauer's equation, see Equation 8-3 [212].

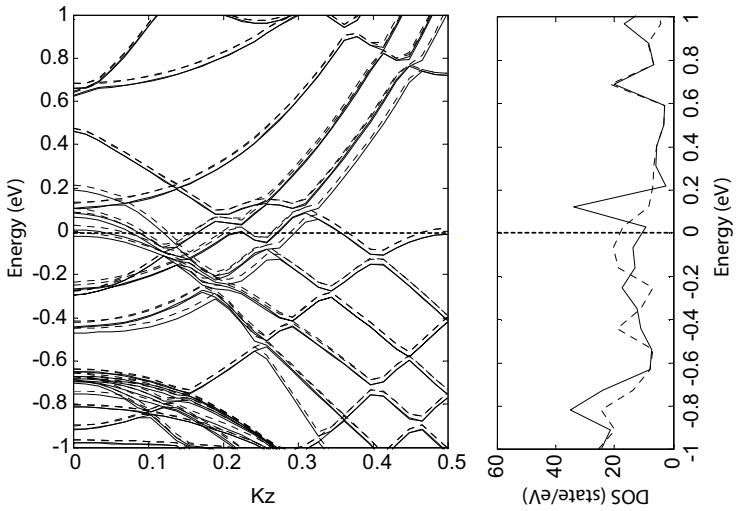

Figure 8-6. Band structure and total spin polarized density of states (DOS) of a Pd fully covered SWNT(10,0). Zero of energy is taken as Fermi level.

$$G = \frac{2e^2}{h} \sum_{i}^{N} T_i \tag{8-3}$$

where $\frac{2e^2}{h} = G_0$ is the quantum unit, and T_i is the transmission of each contributing sub-band (conduction channel) produced by the confinement of the electrons along the circumference of the carbon nanotube. In reality, T_i is reduced due to the scattering of carriers from the abrupt change of cross sections and irregularities at the contacts to the electrodes and from the imperfections, impurities, and electron-phonon scattering in the tube. [205]. We note that even though the Pd fully coated SWNT(10,0) shown in Figure 8-5 may only occur in the ideal condition, and a thick and inhomogeneous coating in the experiment may decrease the channel transmission, G is still expected to be high owing to the new conductance channel opened at Fermi level. Therefore the conductance of a Pd coated SWNT(10,0) can be several G_0.

We then study the interaction between H_2 molecule and a Pd fully coated SWNT(10,0). We notice that the adsorption energy of each H atom with respect to the H_2 molecule is

0.30 eV, about 0.3 eV lower than H_2 adsorption on the axial chain-functionalized tube and 0.7 eV lower than on the radial chain-functionalized tube. The distances from the hydrogen adsorbed Pd to its neighbor Pd atoms, as wells as to the nearest C atom increase $\sim$3.8% and $\sim$1.3% respectively. The relatively weaker interaction between Pd-Pd and Pd-C allows stronger interaction between H_2 and Pd, and hence leads to a larger H-H distance of 0.86 Å. Similar behavior has also been seen in the study of H_2 dissociation on single Pt functionalized SWNT [161]. However, one can expect that a detachment of Pd from SWNT may occur if a high H_2 coverage is applied. While this is foreseen in a fully coated Pd-SWNT system, a better control of Pd peeling from SWNT may be achieved by local decoration such as radial chain-functionalization, where Pd local density is lower. The H_2 adsorption on a Pd fully coated semiconducting SWNT is also expected to induce significant conductance change. This can be seen by comparing the local DOS of Pd atom in different locations presented in Figure 8-7. Figure 8-7 indicates that similar to the radial chain-functionalized SWNT case, the Pd that has adsorbed H_2 has much lower electron density of states than the one without H_2 on the other side of the fully coated SWNT. Therefore, as we can predict , when more H_2 molecules appear, the total DOS of the system will continue to reduce and most probably we will see a band gap when all Pd atoms are attached by H_2.

8.5 Conclusion

DFT calculations on Pd functionalized SWNTs indicate that a discrete Pd monatomic coating is able to metallize a semiconducting SWNT. The dramatic decrease of electrical conductance upon H_2 adsorption on these Pd atoms can be attributed to the filling-up of Pd d state, which brings it below Fermi level. A study of SWNT fully coated with Pd indicates that the Pd atoms are able to distribute evenly on the SWNT surface without significantly altering the morphology of the tube. Both Pd partially functionalized and fully coated

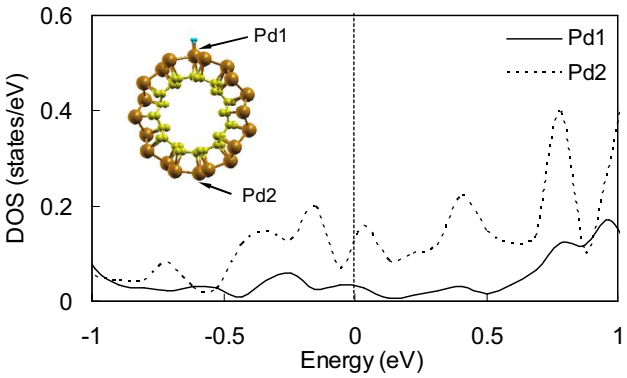

Figure 8-7. Local density of states of two Pd atoms in the fully coated SWNT(10,0). Pd1 and Pd2 are the two Pd atoms as illustrated in the inserted picture.

SWNTs appear to be suitable for hydrogen sensing due to the influence of H_2 adsorption on the metallicity of the Pd decorated carbon nanotube.

Chapter Nine

Conclusions and Proposed Future Work

9.1 Conclusions

Classical Molecular dynamics simulations and quantum chemical *ab initio* methods were used to study the properties of Pd based hydrogen sensing materials and their interactions with hydrogen gas. The first part involved the comparison studies of thermodynamic, structural and dynamic properties of Pd nanowire and nanoclusters. The simulation studies of this work indicate that the Pd nanowire has lower melting temperature than Pd bulk but higher than the same diameter Pd cluster. Both Pd nanowires and nanoclusters exhibit surface pre-melting with different the structural and dynamical behavior. Particularly, the nanowire exhibits a higher pre-melting temperature range, and dynamical behavior characterized by increased movement of atoms in the plane perpendicular to the axis followed by increased movement across these planes as the temperature approaches the transition temperature. A quasi-liquid skin grows from the surface in the radial direction for both nanocluster and nanowire, in the surface pre-melting regime, followed by the breakdown of order in the remaining solid core at the transition temperature. The nanocluster retains the initial fcc structure, whereas, the nanowire appears stable in a structure close to the hcp in the solid phase. Melting points of studied cluster and wire were characterized particularly well by the liquid-drop model for size-dependent melting. A study of graphite supported same sized Pd nanocluster was performed in order to examine the substrate effects. Several analysis reveal that supported Pd cluster has very different geometric evolution during

heating. However both unsupported and supported Pd clusters behave very similar interior structural evolutions at lower temperatures.

The second part of this study involved quantum mechanical modeling of Pd functionalized SWNTs and hydrogen interactions using *ab initio*-DFT method. A detailed analysis of formation of atomic Pd and Pd/Ni chain structures and their interactions with metallic SWNT(6,6) and semiconducting SWNT(10,0) was conducted first. It was found that zigzag chains are energetically more favorable than linear chains, and the overall binding energy is higher in the Pd/Ni alloy chains than in the pure Pd chains. The addition of Pd and its alloy chains on the tube surface modifies the electronic structure of both types of SWNTs. The increased electron density of states around Fermi level enhances the conductivity of SWNT(6,6), whereas the additional states from chains at band gap region effectively transforms SWNT(10,0) into a metal. A larger magnetic moment is observed in the Pd/Ni narrow angle chain functionalized SWNT(6,6) than the wide angle chain functionalized SWNT(10,0). Spin density calculations showed that the magnetic moment to be mostly concentrated on Ni atoms but on different orbitals determined by the interactions between Pd and Ni in the chains. The study of hydrogen interactions with chain-functionalized SWNTs show there are different degrees of chain geometry changes on the tube surfaces upon H_2 adsorption. The results indicate that Ni can improve the stability of Pd chain on tube surface, as well as increase the hydrogen adsorption energy. It is found that electron density of states decreased at Fermi level in the functionalized SWNT(6,6), and band gap reopened in the functionalized SWNT(10,0), which turns a metallized (10,0) tube back to semiconductor. These electronic property changes can significantly reduce the conductance of the tubes, which explains the reported experimental results on Pd functionalized SWNTs in hydrogen sensor applications. In addition, we perform H_2 interactions with noncontinuous Pd chain-functionalized SWNT(10,0) in order to further clarify the sensing mechanism. We note that a discrete Pd monatomic coating is also able to metallize

semiconducting SWNT. By applying different H_2 coverages, we conclude that the large decrease of electrical conductance upon H_2 adsorption is due to the filling-up of Pd d state, which brings it below Fermi level. An exploration of Pd full coating on SWNT indicate Pd atoms are able to distribute evenly on the SWNT surface without significantly altering the structure of the tube. This shows that the Pd functionalized SWNTs are hightly suited as hydrogen sensing materials.

9.2 Major Contributions

The contributions of the dissertation to the field of sensor research are multifold. It develops a fundamental understanding of the sensing materials and unravels the sensing mechanism of recently proposed hydrogen sensors. The theoretical calculations from molecular simulations in this research will not only benefit to the design of novel hydrogen sensing materials, but also establishes a good platform for the study of other gas sensing materials. This will eventually lead to a successful fabrication of high performance but low cost gas sensors.

From a broader impact perspective, this dissertation can help improve the quality of human life through better information regarding the pollutants and hazards. In the area of national security, this research will contribute to the development of improved sensing capability to guard against chemical and biological warfare agents.

9.3 Future Work

9.3.1 Sensor Poisoning

As a result of considerable evidence for hydrogen gas induced sensor response, future work should investigate how to protect the sensor from being poisoned by harmful species. This is because in real application, the environment that needs to be tested is usually a multi

component gas mixture. Species other than hydrogen in the environment may interfere with hydrogen uptake by Pd functionalized SWNTs, thus adversely affecting sensor performance. Therefore the interactions between Pd functionalized SWNT with gases that frequently appear in the ambient atmosphere, such as CO, CH_4, SO_2, need to be studied. An adsorption energy of each gas molecule on the functionalized carbon nanotube can be calculated to determine the poisoning effect on the hydrogen sensor. A possible solution to the poisoning phenomenon may be alloying Pd with ambient gas active metals.

9.3.2 Multipurpose Gas Sensor

It is expected that functionalized SWNTs can be used as a sensor array to detect various types of gases simultaneously [160]. SWNTs functionalized by different metals can form an array and thus function as a multi component gas detector. By choosing different functional materials and controlling the coating amount, one can make the functionalized SWNTs flexible enough to detect a wide range of molecular species and as well as selective to specific molecules. Hence, the future work includes the design of a multi functional carbon nanotube sensor using *ab initio* calculations.

9.3.3 *Ab initio* MD Simulations

Although quantum-mechanical *ab initio* calculations of electronic total energy are extremely useful to understand and to predict complex chemical reactions, it is limited to zero temperature. *Ab initio* MD techniques [213] allow one to calculate accurate structural and dynamic properties at finite temperature by means of atomic trajectories generated by forces obtained directly from electronic structure calculations, therefore no empirical models are needed. *Ab initio* MD has been successfully applied to a wide variety of important problems in physics and chemistry, as well as in biology in the last decade. In numerous studies, new phenomena have been revealed and microscopic mechanisms elucidated that

could not have been uncovered by using empirical methods, leading to new interpretations of experimental data and suggesting new experiments to perform [214]. Therefore, another important part of the future work is to study the sensing materials and sensing reactions at finite temperatures using *ab initio* MD techniques. Thus, questions like whether Pd functionalized SWNTs are stable at room temperature or high temperatures, will even distribution of Pd fully coated SWNTs observed at 0 K maintain at higher temperatures, and what is the effect of temperature to the sensor response, etc. can be answered through these ab initio MD studies.

References

[1] Stetter, J. R., P. J. Hesketh, and G. W. Hunter. 2006. Sensors: Engineering structures and materials from micro to nano. *The Electrochemical Society Interface* 15:66–69.

[2] Christofides, C., and A. Mandelis. 1990. Solid-state sensors for trace hydrogen gas-detection. *Journal of Applied Physics* 68:R1–R30.

[3] Graber, N., H. Ludi, and H. M. Widmer. 1990. The use of chemical sensors in industry. *Sensors and Actuators B-Chemical* 1:239–243.

[4] North, D. C. 1992. An investigation of hydrogen as an internal-combustion fuel. *International Journal of Hydrogen Energy* 17:509–512.

[5] Van Blarigan, P., and J. O. Keller. 1998. A hydrogen fuelled internal combustion engine designed for single speed/power operation. *International Journal of Hydrogen Energy* 23:603–609.

[6] Peschka, W. 1998. Hydrogen: The future cryofuel in internal combustion engines. *International Journal of Hydrogen Energy* 23:27–43.

[7] Favier, F., E. C. Walter, M. P. Zach, T. Benter, and R. M. Penner. 2001. Hydrogen sensors and switches from electrodeposited palladium mesowire arrays. *Science* 293:2227–2231.

[8] Walter, E. C., R. M. Penner, H. Liu, K. H. Ng, M. P. Zach, and F. Favier. 2002. Sensors from electrodeposited metal nanowires. *Surface and Interface Analysis* 34:409–412.

[9] Lundstrom, K. I., M. S. Shivaraman, and C. M. Svensson. 1975. Hydrogen-sensitive Pd-gate Mos-transistor. *Journal of Applied Physics* 46:3876–3881.

[10] Lundstrom, I., M. Armgarth, and L. G. Petersson. 1989. Physics with catalytic metal gate chemical sensors. *Crc Critical Reviews in Solid State and Materials Sciences* 15:201–278.

[11] Baranzahi, A., A. L. Spetz, B. Andersson, and I. Lundstrom. 1995. Gas sensitive field-effect devices for high-temperatures. *Sensors and Actuators B-Chemical* 26:165–169.

[12] Anisimkin, V. I., and E. Verona. 1998. New properties of saw gas sensing. *IEEE Transactions on Ultrasonics Ferroelectrics and Frequency Control* 45:1347–1354.

[13] Jakubik, W. P., M. W. Urbanczyk, S. Kochowski, and J. Bodzenta. 2002. Bilayer structure for hydrogen detection in a surface acoustic wave sensor system. *Sensors and Actuators B-Chemical* 82:265–271.

[14] Srinivasan, K., S. Cular, V. R. Bhethanabotla, S. Lee, M. T. Harris, and J. N. Culver. 2005. Palladium nanoparticle coated tobacco moasic virus sensing layer based surface acoustic wave hydrogen sensors. *In* Nanotechnology and Nanobiotechnology for Sensors I. The 2005 Annual AICHE Meeting, Cincinnati, OH, 74d.

[15] Butler, M. A., and D. S. Ginley. 1988. Hydrogen sensing with palladium-coated optical fibers. *Journal of Applied Physics* 64:3706–3712.

[16] Bond, G. C. 1962. Catalysis by metals. Academic Press, New York.

[17] Anderson, J. R. 1975. The structure of metallic catalysis. Academic Press, New York.

[18] Cheng, Y. T., Y. Li, D. Lisi, and W. M. Wang. 1996. Preparation and characterization of Pd/Ni thin films for hydrogen sensing. *Sensors and Actuators B-Chemical* 30:11–16.

[19] Armgarth, M., D. Soderberg, and I. Lundstrom. 1982. Palladium and platinum gate metal-oxide-semiconductor capacitors in hydrogen and oxygen mixtures. *Applied Physics Letters* 41:654–655.

[20] Lewis, F. A. 1967. The palladium hydrogen system. Academic Press, London, New York.

[21] DiMeo Jr., F., and B. Chen. 2000. Microhotplate based H_2 gas sensors. *In* Proceedings of the 2000 Hydrogen Program Review. U.S. Department of Energy, Golden, CO, Volume II.

[22] Kong, J., M. G. Chapline, and H. J. Dai. 2001. Functionalized carbon nanotubes for molecular hydrogen sensors. *Advanced Materials* 13:1384–1386.

[23] Im, Y., C. Lee, R. P. Vasquez, M. A. Bangar, N. V. Myung, E. J. Menke, R. M. Penner, and M. H. Yun. 2006. Investigation of a single Pd nanowire for use as a hydrogen sensor. *Small* 2:356–358.

[24] Iijima, S. 1991. Helical microtubules of graphitic carbon. *Nature* 354:56–58.

[25] Iijima, S., and T. Ichihashi. 1993. Single-shell carbon nanotubes of 1-nm diameter. *Nature* 364:737–737.

[26] Saito, R., M. Fujita, G. Dresselhaus, and M. S. Dresselhaus. 1992. Electronic-structure of chiral graphene tubules. *Applied Physics Letters* 60:2204–2206.

[27] Saito, R., G. Dresselhaus, and M. S. Dresselhaus. 1998. Physical properties of carbon nanotubes. Imperial College Press, London.

[28] Kong, J., N. R. Franklin, C. W. Zhou, M. G. Chapline, S. Peng, K. J. Cho, and H. J. Dai. 2000. Nanotube molecular wires as chemical sensors. *Science* 287:622–625.

[29] Collins, P. G., K. Bradley, M. Ishigami, and A. Zettl. 2000. Extreme oxygen sensitivity of electronic properties of carbon nanotubes. *Science* 287:1801–1804.

[30] Dresselhaus, M. S., G. Dresselhaus, and P. C. Eklund. 1996. Science of fullerenes and carbon nanotubes. Academic Press, San Diego.

[31] Dekker, C. 1999. Carbon nanotubes as molecular quantum wires. *Physics Today* 52:22–28.

[32] Treacy, M. M. J., T. W. Ebbesen, and J. M. Gibson. 1996. Exceptionally high Young's modulus observed for individual carbon nanotubes. *Nature* 381:678–680.

[33] Wong, E. W., P. E. Sheehan, and C. M. Lieber. 1997. Nanobeam mechanics: Elasticity, strength, and toughness of nanorods and nanotubes. *Science* 277:1971–1975.

[34] Jhi, S. H., S. G. Louie, and M. L. Cohen. 2000. Electronic properties of oxidized carbon nanotubes. *Physical Review Letters* 85:1710–1713.

[35] Peng, S., and K. J. Cho. 2000. Chemical control of nanotube electronics. *Nanotechnology* 11:57–60.

[36] Sun, C. Q., Y. Wang, B. K. Tay, S. Li, H. Huang, and Y. B. Zhang. 2002. Correlation between the melting point of a nanosolid and the cohesive energy of a surface atom. *Journal of Physical Chemistry B* 106:10701 –10705.

[37] Xie, R. H., J. Zhao, and Q. Rao. 2004. Doped carbon nanotubes. *Encyclopedia of nanoscience and nanotechnology* 2:505–535.

[38] Sayago, I., E. Terrado, E. Lafuente, M. C. Horrillo, W. K. Maser, A. M. Benito, R. Navarro, E. P. Urriolabeitia, M. T. Martinez, and J. Gutieerez. 2005. Hydrogen sensors based on carbon nanotubes thin films. *Synthetic Metals* 148:15–19.

[39] Sippel-Oakley, J., H. T. Wang, B. S. Kang, Z. C. Wu, F. Ren, A. G. Rinzler, and S. J. Pearton. 2005. Carbon nanotube films for room temperature hydrogen sensing. *Nanotechnology* 16:2218–2221.

[40] Lu, Y. J., J. Li, J. Han, H. T. Ng, C. Binder, C. Partridge, and M. Meyyappan. 2004. Room temperature methane detection using palladium loaded single-walled carbon nanotube sensors. *Chemical Physics Letters* 391:344–348.

[41] Frenkel, D., and B. Smit. 2002. Understanding molecular simulation: From algorithms to applications. 2^{nd} edition. Academic Press, San Diego.

[42] Verlet, L. 1967. Computer "experiments" on classical fluids. I. Thermodynamical properties of Lennard-Jones molecules. *Physical Review* 159:98–103.

[43] Allen, M. P., and D. J. Tildesley. 1989. Computer simulation of liquids. Oxford science publications, Clarendon Press; Oxford University Press, Oxford England; New York.

[44] Cramer, C. J. 2004. Essentials of computational chemistry: Theories and models. 2^{nd} edition. Wiley, Chichester, West Sussex, England; Hoboken, NJ.

[45] Kittel, C., and H. Kroemer. 2000. Thermal physics. 2^{nd} edition. W.H. Freeman and Co., New York.

[46] Berendsen, H. J. C., J. P. M. Postma, W. F. Vangunsteren, A. Dinola, and J. R. Haak. 1984. Molecular-dynamics with coupling to an external bath. *Journal of Chemical Physics* 81:3684–3690.

[47] Smith, W., and T. R. Forester. 1996. DL_POLY 2.0: A general-purpose parallel molecular dynamics simulation package. *Journal of Molecular Graphics* 14:136–141.

[48] Sutton, A. P., and J. Chen. 1990. Long-range Finnis Sinclair potentials. *Philosophical Magazine Letters* 61:139–146.

[49] Streett, W. B., D. J. Tildesley, and G. Saville. 1978. Multiple time-step methods in molecular-dynamics. *Molecular Physics* 35:639–648.

[50] Ercolessi, F., W. Andreoni, and E. Tosatti. 1991. Melting of small gold particles - mechanism and size effects. *Physical Review Letters* 66:911–914.

[51] Schmidt, M., R. Kusche, W. Kronmuller, B. vonIssendorff, and H. Haberland. 1997. Experimental determination of the melting point and heat capacity for a free cluster of 139 sodium atoms. *Physical Review Letters* 79:99–102.

[52] Lai, S. L., J. Y. Guo, V. Petrova, G. Ramanath, and L. H. Allen. 1996. Size-dependent melting properties of small tin particles: Nanocalorimetric measurements. *Physical Review Letters* 77:99–102.

[53] Peters, K. F., J. B. Cohen, and Y.-W. Chung. 1998. Melting of Pb nanocrystals. *Physical Review B* 57:13430–13438.

[54] Couchman, P. R. 1979. Lindemann hypothesis and the size dependence of melting temperatures. II. *Philosophical Magazine a-Physics of Condensed Matter Structure Defects and Mechanical Properties* 40:637–643.

[55] Borel, J. P. 1981. Thermodynamical size effect and the structure of metallic clusters. *Surface Science* 106:1–9.

[56] Rey, C., L. J. Gallego, J. Garciarodeja, J. A. Alonso, and M. P. Iniguez. 1993. Molecular-dynamics study of the binding-energy and melting of transition-metal clusters. *Physical Review B* 48:8253–8262.

[57] Longo, R. C., C. Rey, and L. J. Gallego. 2000. Molecular dynamics study of the melting behaviour of seven-atom clusters of fcc transition and noble metals on the (111) surface of the same metal using the embedded atom model. *Surface Science* 459:L441–L445.

[58] Li, T. X., Y. L. Ji, S. W. Yu, and G. H. Wang. 2000. Melting properties of noble metal clusters. *Solid State Communications* 116:547–550.

[59] Shimizu, Y., K. S. Ikeda, and S. Sawada. 2001. Spontaneous alloying in binary metal microclusters: A molecular dynamics study. *Physical Review B* 64:075412.

[60] Huang, S. P., and P. B. Balbuena. 2002. Melting of bimetallic Cu-Ni nanoclusters. *Journal of Physical Chemistry B* 106:7225–7236.

[61] Hansen, T. W., J. B. Wagner, P. L. Hansen, S. Dahl, H. Topsoe, and C. J. H. Jacobsen. 2001. Atomic-resolution in situ transmission electron microscopy of a promoter of a heterogeneous catalyst. *Science* 294:1508–1510.

[62] Kondo, Y., and K. Takayanagi. 2000. Synthesis and characterization of helical multi-shell gold nanowires. *Science* 289:606–608.

[63] Mikkelsen, A., N. Skold, L. Ouattara, M. Borgstrom, J. N. Andersen, L. Samuelson, W. Seifert, and E. Lundgren. 2004. Direct imaging of the atomic structure inside a nanowire by scanning tunnelling microscopy. *Nature Materials* 3:519–523.

[64] Hendriksen, B. L. M., and J. W. M. Frenken. 2002. CO oxidation on Pt(110): Scanning tunneling microscopy inside a high-pressure flow reactor. *Physical Review Letters* 89:046101.

[65] Wang, J., H. F. M. Boelens, M. B. Thathagar, and G. Rothenberg. 2004. In situ spectroscopic analysis of nanocluster formation. *Chemphyschem* 5:93–98.

[66] Helveg, S., C. Lopez-Cartes, J. Sehested, P. L. Hansen, B. S. Clausen, J. R. Rostrup-Nielsen, F. Abild-Pedersen, and J. K. Norskov. 2004. Atomic-scale imaging of carbon nanofibre growth. *Nature* 427:426–429.

[67] Chushak, Y. G., and L. S. Bartell. 2001. Melting and freezing of gold nanoclusters. *Journal of Physical Chemistry B* 105:11605–11614.

[68] Wang, L., Y. N. Zhang, X. F. Bian, and Y. Chen. 2003. Melting of cu nanoclusters by molecular dynamics simulation. *Physics Letters A* 310:197–202.

[69] Cleveland, C. L., W. D. Luedtke, and U. Landman. 1999. Melting of gold clusters. *Physical Review B* 60:5065–5077.

[70] Valkealahti, S., and M. Manninen. 1992. Instability of cuboctahedral copper clusters. *Physical Review B* 45:9459–9462.

[71] Gulseren, O., F. Ercolessi, and E. Tosatti. 1995. Premelting of thin wires. *Physical Review B* 51:7377–7380.

[72] Liu, H. B., J. A. Ascencio, M. Perez-Alvarez, and M. J. Yacaman. 2001. Melting behavior of nanometer sized gold isomers. *Surface Science* 491:88–98.

[73] Lee, Y. J., E. K. Lee, S. Kim, and R. M. Nieminen. 2001. Effect of potential energy distribution on the melting of clusters. *Physical Review Letters* 86:999–1002.

[74] Wang, B., G. Wang, X. Chen, and J. Zhao. 2002. Melting behavior of ultrathin titanium nanowires. *Physical Review B* 67:193403.

[75] Schmid, G., S. Emde, V. Maihack, W. MeyerZaika, and S. Peschel. 1996. Synthesis and catalytic properties of large ligand stabilized palladium clusters. *Journal of Molecular Catalysis a-Chemical* 107:95–104.

[76] Blaser, H. U., A. Indolese, A. Schnyder, H. Steiner, and M. Studer. 2001. Supported palladium catalysts for fine chemicals synthesis. *Journal of Molecular Catalysis a-Chemical* 173:3–18.

[77] Schmid, G., M. Baumle, M. Geerkens, I. Helm, C. Osemann, and T. Sawitowski. 1999. Current and future applications of nanoclusters. *Chemical Society Reviews* 28:179–185.

[78] Volokitin, Y., J. Sinzig, L. J. deJongh, G. Schmid, M. N. Vargaftik, and I. I. Moiseev. 1996. Quantum-size effects in the thermodynamic properties of metallic nanoparticles. *Nature* 384:621–623.

[79] Westergren, J., and S. Nordholm. 2003. Melting of palladium clusters - density of states determination by Monte Carlo simulation. *Chemical Physics* 290:189–209.

[80] Foiles, S. M., M. I. Baskes, and M. S. Daw. 1986. Embedded-atom-method functions for the fcc metals Cu, Ag, Au, Ni, Pd, Pt, and their alloys. *Physical Review B* 33:7983–7991.

[81] Ercolessi, F., E. Tosatti, and M. Parrinello. 1986. Au (100) surface reconstruction. *Physical Review Letters* 57:719–722.

[82] Tomanek, D., A. A. Aligia, and C. A. Balseiro. 1985. Calculation of elastic strain and electronic effects on surface segregation. *Physical Review B* 32:5051–5056.

[83] Uppenbrink, J., and D. J. Wales. 1993. Structure and dynamics of model metal-clusters. *Journal of Chemical Physics* 98:5720–5733.

[84] Wales, D. J., and L. J. Munro. 1996. Changes of morphology and capping of model transition metal clusters. *Journal of Physical Chemistry* 100:2053–2061.

[85] Lloyd, L. D., and R. L. Johnston. 2000. Theoretical analysis of 17-19-atom metal clusters using many-body potentials. *Journal of the Chemical Society-Dalton Transactions* :307–316.

[86] Nieminen, J. A. 1995. Temperature-dependence of surface reconstructions of Au on Pd(110). *Physical Review Letters* 74:3856–3859.

[87] Kaszkur, Z. A., and B. Mierzwa. 1998. Segregation in model palladium-cobalt clusters. *Philosophical Magazine a-Physics of Condensed Matter Structure Defects and Mechanical Properties* 77:781–800.

[88] Lamas, E. J., and P. B. Balbuena. 2003. Adsorbate effects on structure and shape of supported nanoclusters: A molecular dynamics study. *Journal of Physical Chemistry B* 107:11682–11689.

[89] Allen, M. P., and D. J. Tildesley. 1989. Computer simulation of liquids. Clarendon Press; Oxford University Press, Oxford; New York.

[90] Glatter, O., and O. Kratky. 1982. Small angle X-ray scattering. Academic Press, London; New York.

[91] Miller, M. K. 2000. Atom probe tomography: Analysis at the atomic level. Kluwer Academic / Plenum Publishers, New York.

[92] Reiss, H., P. Mirabel, and R. L. Whetten. 1988. Capillarity theory for the coexistence of liquid and solid clusters. *Journal of Physical Chemistry* 92:7241–7246.

[93] Rethfeld, B., K. Sokolowski-Tinten, and D. von der Linde. 2002. Ultrafast thermal melting of laser-excited solids by homogeneous nucleation. *Physical Review B* 65:092103.

[94] Kofman, R., P. Cheyssac, A. Aouaj, Y. Lereah, G. Deutscher, T. Bendavid, J. M. Penisson, and A. Bourret. 1994. Surface melting enhanced by curvature effects. *Surface Science* 303:231–246.

[95] Chushak, Y. G., and L. S. Bartell. 2003. Freezing of Ni-Al bimetallic nanoclusters in computer simulations. *Journal of Physical Chemistry B* 107:3747–3751.

[96] Qi, Y., T. Cagin, W. L. Johnson, and W. A. Goddard. 2001. Melting and crystallization in Ni nanoclusters: The mesoscale regime. *Journal of Chemical Physics* 115:385–394.

[97] Calvo, F., and F. Spiegelmann. 2003. Mechanisms of phase transitions in sodium clusters: From molecular to bulk behavior. *Journal of Chemical Physics* 112:2888–2908.

[98] Vanselow, R., and R. Howe. 1988. Chemistry and physics of solid surfaces VII. Springer-Verlag, Berlin; New York.

[99] Iida, T., and R. I. L. Guthrie. 1988. The physical properties of liquid metals. Clarendon, Oxford.

[100] Echt, O., K. Sattler, and E. Recknagel. 1981. Magic numbers for sphere packings - experimental-verification in free xenon clusters. *Physical Review Letters* 47:1121–1124.

[101] Steinhardt, P. J., D. R. Nelson, and M. Ronchetti. 1983. Bond-orientational order in liquids and glasses. *Physical Review B* 28:784–805.

[102] Sakurai, J. J., and S. F. Tuan. 1994. Modern quantum mechanics. Rev. edition. Addison-Wesley Pub. Co., Reading, Mass.

[103] Wang, Y. T., and C. Dellago. 2003. Structural and morphological transitions in gold nanorods: A computer simulation study. *Journal of Physical Chemistry B* 107:9214–9219.

[104] Jose-Yacaman, M., R. Herrera, A. Gomez, and S. Tehuacanero. 1990. Decagonal and hexagonal structures in small gold particles. *Surface Science* 237:248–256.

[105] Hendy, S. C., and B. D. Hall. 2001. Molecular-dynamics simulations of lead clusters. *Physical Review B* 64:085425.

[106] Buffat, P., and J. P. Borel. 1976. Size effect on melting temperature of gold particles. *Physical Review A* 13:2287–2298.

[107] Castro, T., R. Reifenberger, E. Choi, and R. P. Andres. 1990. Size-dependent melting temperature of individual nanometer-sized metallic clusters. *Physical Review B* 42:8548–8556.

[108] Dash, J. G. 1999. History of the search for continuous melting. *Reviews of Modern Physics* 71:17371743.

[109] Pawlow, P. 1909. Melting point dependence on the surface energy of a solid body. *Zeitschrift fuer Physikalische Chemie* 65:1–35.

[110] Pawlow, P. 1909. Melting point dependence on the surface energy of a solid body. *Zeitschrift fuer Physikalische Chemie* 65:545–548.

[111] Wronski, C. R. M. 1967. The size dependence of the melting point of small particles of tin. *British Journal of Applied Physics* 18:1731–1737.

[112] Vanfleet, R. R., and J. M. Mochel. 1995. Thermodynamics of melting and freezing in small particles. *Surface Science* 341:40–50.

[113] Sakai, H. 1996. Surface-induced melting of small particles. *Surface Science* 351:285–291.

[114] Wautelet, M. 1991. Estimation of the variation of the melting temperature with the size of small particles, on the basis of a surface-phonon instability model. *Journal of Physics D-Applied Physics* 24:343–346.

[115] Nanda, K. K., S. N. Sahu, and S. N. Behera. 2002. Liquid-drop model for the size-dependent melting of low-dimensional systems. *Physical Review A* 66:013208.

[116] Miao, L., V. R. Bhethanabotla, and B. Joseph. 2005. Melting of Pd clusters and nanowires: A comparison study using molecular dynamics simulation. *Physical Review B* 72:134109.

[117] Schmidt, M., R. Kusche, B. von Issendorff, and H. Haberland. 1998. Irregular variations in the melting point of size-selected atomic clusters. *Nature* 393:238–240.

[118] Savoia, D., C. Trombini, A. Umanironchi, and G. Verardo. 1981. Active metals from potassium-graphite - palladium-graphite as catalyst in the hydrogenation of nitro-compounds, alkenes, and alkynes. *Journal of the Chemical Society-Chemical Communications* :540–541.

[119] Farkas, G., L. Hegedus, A. Tungler, T. Mathe, J. L. Figueiredo, and M. Freitas. 2000. Effect of carbon support properties on enantioselective hydrogenation of isophorone over palladium catalysts modified with (-)-dihydroapovincaminic acid ethyl ester. *Journal of Molecular Catalysis a-Chemical* 153:215–219.

[120] Bazin, D. 2002. Solid state concepts to understand catalysis using nanoscale metallic particles. *Topics in Catalysis* 18:79–84.

[121] Huang, S. P., D. S. Mainardi, and P. B. Balbuena. 2003. Structure and dynamics of graphite-supported bimetallic nanoclusters. *Surface Science* 545:163–179.

[122] Bardotti, L., P. Jensen, A. Hoareau, M. Treilleux, and B. Cabaud. 1995. Experimental observation of fast diffusion of large antimony clusters on graphite surfaces. *Physical Review Letters* 74:4694–4697.

[123] Tomanek, D., and W. Zhong. 1991. Palladium-graphite interaction potentials based on 1st-principles calculations. *Physical Review B* 43:12623–12625.

[124] Bhethanabotla, V. R., and W. A. Steele. 1990. Computer-simulation study of melting in dense oxygen layers on graphite. *Physical Review B* 41:9480–9487.

[125] Agrawal, P. M., B. M. Rice, and D. L. Thompson. 2002. Predicting trends in rate parameters for self-diffusion on fcc metal surfaces. *Surface Science* 515:21–35.

[126] Ko, E., M. Jain, and J. R. Chelikowsky. 2002. First principles simulations of sige for the liquid and amorphous states. *Journal of Chemical Physics* 117:3476–3483.

[127] Hohenberg, P., and W. Kohn. 1964. Inhomogeneous electron gas. *Physical Review* 136:B864–71.

[128] Kohn, W., and L. J. Sham. 1965. Self-consistent equations including exchange and correlation effects. *Physical Review* 140:A1133–38.

[129] Wigner, E. 1938. The transition-state method. *Transactions of the Faraday Society* 34:29–41.

[130] Ceperley, D. 1978. Ground-state of the fermion one-component plasma - Monte-Carlo study in 2 and 3 dimensions. *Physical Review B* 18:3126–3138.

[131] Ceperley, D. M., and B. J. Alder. 1980. Ground-state of the electron-gas by a stochastic method. *Physical Review Letters* 45:566–569.

[132] Becke, A. D. 1988. Density-functional exchange-energy approximation with correct asymptotic-behavior. *Physical Review A* 38:3098–3100.

[133] Becke, A. D. 1986. Density functional calculations of molecular-bond energies. *Journal of Chemical Physics* 84:4524–4529.

[134] Perdew, J. P. 1986. Density-functional approximation for the correlation-energy of the inhomogeneous electron-gas. *Physical Review B* 33:8822–8824.

[135] Wang, Y., and J. P. Perdew. 1991. Correlation hole of the spin-polarized electron-gas, with exact small-wave-vector and high-density scaling. *Physical Review B* 44:13298–13307.

[136] Perdew, J. P., J. A. Chevary, S. H. Vosko, K. A. Jackson, M. R. Pederson, D. J. Singh, and C. Fiolhais. 1992. Atoms, molecules, solids, and surfaces - applications of the generalized gradient approximation for exchange and correlation. *Physical Review B* 46:6671–6687.

[137] Perdew, J. P., K. Burke, and M. Ernzerhof. 1996. Generalized gradient approximation made simple. *Physical Review Letters* 77:3865–3868.

[138] Lee, C. T., W. T. Yang, and R. G. Parr. 1988. Development of the Colle-Salvetti correlation-energy formula into a functional of the electron-density. *Physical Review B* 37:785–789.

[139] Becke, A. D. 1996. Density-functional thermochemistry. 4. A new dynamical correlation functional and implications for exact-exchange mixing. *Journal of Chemical Physics* 104:1040–1046.

[140] Kohn, W. 1999. An essay on condensed matter physics in the twentieth century. *Reviews of Modern Physics* 71:S59–S77.

[141] SanchezPortal, D., E. Artacho, and J. M. Soler. 1996. Analysis of atomic orbital basis sets from the projection of plane-wave results. *Journal of Physics-Condensed Matter* 8:3859–3880.

[142] Ashcroft, N. W., and N. D. Mermin. 1964. Solid state physics. Holt Rinehart and Winston, New York.

[143] Phillips, J. C. 1958. Energy-band interpolation scheme based on a pseudopotential. *Physical Review* 1:685–695.

[144] Yin, M. T., and M. L. Cohen. 1982. Theory of $ab\ initio$ pseudopotential calculations. *Physical Review B* 25:7403–7412.

[145] Yin, M. T., and M. L. Cohen. 1982. Theory of static structural-properties, crystal stability, and phase-transformations - application to Si and Ge. *Physical Review B* 26:5668–5687.

[146] Kleinman, L., and D. M. Bylander. 1982. Efficacious form for model pseudopotentials. *Physical Review Letters* 48:1425–1428.

[147] Vanderbilt, D. 1990. Soft self-consistent pseudopotentials in a generalized eigenvalue formalism. *Physical Review B* 41:7892–7895.

[148] Kresse, G., and J. Hafner. 1993. $Ab\ initio$ molecular-dynamics for liquid-metals. *Physical Review B* 47:558–561.

[149] Kresse, G., and J. Hafner. 1994. $Ab\ initio$ molecular-dynamics simulation of the liquid-metal amorphous-semiconductor transition in germanium. *Physical Review B* 49:14251.

[150] Kresse, G., and J. Furthmuller. 1996. Efficiency of ab-$initio$ total energy calculations for metals and semiconductors using a plane-wave basis set. *Computational Materials Science* 6:15–50.

[151] Kresse, G., and J. Furthmuller. 1996. Efficient iterative schemes for $ab\ initio$ total-energy calculations using a plane-wave basis set. *Physical Review B* 54:11169–11186.

[152] Ciraci, S., S. Dag, T. Yildirim, O. Gulseren, and R. T. Senger. 2004. Functionalized carbon nanotubes and device applications. *Journal of Physics-Condensed Matter* 16:R901–R960.

[153] Durgun, E., S. Dag, V. M. K. Bagci, O. Gulseren, T. Yildirim, and S. Ciraci. 2003. Systematic study of adsorption of single atoms on a carbon nanotube. *Physical Review B* 67:201401.

[154] Durgun, E., S. Dag, S. Ciraci, and O. Gulseren. 2004. Energetics and electronic structures of individual atoms adsorbed on carbon nanotubes. *Journal of Physical Chemistry B* 108:575–582.

[155] Yang, C. K., J. J. Zhao, and J. P. Lu. 2002. Binding energies and electronic structures of adsorbed titanium chains on carbon nanotubes. *Physical Review B* 66:041403.

[156] Bagci, V. M. K., O. Gulseren, T. Yildirim, Z. Gedik, and S. Ciraci. 2002. Metal nanoring and tube formation on carbon nanotubes. *Physical Review B* 66:045409.

[157] Singh, D. J. 1994. Planewaves, pseudopotentials, and the LAPW method. Kluwer Academic Publishers, Boston.

[158] Payne, M. C., M. P. Teter, D. C. Allan, T. A. Arias, and J. D. Joannopoulos. 1992. Iterative minimization techniques for $ab\ initio$ total-energy calculations - molecular-dynamics and conjugate gradients. *Reviews of Modern Physics* 64:1045–1097.

[159] Lee, E. C., Y. S. Kim, Y. G. Jin, and K. J. Chang. 2002. First-principles study of hydrogen adsorption on carbon nanotube surfaces. *Physical Review B* 66:073415.

[160] Peng, S., and K. J. Cho. 2003. $Ab\ initio$ study of doped carbon nanotube sensors. *Nano Letters* 3:513–517.

[161] Dag, S., Y. Ozturk, S. Ciraci, and T. Yildirim. 2005. Adsorption and dissociation of hydrogen molecules on bare and functionalized carbon nanotubes. *Physical Review B* 72:155404.

[162] Jakubik, W. P., M. W. Urbanczyk, S. Kochowski, and J. Bodzenta. 2003. Palladium and phthalocyanine bilayer films for hydrogen detection in a surface acoustic wave sensor system. *Sensors and Actuators B-Chemical* 96:321–328.

[163] Smit, R. H. M., C. Untiedt, A. I. Yanson, and J. M. van Ruitenbeek. 2001. Common origin for surface reconstruction and the formation of chains of metal atoms. *Physical Review Letters* 87:266102.

[164] Ohnishi, H., Y. Kondo, and K. Takayanagi. 1998. Quantized conductance through individual rows of suspended gold atoms. *Nature* 395:780–783.

[165] Yanson, A. I., G. R. Bollinger, H. E. van den Brom, N. Agrait, and J. M. van Ruitenbeek. 1998. Formation and manipulation of a metallic wire of single gold atoms. *Nature* 395:783–785.

[166] Sen, P., S. Ciraci, A. Buldum, and I. P. Batra. 2001. Structure of aluminum atomic chains. *Physical Review B* 64:195420.

[167] Sanchez-Portal, D., E. Artacho, J. Junquera, P. Ordejon, A. Garcia, and J. M. Soler. 1999. Stiff monatomic gold wires with a spinning zigzag geometry. *Physical Review Letters* 83:3884–3887.

[168] Bahn, S. R., and K. W. Jacobsen. 2001. Chain formation of metal atoms. *Physical Review Letters* 87:266101.

[169] Geng, W. T., and K. S. Kim. 2003. Linear monatomic wires stabilized by alloying: $Ab\ initio$ density functional calculations. *Physical Review B* 67:233403.

[170] Nilius, N., T. M. Wallis, and W. Ho. 2004. Building alloys from single atoms: Au-Pd chains on NiAl(110). *Journal of Physical Chemistry B* 108:14616–14619.

[171] Zhang, Y., N. W. Franklin, R. J. Chen, and H. J. Dai. 2000. Metal coating on suspended carbon nanotubes and its implication to metal-tube interaction. *Chemical Physics Letters* 331:35–41.

[172] Marinas, J. M., J. M. Campelo, and D. Luna. 1986. New supported metallic nickel systems. *Studies in Surface Science and Catalysis* 27:411–457.

[173] Hughes, R. C., W. T. Schubert, and R. J. Buss. 1995. Solid-state hydrogen sensors using palladium-nickel alloys - effect of alloy composition on sensor response. *Journal of the Electrochemical Society* 142:249–254.

[174] Thomas, R. C., and R. C. Hughes. 1997. Sensors for detecting molecular hydrogen based on Pd metal alloys. *Journal of the Electrochemical Society* 144:3245–3249.

[175] Raybaud, P., G. Kresse, J. Hafner, and H. Toulhoat. 1997. $Ab\ initio$ density functional studies of transition-metal sulphides: I. Crystal structure and cohesive properties. *Journal of Physics-Condensed Matter* 9:11085–11106.

[176] Monkhorst, H. J., and J. D. Pack. 1976. Special points for Brillouin-zone integrations. *Physical Review B* 13:5188–5192.

[177] Yagi, Y., T. M. Briere, M. H. F. Sluiter, V. Kumar, A. A. Farajian, and Y. Kawazoe. 2004. Stable geometries and magnetic properties of single-walled carbon nanotubes doped with 3d transition metals: A first-principles study. *Physical Review B* 69:075414.

[178] Peierls, R. E. 1964. Quantum theory of solids. Clarendon Press, Oxford.

[179] Weinert, M., E. Wimmer, and A. J. Freeman. 1982. Total-energy all-electron density functional method for bulk solids and surfaces. *Physical Review B* 26:4571–4578.

[180] Blaha, P., K. Schwarz, G. Madsen, D. Kvasnicka, and J. Luitz. 2001. WIEN2k: An Augemented Plane Wave Plus Local Orbital Program for Calculating Crystal Properties. Vienna University of Technology, Vienna, Austria.

[181] Miao, L., V. R. Bhethanabotla, and B. Joseph. in progress 2006 .

[182] Reich, S., C. Thomsen, and P. Ordejon. 2002. Electronic band structure of isolated and bundled carbon nanotubes. *Physical Review B* 65:155411.

[183] Gulseren, O., T. Yildirim, and S. Ciraci. 2002. Systematic $ab\ initio$ study of curvature effects in carbon nanotubes. *Physical Review B* 65:153405.

[184] Henkelman, G., A. Arnaldsson, and H. Jonsson. 2006. A fast and robust algorithm for bader decomposition of charge density. *Computatioinal Materials Science* 36:254–360.

[185] Zhao, J. J., A. Buldum, J. Han, and J. P. Lu. 2002. Gas molecule adsorption in carbon nanotubes and nanotube bundles. *Nanotechnology* 13:195–200.

[186] Tada, K., S. Furuya, and K. Watanabe. 2001. $Ab\ initio$ study of hydrogen adsorption to single-walled carbon nanotubes. *Physical Review B* 63:155405.

[187] Dillon, A. C., K. M. Jones, T. A. Bekkedahl, C. H. Kiang, D. S. Bethune, and M. J. Heben. 1997. Storage of hydrogen in single-walled carbon nanotubes. *Nature* 386:377–379.

[188] Ahn, C. C., Y. Ye, B. V. Ratnakumar, C. Witham, R. C. Bowman, and B. Fultz. 1998. Hydrogen desorption and adsorption measurements on graphite nanofibers. *Applied Physics Letters* 73:3378–3380.

[189] Modi, A., N. Koratkar, E. Lass, B. Q. Wei, and P. M. Ajayan. 2003. Miniaturized gas ionization sensors using carbon nanotubes. *Nature* 424:171–174.

[190] Han, S. S., and H. M. Lee. 2004. Adsorption properties of hydrogen on (10,0) single-walled carbon nanotube through density functional theory. *Carbon* 42:2169–2177.

[191] Balasubramanian, K., P. Y. Feng, and M. Z. Liao. 1988. Electronic states and potential energy surfaces of PdH_2: Comparison with PtH_2. *Journal of Chemical Physics* 88:6955–6961.

[192] Conrad, H., G. Ertl, and E. E. Latta. 1974. Adsorption of hydrogen on palladium single crystal surfaces. *surface science* 41:435–446.

[193] Wilke, S., D. Hennig, and R. Lober. 1994. *Ab-initio* calculations of hydrogen adsorption on (100) surfaces of palladium and rhodium. *Physical Review B* 50:2548–2560.

[194] Behm, R. J., K. Christmann, and G. Ertl. 1980. Adsorption of hydrogen on Pd(100). *Surface Science* 99:320–340.

[195] Nowick, A. S., and J. J. Burton. 1975. Diffusion in solids. Academic Press, New York.

[196] Christmann, K., O. Schober, G. Ertl, and M. Neumann. 1973. Adsorption of hydrogen on nickel single crystal surfaces. *The journal of chemical physics* 60:4528–4540.

[197] Madix, R. J., G. Ertl, and K. Christmann. 1979. Pre-exponential factors for hydrogen desorption from single-crystal metal-surfaces. *Chemical Physics Letters* 62:38–41.

[198] Landolt, M., and M. Campagna. 1977. Demagnetization of Ni(100) surface by hydrogen adsorption. *Physical Review Letters* 39:568–570.

[199] Muscat, J. P., and D. M. Newns. 1979. Nature of the bond in hydrogen chemisorption on ni, pd, and pt. *Physical Review Letters* 43:2025–2028.

[200] Wong, Y. M., W. P. Kang, J. L. Davidson, A. Wisitsora-at, and K. L. Soh. 2003. A novel microelectronic gas sensor utilizing carbon nanotubes for hydrogen gas detection. *Sensors and Actuators B-Chemical* 93:327–332.

[201] Star, A., T. R. Han, V. Joshi, J. C. P. Gabriel, and G. Gruner. 2004. Nanoelectronic carbon dioxide sensors. *Advanced Materials* 16:2049–2052.

[202] Liang, Y. X., Y. J. Chen, and T. H. Wang. 2004. Low-resistance gas sensors fabricated from multiwalled carbon nanotubes coated with a thin tin oxide layer. *Applied Physics Letters* 85:666–668.

[203] Bekyarova, E., M. Davis, T. Burch, M. E. Itkis, B. Zhao, S. Sunshine, and R. C. Haddon. 2004. Chemically functionalized single-walled carbon nanotubes as ammonia sensors. *Journal of Physical Chemistry B* 108:19717–19720.

[204] Durgun, E., S. Dag, and S. Ciraci. 2004. Theoretical study of Ga-based nanowires and the interaction of Ga with single-wall carbon nanotubes. *Physical Review B* 70:155305.

[205] Dag, S., E. Durgun, and S. Ciraci. 2004. High-conducting magnetic nanowires obtained from uniform titanium-covered carbon nanotubes. *Physical Review B* 69:121407.

[206] Peng, S., and K. Cho. 2002. Nano electro mechanics of semiconducting carbon nanotube. *Journal of Applied Mechanics-Transactions of the Asme* 69:451–453.

[207] Sampedro, B., P. Crespo, A. Hernando, R. Litran, J. C. S. Lopez, C. L. Cartes, A. Fernandez, J. Ramirez, J. G. Calbet, and M. Vallet. 2003. Ferromagnetism in fcc twinned 2.4 nm size Pd nanoparticles. *Physical Review Letters* 91:237203.

[208] Alefeld, G., and J. Vlkl. 1978. Hydrogen in metals. Topics in applied physics; v. 28-29, Springer-Verlag, Berlin; New York.

[209] Schlapbach, L., and J. P. Burger. 1982. A new XPS UPS study of the electronic-structure of PdH0.6. *Journal De Physique Lettres* 43:L273–L276.

[210] Bennett, P. A., and J. C. Fuggle. 1982. Electronic-structure and surface kinetics of palladium hydride studied with X-ray photoelectron-spectroscopy and electron-energy-loss spectroscopy. *Physical Review B* 26:6030–6039.

[211] Chan, C. T., and S. G. Louie. 1983. Self-consistent pseudopotential calculation of the electronic-structure of PdH and Pd_4H. *Physical Review B* 27:3325–3337.

[212] Imry, Y., and R. Landauer. 1999. Conductance viewed as transmission. *Reviews of Modern Physics* 71:S306–S312.

[213] Car, R., and M. Parrinello. 1985. Unified approach for molecular-dynamics and density-functional theory. *Physical Review Letters* 55:2471–2474.

[214] Iftimie, R., P. Minary, and M. E. Tuckerman. 2005. $Ab\ initio$ molecular dynamics: Concepts, recent developments, and future trends. *Proceedings of the National Academy of Sciences of the United States of America* 102:6654–6659.

Appendices

Appendix A: DL_POLY Programs

DL_POLY_2 requires five input files named CONTROL, CONFIG, FIELD, TABLE and REVOLD. The first three files are mandatory, while TABLE is used only to input certain kinds of pair potential, and is not always required. REVOLD is required only if the job represents a continuation of a previous job. In the following sections I describe the form and content of these files used in the Pd nanocluster simulations.

A.1 The Input Files

A.1.1 The CONTROL File

CONTROL file defines the control variables for running a DL_POLY_2 job. The CONTROL file is small and easy to check visually. An example CONTROL file for a fcc Pd nanocluster appears below.

```
DL_POLY CONTROL FILE: Pd nanocluster
temperature          300.00
pressure             0.0000
ensemble nvt ber     0.4
integrator           leapfrog
steps                600000
equilibration        400000
scale                10
print                100
stack                10
stats                10
rdf                  10
timestep             0.001
cutoff               6.878
delr width           1.000
no electrostatics
zden
traj                 400000 100 1
print rdf
```

Appendix A (Continued)

```
job time            100000.00
close time          500.00
finish
```

The meaning of directives listed this CONTROL file are as follows:

- DL_POLY CONTROL FILE: This line is a header to aid identification of the file. This line is limited to 80 characters.
- temperature: Set the required simulation temperature to 300 K
- pressure: Set the required simulation pressure to 0 katm
- ensemble nvt ber: Set NVT ensemble with the Berendsen thermostat with coupling time constant 0.4
- integrator: Select leapfrog integration algorithm
- steps: Run simulation for 600,000 timesteps
- equilibration: Equilibrate simulation for first 400,000 timesteps
- scale: Rescale atomic velocities every 10 timesteps during equilibration
- print: Print system data every 100 timesteps
- stack: Set rolling average stack to 10 timesteps
- stats: Accumulate statistics data every 10 timesteps
- rdf: Calculate radial distribution functions at every 10 timesteps
- timestep: Set simulation timestep to 0.001 ps

- cutoff: Set required forces cutoff to 6.8778 Å
- delr width: Set Verlet neighbor list shell width to 0.55 Å
- zden: Calculate the z-density profile
- traj: Write coordinates and velocities outputs into HISTORY file starting from the indicated timestep (400,000) at interval of 100 timesteps
- print rdf: Print radial distribution function
- job time: Set total time allowed for this job to 100,000 ps
- close time: Set the time DL_POLY requires to write and close data files to 500 s
- finish: Close the CONTROL file

A.1.2 The CONFIG File

The CONFIG file contains the dimensions of the unit cell, the key for periodic boundary conditions and the atomic labels, coordinates, velocities and forces. The initial CONFIG file of the simulated Pd nanocluster is genernated by the FORTRAN program. Both the program and CONFIG file are shown below.

```
C      THIS PROGRAM GENERATE A SPHERICAL Pd CLUSTER WITH A
C      CUTOFF RADIUS OF Rc
C      N -- TOTAL NUMBER OF PD ATOMS
C      NC -- NUMBER OF UNIT CELLS

       INTEGER     N, NC
       PARAMETER ( NC = 11, N = 4 * NC   3 )
       REAL        RX(N), RY(N), RZ(N)
       REAL        CELL1, CELL2
```

Appendix A (Continued)

```
        REAL        Rc, Ra, Rsum
        NO=6
        OPEN (NO,FILE='OUTPUT')

C    CALCULATE THE SIDE OF THE UNIT CELL

        CELL  = 3.8907
        CELL2 = 0.75 * CELL
        CELL1 = 0.25 * CELL

C    SUBLATTICE A

        RX(1) =  CELL1
        RY(1) =  CELL1
        RZ(1) =  CELL1

C    SUBLATTICE B

        RX(2) =  CELL2
        RY(2) =  CELL2
        RZ(2) =  CELL1

C      SUBLATTICE C

        RX(3) =  CELL1
        RY(3) =  CELL2
        RZ(3) =  CELL2

C      SUBLATTICE D

        RX(4) =  CELL2
        RY(4) =  CELL1
        RZ(4) =  CELL2

C      CONSTRUCT THE LATTICE FROM THE UNIT CELL
```

```
        M = 0
        DO 99 IZ = 1, NC
           DO 98 IY = 1, NC
              DO 97 IX = 1, NC
                 DO 96 IREF = 1, 4
                    RX(IREF+M) = RX(IREF) + CELL * REAL ( IX - 1 )
                    RY(IREF+M) = RY(IREF) + CELL * REAL ( IY - 1 )
                    RZ(IREF+M) = RZ(IREF) + CELL * REAL ( IZ - 1 )
96               CONTINUE
                 M = M + 4
97            CONTINUE
98         CONTINUE
99      CONTINUE

C      SHIFT CENTRE OF BOX TO THE ORIGIN

        S=0
        R=0
        Rsum=0
        DO 100 I = 1, N
        RX(I) = RX(I) - 0.5*CELL*REAL(NC)
         RY(I) = RY(I) - 0.5*CELL*REAL(NC)
         RZ(I) = RZ(I) - 0.5*CELL*REAL(NC)
100  CONTINUE
        Rc=13.2
        Do 120 J=1, N
         Ra=SQRT(RX(J) 2+RY(J) 2+RZ(J) 2)
           IF (Ra .lt. Rc)  THEN
          S=S+1
          R=R+(RX(J) 2+RY(J) 2+RZ(J) 2)
             PRINT *,'Pd','            ',S,'       ','46'
             WRITE (6,110) RX(J),RY(J),RZ(J)
             Rsum=Rsum+(RX(J) 2+RY(J) 2+RZ(J) 2)
110   FORMAT (1x,F19.15,1X,F19.15,1X,F19.15)
           ENDIF
```

```
120   CONTINUE

        END

DL_POLY CONFIG file: Pd nanocluster
         0         0
 Pd              1       46
  -2.918099880218506  -4.863500118255615  -8.754300117492676
 Pd              2       46
  -0.972700595855713  -6.808899879455566  -8.754300117492676
 Pd              3       46
   0.972699642181396  -4.863500118255615  -8.754300117492676
 Pd              4       46
   2.918099880218506  -6.808899879455566  -8.754300117492676
 Pd              5       46
   4.863500118255615  -4.863500118255615  -8.754300117492676
 Pd              6       46
  -6.808899879455566  -0.972700595855713  -8.754300117492676
 Pd              7       46
  -4.863500118255615  -2.918099880218506  -8.754300117492676
 Pd              8       46
  -2.918099880218506  -2.918099880218506 -10.699700355529785
 Pd              9       46
  -0.972700595855713  -0.972700595855713 -10.699700355529785
 Pd              10       46
  -2.918099880218506  -0.972700595855713  -8.754300117492676
 Pd              11       46
  -0.972700595855713  -2.918099880218506  -8.754300117492676
 Pd              12       46
   0.972699642181396  -2.918099880218506 -10.699700355529785
 Pd              13       46
   2.918099880218506  -0.972700595855713 -10.699700355529785
 Pd              14       46
   0.972699642181396  -0.972700595855713  -8.754300117492676
 Pd              15       46
   2.918099880218506  -2.918099880218506  -8.754300117492676
 Pd              16       46
```

```
  4.863500118255615  -0.972700595855713  -8.754300117492676
Pd             17       46
  6.808900356292725  -2.918099880218506  -8.754300117492676
Pd             18       46
 -6.808899879455566   2.918099880218506  -8.754300117492676
Pd             19       46
 -4.863500118255615   0.972699642181396  -8.754300117492676
Pd             20       46
 -2.918099880218506   0.972699642181396 -10.699700355529785
Pd             21       46
 -0.972700595855713   2.918099880218506 -10.699700355529785
Pd             22       46
 -2.918099880218506   2.918099880218506  -8.754300117492676
Pd             23       46
 -0.972700595855713   0.972699642181396  -8.754300117492676
Pd             24       46
  0.972699642181396   0.972699642181396 -10.699700355529785
Pd             25       46
  2.918099880218506   2.918099880218506 -10.699700355529785
Pd             26       46
  0.972699642181396   2.918099880218506  -8.754300117492676
Pd             27       46
  2.918099880218506   0.972699642181396  -8.754300117492676
Pd             28       46
  4.863500118255615   2.918099880218506  -8.754300117492676
Pd             29       46
  6.808900356292725   0.972699642181396  -8.754300117492676
Pd             30       46
 -4.863500118255615   4.863500118255615  -8.754300117492676
Pd             31       46
 -2.918099880218506   6.808900356292725  -8.754300117492676
Pd             32       46
 -0.972700595855713   4.863500118255615  -8.754300117492676
Pd             33       46
  0.972699642181396   6.808900356292725  -8.754300117492676
Pd             34       46
```

```
  2.918099880218506   4.863500118255615  -8.754300117492676
Pd              35       46
 -0.972700595855713  -8.754300117492676  -6.808899879455566
Pd              36       46
 -2.918099880218506  -8.754300117492676  -4.863500118255615
Pd              37       46
  2.918099880218506  -8.754300117492676  -6.808899879455566
Pd              38       46
  0.972699642181396  -8.754300117492676  -4.863500118255615
Pd              39       46
  4.863500118255615  -8.754300117492676  -4.863500118255615
Pd              40       46
 -4.863500118255615  -4.863500118255615  -6.808899879455566
Pd              41       46
 -6.808899879455566  -4.863500118255615  -4.863500118255615
Pd              42       46
 -4.863500118255615  -6.808899879455566  -4.863500118255615
Pd              43       46
 -2.918099880218506  -6.808899879455566  -6.808899879455566
Pd              44       46
 -0.972700595855713  -4.863500118255615  -6.808899879455566
Pd              45       46
 -2.918099880218506  -4.863500118255615  -4.863500118255615
Pd              46       46
 -0.972700595855713  -6.808899879455566  -4.863500118255615
Pd              47       46
  0.972699642181396  -6.808899879455566  -6.808899879455566
Pd              48       46
  2.918099880218506  -4.863500118255615  -6.808899879455566
Pd              49       46
  0.972699642181396  -4.863500118255615  -4.863500118255615
Pd              50       46
  2.918099880218506  -6.808899879455566  -4.863500118255615
Pd              51       46
  4.863500118255615  -6.808899879455566  -6.808899879455566
Pd              52       46
```

```
  6.808900356292725  -4.863500118255615  -6.808899879455566
Pd             53       46
  4.863500118255615  -4.863500118255615  -4.863500118255615
Pd             54       46
  6.808900356292725  -6.808899879455566  -4.863500118255615
Pd             55       46
  8.754301071166992  -4.863500118255615  -4.863500118255615
Pd             56       46
 -8.754300117492676  -0.972700595855713  -6.808899879455566
Pd             57       46
 -8.754300117492676  -2.918099880218506  -4.863500118255615
Pd             58       46
 -6.808899879455566  -2.918099880218506  -6.808899879455566
Pd             59       46
 -4.863500118255615  -0.972700595855713  -6.808899879455566
Pd             60       46
 -6.808899879455566  -0.972700595855713  -4.863500118255615
Pd             61       46
 -4.863500118255615  -2.918099880218506  -4.863500118255615
Pd             62       46
 -2.918099880218506  -2.918099880218506  -6.808899879455566
Pd             63       46
 -0.972700595855713  -0.972700595855713  -6.808899879455566
Pd             64       46
 -2.918099880218506  -0.972700595855713  -4.863500118255615
Pd             65       46
 -0.972700595855713  -2.918099880218506  -4.863500118255615
Pd             66       46
  0.972699642181396  -2.918099880218506  -6.808899879455566
Pd             67       46
  2.918099880218506  -0.972700595855713  -6.808899879455566
Pd             68       46
  0.972699642181396  -0.972700595855713  -4.863500118255615
Pd             69       46
  2.918099880218506  -2.918099880218506  -4.863500118255615
Pd             70       46
```

```
  4.863500118255615  -2.918099880218506  -6.808899879455566
Pd              71       46
  6.808900356292725  -0.972700595855713  -6.808899879455566
Pd              72       46
  4.863500118255615  -0.972700595855713  -4.863500118255615
Pd              73       46
  6.808900356292725  -2.918099880218506  -4.863500118255615
Pd              74       46
  8.754301071166992  -2.918099880218506  -6.808899879455566
Pd              75       46
  8.754301071166992  -0.972700595855713  -4.863500118255615
Pd              76       46
 -8.754300117492676   2.918099880218506  -6.808899879455566
Pd              77       46
 -8.754300117492676   0.972699642181396  -4.863500118255615
Pd              78       46
 -6.808899879455566   0.972699642181396  -6.808899879455566
Pd              79       46
 -4.863500118255615   2.918099880218506  -6.808899879455566
Pd              80       46
 -6.808899879455566   2.918099880218506  -4.863500118255615
Pd              81       46
 -4.863500118255615   0.972699642181396  -4.863500118255615
Pd              82       46
 -2.918099880218506   0.972699642181396  -6.808899879455566
Pd              83       46
 -0.972700595855713   2.918099880218506  -6.808899879455566
Pd              84       46
 -2.918099880218506   2.918099880218506  -4.863500118255615
Pd              85       46
 -0.972700595855713   0.972699642181396  -4.863500118255615
Pd              86       46
  0.972699642181396   0.972699642181396  -6.808899879455566
Pd              87       46
  2.918099880218506   2.918099880218506  -6.808899879455566
Pd              88       46
```

```
  0.972699642181396   2.918099880218506  -4.863500118255615
Pd              89       46
  2.918099880218506   0.972699642181396  -4.863500118255615
Pd              90       46
  4.863500118255615   0.972699642181396  -6.808899879455566
Pd              91       46
  6.808900356292725   2.918099880218506  -6.808899879455566
Pd              92       46
  4.863500118255615   2.918099880218506  -4.863500118255615
Pd              93       46
  6.808900356292725   0.972699642181396  -4.863500118255615
Pd              94       46
  8.754301071166992   0.972699642181396  -6.808899879455566
Pd              95       46
  8.754301071166992   2.918099880218506  -4.863500118255615
Pd              96       46
 -8.754300117492676   4.863500118255615  -4.863500118255615
Pd              97       46
 -6.808899879455566   4.863500118255615  -6.808899879455566
Pd              98       46
 -4.863500118255615   6.808900356292725  -6.808899879455566
Pd              99       46
 -6.808899879455566   6.808900356292725  -4.863500118255615
Pd              100      46
 -4.863500118255615   4.863500118255615  -4.863500118255615
Pd              101      46
 -2.918099880218506   4.863500118255615  -6.808899879455566
Pd              102      46
 -0.972700595855713   6.808900356292725  -6.808899879455566
Pd              103      46
 -2.918099880218506   6.808900356292725  -4.863500118255615
Pd              104      46
 -0.972700595855713   4.863500118255615  -4.863500118255615
Pd              105      46
  0.972699642181396   4.863500118255615  -6.808899879455566
Pd              106      46
```

```
  2.918099880218506   6.808900356292725  -6.808899879455566
Pd              107       46
  0.972699642181396   6.808900356292725  -4.863500118255615
Pd              108       46
  2.918099880218506   4.863500118255615  -4.863500118255615
Pd              109       46
  4.863500118255615   4.863500118255615  -6.808899879455566
Pd              110       46
  4.863500118255615   6.808900356292725  -4.863500118255615
Pd              111       46
  6.808900356292725   4.863500118255615  -4.863500118255615
Pd              112       46
 -4.863500118255615   8.754301071166992  -4.863500118255615
Pd              113       46
 -2.918099880218506   8.754301071166992  -6.808899879455566
Pd              114       46
 -0.972700595855713   8.754301071166992  -4.863500118255615
Pd              115       46
  0.972699642181396   8.754301071166992  -6.808899879455566
Pd              116       46
  2.918099880218506   8.754301071166992  -4.863500118255615
Pd              117       46
 -4.863500118255615  -8.754300117492676  -2.918099880218506
Pd              118       46
 -6.808899879455566  -8.754300117492676  -0.972700595855713
Pd              119       46
 -2.918099880218506 -10.699700355529785  -2.918099880218506
Pd              120       46
 -0.972700595855713  -8.754300117492676  -2.918099880218506
Pd              121       46
 -2.918099880218506  -8.754300117492676  -0.972700595855713
Pd              122       46
 -0.972700595855713 -10.699700355529785  -0.972700595855713
Pd              123       46
  0.972699642181396 -10.699700355529785  -2.918099880218506
Pd              124       46
```

```
  2.918099880218506  -8.754300117492676  -2.918099880218506
Pd              125       46
  0.972699642181396  -8.754300117492676  -0.972700595855713
Pd              126       46
  2.918099880218506 -10.699700355529785  -0.972700595855713
Pd              127       46
  6.808900356292725  -8.754300117492676  -2.918099880218506
Pd              128       46
  4.863500118255615  -8.754300117492676  -0.972700595855713
Pd              129       46
 -8.754300117492676  -4.863500118255615  -2.918099880218506
Pd              130       46
 -8.754300117492676  -6.808899879455566  -0.972700595855713
Pd              131       46
 -6.808899879455566  -6.808899879455566  -2.918099880218506
Pd              132       46
 -4.863500118255615  -4.863500118255615  -2.918099880218506
Pd              133       46
 -6.808899879455566  -4.863500118255615  -0.972700595855713
Pd              134       46
 -4.863500118255615  -6.808899879455566  -0.972700595855713
Pd              135       46
 -2.918099880218506  -6.808899879455566  -2.918099880218506
Pd              136       46
 -0.972700595855713  -4.863500118255615  -2.918099880218506
Pd              137       46
 -2.918099880218506  -4.863500118255615  -0.972700595855713
Pd              138       46
 -0.972700595855713  -6.808899879455566  -0.972700595855713
Pd              139       46
  0.972699642181396  -6.808899879455566  -2.918099880218506
Pd              140       46
  2.918099880218506  -4.863500118255615  -2.918099880218506
Pd              141       46
  0.972699642181396  -4.863500118255615  -0.972700595855713
Pd              142       46
```

```
  2.918099880218506  -6.808899879455566  -0.972700595855713
Pd              143       46
  4.863500118255615  -6.808899879455566  -2.918099880218506
Pd              144       46
  6.808900356292725  -4.863500118255615  -2.918099880218506
Pd              145       46
  4.863500118255615  -4.863500118255615  -0.972700595855713
Pd              146       46
  6.808900356292725  -6.808899879455566  -0.972700595855713
Pd              147       46
  8.754301071166992  -6.808899879455566  -2.918099880218506
Pd              148       46
  8.754301071166992  -4.863500118255615  -0.972700595855713
Pd              149       46
-10.699700355529785  -2.918099880218506  -2.918099880218506
Pd              150       46
 -8.754300117492676  -0.972700595855713  -2.918099880218506
Pd              151       46
-10.699700355529785  -0.972700595855713  -0.972700595855713
Pd              152       46
 -8.754300117492676  -2.918099880218506  -0.972700595855713
Pd              153       46
 -6.808899879455566  -2.918099880218506  -2.918099880218506
Pd              154       46
 -4.863500118255615  -0.972700595855713  -2.918099880218506
Pd              155       46
 -6.808899879455566  -0.972700595855713  -0.972700595855713
Pd              156       46
 -4.863500118255615  -2.918099880218506  -0.972700595855713
Pd              157       46
 -2.918099880218506  -2.918099880218506  -2.918099880218506
Pd              158       46
 -0.972700595855713  -0.972700595855713  -2.918099880218506
Pd              159       46
 -2.918099880218506  -0.972700595855713  -0.972700595855713
Pd              160       46
```

```
 -0.972700595855713  -2.918099880218506  -0.972700595855713
Pd              161       46
  0.972699642181396  -2.918099880218506  -2.918099880218506
Pd              162       46
  2.918099880218506  -0.972700595855713  -2.918099880218506
Pd              163       46
  0.972699642181396  -0.972700595855713  -0.972700595855713
Pd              164       46
  2.918099880218506  -2.918099880218506  -0.972700595855713
Pd              165       46
  4.863500118255615  -2.918099880218506  -2.918099880218506
Pd              166       46
  6.808900356292725  -0.972700595855713  -2.918099880218506
Pd              167       46
  4.863500118255615  -0.972700595855713  -0.972700595855713
Pd              168       46
  6.808900356292725  -2.918099880218506  -0.972700595855713
Pd              169       46
  8.754301071166992  -2.918099880218506  -2.918099880218506
Pd              170       46
 10.699701309204102  -0.972700595855713  -2.918099880218506
Pd              171       46
  8.754301071166992  -0.972700595855713  -0.972700595855713
Pd              172       46
 10.699701309204102  -2.918099880218506  -0.972700595855713
Pd              173       46
-10.699700355529785   0.972699642181396  -2.918099880218506
Pd              174       46
 -8.754300117492676   2.918099880218506  -2.918099880218506
Pd              175       46
-10.699700355529785   2.918099880218506  -0.972700595855713
Pd              176       46
 -8.754300117492676   0.972699642181396  -0.972700595855713
Pd              177       46
 -6.808899879455566   0.972699642181396  -2.918099880218506
Pd              178       46
```

```
 -4.863500118255615   2.918099880218506  -2.918099880218506
Pd              179       46
 -6.808899879455566   2.918099880218506  -0.972700595855713
Pd              180       46
 -4.863500118255615   0.972699642181396  -0.972700595855713
Pd              181       46
 -2.918099880218506   0.972699642181396  -2.918099880218506
Pd              182       46
 -0.972700595855713   2.918099880218506  -2.918099880218506
Pd              183       46
 -2.918099880218506   2.918099880218506  -0.972700595855713
Pd              184       46
 -0.972700595855713   0.972699642181396  -0.972700595855713
Pd              185       46
  0.972699642181396   0.972699642181396  -2.918099880218506
Pd              186       46
  2.918099880218506   2.918099880218506  -2.918099880218506
Pd              187       46
  0.972699642181396   2.918099880218506  -0.972700595855713
Pd              188       46
  2.918099880218506   0.972699642181396  -0.972700595855713
Pd              189       46
  4.863500118255615   0.972699642181396  -2.918099880218506
Pd              190       46
  6.808900356292725   2.918099880218506  -2.918099880218506
Pd              191       46
  4.863500118255615   2.918099880218506  -0.972700595855713
Pd              192       46
  6.808900356292725   0.972699642181396  -0.972700595855713
Pd              193       46
  8.754301071166992   0.972699642181396  -2.918099880218506
Pd              194       46
 10.699701309204102   2.918099880218506  -2.918099880218506
Pd              195       46
  8.754301071166992   2.918099880218506  -0.972700595855713
Pd              196       46
```

```
 10.699701309204102   0.972699642181396  -0.972700595855713
Pd              197       46
 -8.754300117492676   6.808900356292725  -2.918099880218506
Pd              198       46
 -8.754300117492676   4.863500118255615  -0.972700595855713
Pd              199       46
 -6.808899879455566   4.863500118255615  -2.918099880218506
Pd              200       46
 -4.863500118255615   6.808900356292725  -2.918099880218506
Pd              201       46
 -6.808899879455566   6.808900356292725  -0.972700595855713
Pd              202       46
 -4.863500118255615   4.863500118255615  -0.972700595855713
Pd              203       46
 -2.918099880218506   4.863500118255615  -2.918099880218506
Pd              204       46
 -0.972700595855713   6.808900356292725  -2.918099880218506
Pd              205       46
 -2.918099880218506   6.808900356292725  -0.972700595855713
Pd              206       46
 -0.972700595855713   4.863500118255615  -0.972700595855713
Pd              207       46
  0.972699642181396   4.863500118255615  -2.918099880218506
Pd              208       46
  2.918099880218506   6.808900356292725  -2.918099880218506
Pd              209       46
  0.972699642181396   6.808900356292725  -0.972700595855713
Pd              210       46
  2.918099880218506   4.863500118255615  -0.972700595855713
Pd              211       46
  4.863500118255615   4.863500118255615  -2.918099880218506
Pd              212       46
  6.808900356292725   6.808900356292725  -2.918099880218506
Pd              213       46
  4.863500118255615   6.808900356292725  -0.972700595855713
Pd              214       46
```

```
  6.808900356292725   4.863500118255615  -0.972700595855713
Pd              215       46
  8.754301071166992   4.863500118255615  -2.918099880218506
Pd              216       46
  8.754301071166992   6.808900356292725  -0.972700595855713
Pd              217       46
 -6.808899879455566   8.754301071166992  -2.918099880218506
Pd              218       46
 -4.863500118255615   8.754301071166992  -0.972700595855713
Pd              219       46
 -2.918099880218506   8.754301071166992  -2.918099880218506
Pd              220       46
 -0.972700595855713  10.699701309204102  -2.918099880218506
Pd              221       46
 -2.918099880218506  10.699701309204102  -0.972700595855713
Pd              222       46
 -0.972700595855713   8.754301071166992  -0.972700595855713
Pd              223       46
  0.972699642181396   8.754301071166992  -2.918099880218506
Pd              224       46
  2.918099880218506  10.699701309204102  -2.918099880218506
Pd              225       46
  0.972699642181396  10.699701309204102  -0.972700595855713
Pd              226       46
  2.918099880218506   8.754301071166992  -0.972700595855713
Pd              227       46
  4.863500118255615   8.754301071166992  -2.918099880218506
Pd              228       46
  6.808900356292725   8.754301071166992  -0.972700595855713
Pd              229       46
 -4.863500118255615  -8.754300117492676   0.972699642181396
Pd              230       46
 -6.808899879455566  -8.754300117492676   2.918099880218506
Pd              231       46
 -2.918099880218506 -10.699700355529785   0.972699642181396
Pd              232       46
```

```
 -0.972700595855713  -8.754300117492676   0.972699642181396
Pd              233       46
 -2.918099880218506  -8.754300117492676   2.918099880218506
Pd              234       46
 -0.972700595855713 -10.699700355529785   2.918099880218506
Pd              235       46
  0.972699642181396 -10.699700355529785   0.972699642181396
Pd              236       46
  2.918099880218506  -8.754300117492676   0.972699642181396
Pd              237       46
  0.972699642181396  -8.754300117492676   2.918099880218506
Pd              238       46
  2.918099880218506 -10.699700355529785   2.918099880218506
Pd              239       46
  6.808900356292725  -8.754300117492676   0.972699642181396
Pd              240       46
  4.863500118255615  -8.754300117492676   2.918099880218506
Pd              241       46
 -8.754300117492676  -4.863500118255615   0.972699642181396
Pd              242       46
 -8.754300117492676  -6.808899879455566   2.918099880218506
Pd              243       46
 -6.808899879455566  -6.808899879455566   0.972699642181396
Pd              244       46
 -4.863500118255615  -4.863500118255615   0.972699642181396
Pd              245       46
 -6.808899879455566  -4.863500118255615   2.918099880218506
Pd              246       46
 -4.863500118255615  -6.808899879455566   2.918099880218506
Pd              247       46
 -2.918099880218506  -6.808899879455566   0.972699642181396
Pd              248       46
 -0.972700595855713  -4.863500118255615   0.972699642181396
Pd              249       46
 -2.918099880218506  -4.863500118255615   2.918099880218506
Pd              250       46
```

```
 -0.972700595855713  -6.808899879455566   2.918099880218506
Pd              251       46
  0.972699642181396  -6.808899879455566   0.972699642181396
Pd              252       46
  2.918099880218506  -4.863500118255615   0.972699642181396
Pd              253       46
  0.972699642181396  -4.863500118255615   2.918099880218506
Pd              254       46
  2.918099880218506  -6.808899879455566   2.918099880218506
Pd              255       46
  4.863500118255615  -6.808899879455566   0.972699642181396
Pd              256       46
  6.808900356292725  -4.863500118255615   0.972699642181396
Pd              257       46
  4.863500118255615  -4.863500118255615   2.918099880218506
Pd              258       46
  6.808900356292725  -6.808899879455566   2.918099880218506
Pd              259       46
  8.754301071166992  -6.808899879455566   0.972699642181396
Pd              260       46
  8.754301071166992  -4.863500118255615   2.918099880218506
Pd              261       46
-10.699700355529785  -2.918099880218506   0.972699642181396
Pd              262       46
 -8.754300117492676  -0.972700595855713   0.972699642181396
Pd              263       46
-10.699700355529785  -0.972700595855713   2.918099880218506
Pd              264       46
 -8.754300117492676  -2.918099880218506   2.918099880218506
Pd              265       46
 -6.808899879455566  -2.918099880218506   0.972699642181396
Pd              266       46
 -4.863500118255615  -0.972700595855713   0.972699642181396
Pd              267       46
 -6.808899879455566  -0.972700595855713   2.918099880218506
Pd              268       46
```

```
 -4.863500118255615  -2.918099880218506   2.918099880218506
Pd              269       46
 -2.918099880218506  -2.918099880218506   0.972699642181396
Pd              270       46
 -0.972700595855713  -0.972700595855713   0.972699642181396
Pd              271       46
 -2.918099880218506  -0.972700595855713   2.918099880218506
Pd              272       46
 -0.972700595855713  -2.918099880218506   2.918099880218506
Pd              273       46
  0.972699642181396  -2.918099880218506   0.972699642181396
Pd              274       46
  2.918099880218506  -0.972700595855713   0.972699642181396
Pd              275       46
  0.972699642181396  -0.972700595855713   2.918099880218506
Pd              276       46
  2.918099880218506  -2.918099880218506   2.918099880218506
Pd              277       46
  4.863500118255615  -2.918099880218506   0.972699642181396
Pd              278       46
  6.808900356292725  -0.972700595855713   0.972699642181396
Pd              279       46
  4.863500118255615  -0.972700595855713   2.918099880218506
Pd              280       46
  6.808900356292725  -2.918099880218506   2.918099880218506
Pd              281       46
  8.754301071166992  -2.918099880218506   0.972699642181396
Pd              282       46
 10.699701309204102  -0.972700595855713   0.972699642181396
Pd              283       46
  8.754301071166992  -0.972700595855713   2.918099880218506
Pd              284       46
 10.699701309204102  -2.918099880218506   2.918099880218506
Pd              285       46
-10.699700355529785   0.972699642181396   0.972699642181396
Pd              286       46
```

```
 -8.754300117492676   2.918099880218506   0.972699642181396
Pd              287       46
-10.699700355529785   2.918099880218506   2.918099880218506
Pd              288       46
 -8.754300117492676   0.972699642181396   2.918099880218506
Pd              289       46
 -6.808899879455566   0.972699642181396   0.972699642181396
Pd              290       46
 -4.863500118255615   2.918099880218506   0.972699642181396
Pd              291       46
 -6.808899879455566   2.918099880218506   2.918099880218506
Pd              292       46
 -4.863500118255615   0.972699642181396   2.918099880218506
Pd              293       46
 -2.918099880218506   0.972699642181396   0.972699642181396
Pd              294       46
 -0.972700595855713   2.918099880218506   0.972699642181396
Pd              295       46
 -2.918099880218506   2.918099880218506   2.918099880218506
Pd              296       46
 -0.972700595855713   0.972699642181396   2.918099880218506
Pd              297       46
  0.972699642181396   0.972699642181396   0.972699642181396
Pd              298       46
  2.918099880218506   2.918099880218506   0.972699642181396
Pd              299       46
  0.972699642181396   2.918099880218506   2.918099880218506
Pd              300       46
  2.918099880218506   0.972699642181396   2.918099880218506
Pd              301       46
  4.863500118255615   0.972699642181396   0.972699642181396
Pd              302       46
  6.808900356292725   2.918099880218506   0.972699642181396
Pd              303       46
  4.863500118255615   2.918099880218506   2.918099880218506
Pd              304       46
```

Appendix A (Continued)

```
  6.808900356292725   0.972699642181396   2.918099880218506
Pd              305       46
  8.754301071166992   0.972699642181396   0.972699642181396
Pd              306       46
 10.699701309204102   2.918099880218506   0.972699642181396
Pd              307       46
  8.754301071166992   2.918099880218506   2.918099880218506
Pd              308       46
 10.699701309204102   0.972699642181396   2.918099880218506
Pd              309       46
 -8.754300117492676   6.808900356292725   0.972699642181396
Pd              310       46
 -8.754300117492676   4.863500118255615   2.918099880218506
Pd              311       46
 -6.808899879455566   4.863500118255615   0.972699642181396
Pd              312       46
 -4.863500118255615   6.808900356292725   0.972699642181396
Pd              313       46
 -6.808899879455566   6.808900356292725   2.918099880218506
Pd              314       46
 -4.863500118255615   4.863500118255615   2.918099880218506
Pd              315       46
 -2.918099880218506   4.863500118255615   0.972699642181396
Pd              316       46
 -0.972700595855713   6.808900356292725   0.972699642181396
Pd              317       46
 -2.918099880218506   6.808900356292725   2.918099880218506
Pd              318       46
 -0.972700595855713   4.863500118255615   2.918099880218506
Pd              319       46
  0.972699642181396   4.863500118255615   0.972699642181396
Pd              320       46
  2.918099880218506   6.808900356292725   0.972699642181396
Pd              321       46
  0.972699642181396   6.808900356292725   2.918099880218506
Pd              322       46
```

```
  2.918099880218506   4.863500118255615   2.918099880218506
Pd              323       46
  4.863500118255615   4.863500118255615   0.972699642181396
Pd              324       46
  6.808900356292725   6.808900356292725   0.972699642181396
Pd              325       46
  4.863500118255615   6.808900356292725   2.918099880218506
Pd              326       46
  6.808900356292725   4.863500118255615   2.918099880218506
Pd              327       46
  8.754301071166992   4.863500118255615   0.972699642181396
Pd              328       46
  8.754301071166992   6.808900356292725   2.918099880218506
Pd              329       46
 -6.808899879455566   8.754301071166992   0.972699642181396
Pd              330       46
 -4.863500118255615   8.754301071166992   2.918099880218506
Pd              331       46
 -2.918099880218506   8.754301071166992   0.972699642181396
Pd              332       46
 -0.972700595855713  10.699701309204102   0.972699642181396
Pd              333       46
 -2.918099880218506  10.699701309204102   2.918099880218506
Pd              334       46
 -0.972700595855713   8.754301071166992   2.918099880218506
Pd              335       46
  0.972699642181396   8.754301071166992   0.972699642181396
Pd              336       46
  2.918099880218506  10.699701309204102   0.972699642181396
Pd              337       46
  0.972699642181396  10.699701309204102   2.918099880218506
Pd              338       46
  2.918099880218506   8.754301071166992   2.918099880218506
Pd              339       46
  4.863500118255615   8.754301071166992   0.972699642181396
Pd              340       46
```

```
  6.808900356292725   8.754301071166992   2.918099880218506
Pd              341       46
 -4.863500118255615  -8.754300117492676   4.863500118255615
Pd              342       46
 -0.972700595855713  -8.754300117492676   4.863500118255615
Pd              343       46
 -2.918099880218506  -8.754300117492676   6.808900356292725
Pd              344       46
  2.918099880218506  -8.754300117492676   4.863500118255615
Pd              345       46
  0.972699642181396  -8.754300117492676   6.808900356292725
Pd              346       46
 -8.754300117492676  -4.863500118255615   4.863500118255615
Pd              347       46
 -6.808899879455566  -6.808899879455566   4.863500118255615
Pd              348       46
 -4.863500118255615  -4.863500118255615   4.863500118255615
Pd              349       46
 -6.808899879455566  -4.863500118255615   6.808900356292725
Pd              350       46
 -4.863500118255615  -6.808899879455566   6.808900356292725
Pd              351       46
 -2.918099880218506  -6.808899879455566   4.863500118255615
Pd              352       46
 -0.972700595855713  -4.863500118255615   4.863500118255615
Pd              353       46
 -2.918099880218506  -4.863500118255615   6.808900356292725
Pd              354       46
 -0.972700595855713  -6.808899879455566   6.808900356292725
Pd              355       46
  0.972699642181396  -6.808899879455566   4.863500118255615
Pd              356       46
  2.918099880218506  -4.863500118255615   4.863500118255615
Pd              357       46
  0.972699642181396  -4.863500118255615   6.808900356292725
Pd              358       46
```

```
  2.918099880218506  -6.808899879455566   6.808900356292725
Pd              359       46
  4.863500118255615  -6.808899879455566   4.863500118255615
Pd              360       46
  6.808900356292725  -4.863500118255615   4.863500118255615
Pd              361       46
  4.863500118255615  -4.863500118255615   6.808900356292725
Pd              362       46
 -8.754300117492676  -0.972700595855713   4.863500118255615
Pd              363       46
 -8.754300117492676  -2.918099880218506   6.808900356292725
Pd              364       46
 -6.808899879455566  -2.918099880218506   4.863500118255615
Pd              365       46
 -4.863500118255615  -0.972700595855713   4.863500118255615
Pd              366       46
 -6.808899879455566  -0.972700595855713   6.808900356292725
Pd              367       46
 -4.863500118255615  -2.918099880218506   6.808900356292725
Pd              368       46
 -2.918099880218506  -2.918099880218506   4.863500118255615
Pd              369       46
 -0.972700595855713  -0.972700595855713   4.863500118255615
Pd              370       46
 -2.918099880218506  -0.972700595855713   6.808900356292725
Pd              371       46
 -0.972700595855713  -2.918099880218506   6.808900356292725
Pd              372       46
  0.972699642181396  -2.918099880218506   4.863500118255615
Pd              373       46
  2.918099880218506  -0.972700595855713   4.863500118255615
Pd              374       46
  0.972699642181396  -0.972700595855713   6.808900356292725
Pd              375       46
  2.918099880218506  -2.918099880218506   6.808900356292725
Pd              376       46
```

```
  4.863500118255615  -2.918099880218506   4.863500118255615
Pd             377       46
  6.808900356292725  -0.972700595855713   4.863500118255615
Pd             378       46
  4.863500118255615  -0.972700595855713   6.808900356292725
Pd             379       46
  6.808900356292725  -2.918099880218506   6.808900356292725
Pd             380       46
  8.754301071166992  -2.918099880218506   4.863500118255615
Pd             381       46
  8.754301071166992  -0.972700595855713   6.808900356292725
Pd             382       46
 -8.754300117492676   2.918099880218506   4.863500118255615
Pd             383       46
 -8.754300117492676   0.972699642181396   6.808900356292725
Pd             384       46
 -6.808899879455566   0.972699642181396   4.863500118255615
Pd             385       46
 -4.863500118255615   2.918099880218506   4.863500118255615
Pd             386       46
 -6.808899879455566   2.918099880218506   6.808900356292725
Pd             387       46
 -4.863500118255615   0.972699642181396   6.808900356292725
Pd             388       46
 -2.918099880218506   0.972699642181396   4.863500118255615
Pd             389       46
 -0.972700595855713   2.918099880218506   4.863500118255615
Pd             390       46
 -2.918099880218506   2.918099880218506   6.808900356292725
Pd             391       46
 -0.972700595855713   0.972699642181396   6.808900356292725
Pd             392       46
  0.972699642181396   0.972699642181396   4.863500118255615
Pd             393       46
  2.918099880218506   2.918099880218506   4.863500118255615
Pd             394       46
```

```
  0.972699642181396   2.918099880218506   6.808900356292725
Pd              395       46
  2.918099880218506   0.972699642181396   6.808900356292725
Pd              396       46
  4.863500118255615   0.972699642181396   4.863500118255615
Pd              397       46
  6.808900356292725   2.918099880218506   4.863500118255615
Pd              398       46
  4.863500118255615   2.918099880218506   6.808900356292725
Pd              399       46
  6.808900356292725   0.972699642181396   6.808900356292725
Pd              400       46
  8.754301071166992   0.972699642181396   4.863500118255615
Pd              401       46
  8.754301071166992   2.918099880218506   6.808900356292725
Pd              402       46
 -6.808899879455566   4.863500118255615   4.863500118255615
Pd              403       46
 -4.863500118255615   6.808900356292725   4.863500118255615
Pd              404       46
 -4.863500118255615   4.863500118255615   6.808900356292725
Pd              405       46
 -2.918099880218506   4.863500118255615   4.863500118255615
Pd              406       46
 -0.972700595855713   6.808900356292725   4.863500118255615
Pd              407       46
 -2.918099880218506   6.808900356292725   6.808900356292725
Pd              408       46
 -0.972700595855713   4.863500118255615   6.808900356292725
Pd              409       46
  0.972699642181396   4.863500118255615   4.863500118255615
Pd              410       46
  2.918099880218506   6.808900356292725   4.863500118255615
Pd              411       46
  0.972699642181396   6.808900356292725   6.808900356292725
Pd              412       46
```

```
  2.918099880218506   4.863500118255615   6.808900356292725
Pd              413       46
  4.863500118255615   4.863500118255615   4.863500118255615
Pd              414       46
  6.808900356292725   6.808900356292725   4.863500118255615
Pd              415       46
  4.863500118255615   6.808900356292725   6.808900356292725
Pd              416       46
  6.808900356292725   4.863500118255615   6.808900356292725
Pd              417       46
  8.754301071166992   4.863500118255615   4.863500118255615
Pd              418       46
 -2.918099880218506   8.754301071166992   4.863500118255615
Pd              419       46
 -0.972700595855713   8.754301071166992   6.808900356292725
Pd              420       46
  0.972699642181396   8.754301071166992   4.863500118255615
Pd              421       46
  2.918099880218506   8.754301071166992   6.808900356292725
Pd              422       46
  4.863500118255615   8.754301071166992   4.863500118255615
Pd              423       46
 -4.863500118255615  -4.863500118255615   8.754301071166992
Pd              424       46
 -2.918099880218506  -6.808899879455566   8.754301071166992
Pd              425       46
 -0.972700595855713  -4.863500118255615   8.754301071166992
Pd              426       46
  0.972699642181396  -6.808899879455566   8.754301071166992
Pd              427       46
  2.918099880218506  -4.863500118255615   8.754301071166992
Pd              428       46
 -6.808899879455566  -2.918099880218506   8.754301071166992
Pd              429       46
 -4.863500118255615  -0.972700595855713   8.754301071166992
Pd              430       46
```

```
 -2.918099880218506  -2.918099880218506   8.754301071166992
Pd              431       46
 -0.972700595855713  -0.972700595855713   8.754301071166992
Pd              432       46
 -2.918099880218506  -0.972700595855713  10.699701309204102
Pd              433       46
 -0.972700595855713  -2.918099880218506  10.699701309204102
Pd              434       46
  0.972699642181396  -2.918099880218506   8.754301071166992
Pd              435       46
  2.918099880218506  -0.972700595855713   8.754301071166992
Pd              436       46
  0.972699642181396  -0.972700595855713  10.699701309204102
Pd              437       46
  2.918099880218506  -2.918099880218506  10.699701309204102
Pd              438       46
  4.863500118255615  -2.918099880218506   8.754301071166992
Pd              439       46
  6.808900356292725  -0.972700595855713   8.754301071166992
Pd              440       46
 -6.808899879455566   0.972699642181396   8.754301071166992
Pd              441       46
 -4.863500118255615   2.918099880218506   8.754301071166992
Pd              442       46
 -2.918099880218506   0.972699642181396   8.754301071166992
Pd              443       46
 -0.972700595855713   2.918099880218506   8.754301071166992
Pd              444       46
 -2.918099880218506   2.918099880218506  10.699701309204102
Pd              445       46
 -0.972700595855713   0.972699642181396  10.699701309204102
Pd              446       46
  0.972699642181396   0.972699642181396   8.754301071166992
Pd              447       46
  2.918099880218506   2.918099880218506   8.754301071166992
Pd              448       46
```

```
  0.972699642181396   2.918099880218506  10.699701309204102
Pd              449       46
  2.918099880218506   0.972699642181396  10.699701309204102
Pd              450       46
  4.863500118255615   0.972699642181396   8.754301071166992
Pd              451       46
  6.808900356292725   2.918099880218506   8.754301071166992
Pd              452       46
 -2.918099880218506   4.863500118255615   8.754301071166992
Pd              453       46
 -0.972700595855713   6.808900356292725   8.754301071166992
Pd              454       46
  0.972699642181396   4.863500118255615   8.754301071166992
Pd              455       46
  2.918099880218506   6.808900356292725   8.754301071166992
Pd              456       46
  4.863500118255615   4.863500118255615   8.754301071166992
```

The first line in the CONFIG file has the same definition as that in the CONTROL file. The first zero in the second line indicate only atomic coordinates are included in the file. The second integer is the periodic boundary key, where zero means no periodic boundaries. If periodic boundary condition is used, a three-line cell vectors needs to be defined after the second line, otherwise the x, y, z coordinates will be listed without the three lines. Before each atomic coordinate line, atom name, atom index and atomic number are listed in the order of increasing index.

A.1.3 The FIELD File

The FIELD file contains the force field information defining the nature of the molecular forces. The FIELD file used for the simulated Pd nanocluster is shown below.

```
DL_POLY FIELD file: Pd nanocluster
```

```
units ev
molecules 1
Palladium
nummols 456
atoms 1
Pd      106.420       0.0000
finish
vdw 1
Pd      Pd      stch    0.004179    3.89      12.0        7.0         108.27
Close
```

The first line the FIELD file is the title. It must be followed by the units. In our simulations the energy unit of eV is used. Lines following that are molecular details. The first line in the molecular details specify the number of different types of molecules. The details of each type of molecule include the name of the molecule and total number of this molecule in the system. Each atomic information in this molecule is then given by atom name, atomic mass and atomic charge. A directive of finish is entered to signal to DL_POLY_2 that the entry of the details of a molecule has been completed. The entries for a second molecule may now be entered, and the cycle is repeated until all types of molecules indicated by the molecules directive have been entered. Since the in our simulation Pd nanocluster has only one type of molecule/atom, the repeating is not needed. The non-bonded interactions are identified by atom types. The Sutton-Chen potential for Pd-Pd interactions is signaled by the directive stch with corresponding parameters. In the end, the FIELD file must be closed with the directive close.

A.2 The Output Files

DL_POLY_2 produces up to seven output files: HISTORY, OUTPUT, REVCON, REVIVE, RDFDAT, ZDNDAT and STATIS, depending on the directives in the CONTROL file. These respectively contain: a dump file of atomic coordinates, velocities and forces; a summary of the simulation; the restart configuration; statistics accumulators; radial distribution data, Z-density data and a statistical history. The format of each output file can be found in the DL_POLY_s manual.

Appendix B: VASP Programs

VASP 4.6.28 was used for the DFT calculations in this dissertation. VASP uses a relatively large number of input and output files. A short description of some of the important files are given in the example of Pd fully coated SWNT(10,0) in this chapter.

B.1 The Input Files

In order to run a VASP job, at least four input files are needed. They are INCAR, POTCAR, POSCAR, and KPOINTS files.

B.1.1 The INCAR File

INCAR is the central input of VASP. It determines what to do and how to do it, and contains a relatively large number of parameters. However, since most of these parameters have convenient defaults, INCAR file is usually simply. An INCAR file for the total energy calculation of Pd fully coated SWNT(10,0) is given below.

```
SYSTEM  = Pd fully coated SWNT(10,0)
Start parameter for this run
PREC    = Accurate
ISPIN   = 2
Electronic relaxation 1
ENCUT   = 500
NELMDL  = -10
EDIFF   = 1E-04
VOSKOWN = 1
Ironic relaxation
EDIFFG  = 1E-03
NSW     = 0
IBRION  = -1
ISIF    = 2
```

The meaning of directives listed this INCAR file are as follows:

- SYSTEM tag is followed by the title string to help user to identify the system.
- PREC tag determines the energy cutoff, if no value is given for ENCUT in the INCAR. For PREC=Accurate, ENCUT is set to the maximal ENMAX value in the POTCAR file plus 30%. PREC= Accurate avoids wrap around errors and uses an augmentation grid that is exactly twice as large as the course grid for the representation of the pseudo wave functions. PREC=Accurate increases the memory requirements somewhat, but it should be used if accurate forces and energies are required.
- ISPIN determines whether spin polarized calculations are performed, where 2 is for spin polarized calculations.
- ENCUT is the cut-off energy for plane waves basis set in eV, as discussed in Chapter Seven.
- NELMDL gives the number of non-selfconsistent steps at the beginning; if one initializes the wave functions randomly the initial wave functions are far from anything reasonable. A value of -10 results in a 10-step delay for the start-configuration.
- EDIFF Specifies the global break condition for the electronic self-consistent loop. The relaxation of the electronic degrees of freedom will be stopped if the total (free) energy change and the band structure energy change ("change of eigenvalues") between two steps are both smaller than 1E-04.
- VOSKOWN=1 turn on the Vosko-Wilk-Nusair interpolation formula for the correlation part of the exchange correlation functional. This usually enhances the magnetic moments and the magnetic energies. It is desirable to use this interpolation whenever the PW91 functional is applied.

- EDIFFG=1E-03 states if the total (free) energy between two ionic steps is smaller than 10-3, the ionic relaxation loop will stop.
- IBRION=-1 indicates ions will not be updated or moved. If IBRION=2 is defined, a conjugate-gradient algorithm will be used to relax the ions into their instantaneous ground state.
- NSW defines the number of ionic steps. It should be zero if IBRION=-1 is defined in INCAR file. If an ionic relaxation is performed, i.e. IBRION=-2, a positive NSW should be used.
- ISIF controls whether the stress tensor is calculated. In addition, it also determines which degrees of freedom (ions, cell volume, cell shape) are allowed to change. ISIF=2 is a default set for IBRION≠0.

B.1.2 The POSCAR File

This file contains the lattice geometry and the ionic positions, optionally also starting velocities and predictor-corrector coordinates for a MD-run. The coordinates for SWNTs can be generated using TubeGen Online. The POSCAR of Pd fully coated SWNT(10,0) is shown below.

```
   CNT(10,0)-Pdfullcover
    1.000000000000000
    19.1126456549789300   10.7330367637471300    0.0000149140521125
     0.0000580931183641   -0.0001110915924111   -4.2919968268296320
    -0.3878849318882599   22.1354734425387000    0.0005846469432516
  40  20
Direct
  0.5730235429675119  0.8330924087047578  0.1347674198436266
```

0.4284796001067903	0.1668926871836973	0.8648536625587369
0.4284796946512301	0.8330791708865419	0.8648512053138973
0.5730251167132323	0.1670264718729868	0.1347684193137511
0.4446167196771214	0.8331993555307236	0.1997764766189718
0.5568638447413861	0.1669419855081387	0.7995882231241254
0.5568641969022039	0.8329963210444333	0.7995886899596130
0.4446169614371343	0.1669617548056479	0.1997742675413647
0.3040676683703012	0.3331732331433628	0.1559314109024541
0.6967190894797994	0.6668409546215486	0.8443979997476063
0.6967190744745224	0.3331244062104446	0.8443985730891725
0.3040697776228782	0.6669854842377703	0.1559307936110770
0.3851432622283681	0.3331515560971354	0.2048413248878092
0.6162026419957130	0.6668983203063732	0.7948968661175968
0.6162036292845769	0.3330416612997809	0.7948961506890768
0.3851438826014473	0.6670146949619991	0.2048413092415728
0.2999163285682087	0.3330673693381385	0.0459241534056574
0.7017554441095371	0.6669799379875485	0.9539516107590060
0.7017541553847551	0.3330467196378990	0.9539527370850251
0.2999175935679261	0.6670182046167312	0.0459247522986814
0.6743484367570360	0.8331067977217543	0.0182293607363064
0.3275789213419174	0.1668813879758773	0.9816675581370617
0.3275799680051250	0.8331608378148943	0.9816672388197674
0.6743484533825921	0.1669529937251255	0.0182288568258002
0.6299423529113213	0.6669726619533662	0.0805259355444719
0.3717661956026035	0.3330188794804130	0.9193130487637688
0.3717650233813501	0.6669836990327767	0.9193131055507777
0.6299427138691271	0.3331208301089248	0.0805271568464931
0.5091821720000027	0.6669811752444303	0.1757417410070019
0.4922530355319807	0.3331433753515185	0.8236259008850624
0.4922529714597985	0.6668056260692765	0.8236246706400081
0.5091813049284468	0.3331606991210450	0.1757424777175132
0.3364979495809308	0.8330700134712288	0.1899805440847686
0.6644965076555494	0.1669589042232005	0.8102118198415553
0.6644965030948455	0.8329905343497330	0.8102124124881627
0.3364965990840787	0.1670971680996445	0.1899817172593217
0.2915947790741029	0.8332287727865832	0.1060628585158980

```
0.7094980915883724  0.1668311056433822  0.8940258080240611
0.7094989105616207  0.8331640068262516  0.8940259113864570
0.2915936702657689  0.1669004319194229  0.1060641889645453
0.2523288352820288  0.0000873956505458  0.2894911142560943
0.3263772201651491  0.5000933873665332  0.3128480737465154
0.2022854501384330  0.5000686696270193  0.2366363310640125
0.1826826673506829  0.0000478973459010  0.1599514194914278
0.1949339836505786  0.5000214981021003  0.0683297848739883
0.4160677942492583  0.0000901142839425  0.3055335535651835
0.5136416202622343  0.5000844537556830  0.2690563404465109
0.6105452270331710  0.0000778434534041  0.2064733062026534
0.6973266142214172  0.5000532211488107  0.1236357623665469
0.7650950847862461  0.0000344416088467  0.0286964425642751
0.8067388306642229  0.5000187263874949  0.9309400739388991
0.8185125597869742  0.9999922465254230  0.8395361877630307
0.7987480554184572  0.4999718691748427  0.7634748786246206
0.7492740065683776  0.9999511945251882  0.7108216927405806
0.6756984375234936  0.4999429974787901  0.6870073224369904
0.5857283865527165  0.9999428942166162  0.6939589917366931
0.4876343163762868  0.4999443227102844  0.7305789502648068
0.3905232223183006  0.9999504884345640  0.7935228503093086
0.3040809734799907  0.4999823720228207  0.8764144180255471
0.2368056977223532  0.0000040064236302  0.9709818446001535
```

The first line is treated as a comment line, usually used for the name of the system. The second line provides a universal scaling factor, which is used to scale all lattice vectors and all atomic coordinates. The next three lines are the three lattice vectors defining the unit cell of the system. The fifth line supplies the number of atoms per atomic species in a same order as the included atomic species in POTCAR file. An optional tag of Selective Dynamics can be used in the sixth line to allow for a selective atom relaxation. If this tag is omitted, the sixth line supplies the switch between cartesian and direct lattice. The direct

coordinates is used in the POSCAR file. The next lines give the three coordinates for each atom.

B.1.3 The POTCAR File

The POTCAR file contains the pseudopotential for each atomic species used in the calculation. VASP is supplied with a set of standard pseudopotential. All supplied PP's with VASP are of the ultra soft type. If the number of species in the system is larger than one, a UNIX command can be used to combine the POTCAR of each species into one POTCAR file. The Pd fully coated SWNT(10,0) system's POTCAR file is made by cat command:

```
> cat POTCAR_C POTCAR_Pd >POTCAR
```

Note that the order of each species in the POTCAR file has to be consistent with that in the POSCAR file.

B.1.4 The KPOINTS File

The file KPOINTS must contain the k-point coordinates and weights or the mesh size for creating the k-point grid. The k-mesh can be either entered by hand or generated automatically. In our simulations, Monkhorst-pack grid is used to sample the Brillouin zone. The KPOINT file is like below:

```
Monkhorst pack
0
Monkhorst Pack
 1   1   31
 0   0   0
```

The First line is treated as a comment. The zero on the second line activates the automatic generation scheme. The automatic scheme is selected by the third line. The fourth line

defines the numbers of subdivisions along each reciprocal vector. The last line is optional and supplies an additional shirt of k-mesh. An zero indicates no shift.

B.2 The Output Files

VASP can generate more than ten different output files, but only some are used in this dissertation for electronic property calculations. For example, DOSCAR, CHGCAR, OUTCAR and EIGENVAL files. DOSCAR contains the DOS and integrated DOS. CHGCAR provides the total charge on the FFT-grid. OUTCAR contains information of self-consistent iterations, such as force, energy, stress, etc. EIGENVAL saves Kohn-Sham eigenvalues for all k-points at the end of the simulation.

B.3 Calculate Band Structure

To calculate the band structure, CHGCAR file from a previous self-consistent run is needed as an input file. The INCAR file is slightly different from that for the ground state energy calculation as shown in the beginning of this chapter, because the following tag is needed.

```
ICHARG = 11
```

Thus the charge density will be kept constant during the electronic minimization. The KPOINTS file also needs to be modified to generate strings of k-points connecting specific points of Brillouin zone. The KPOINTS used for band structure calculation for the Pd functionalized SWNT(10,0) is shown below, where the third line must start with an L for the line-mode calculation.

```
k-points along high symmetry lines
20
```

```
Line mode
rec
0.00000  0.00000  0.00000
0.00000  0.00000  0.50000
```

According to this KPOINTS file, VASP will generate 20 k-points between the first and second supplied high symmetry k-points defined in the fifth and sixth lines. These k-points are supplied in reciprocal coordinates by using a rec in the fourth line. More interested k-points can be added in pair in the end of the file for calculations of band structure along other lines. After running VASP using the modified INCAR, KPOINTS together with the CHGCAR, POTCAR and POSCAR, an EIGENVAL file that has all the needed information for band structure plot will be generated. The format of EIGENVAL file can be found in the VASP manual. A program called P4VASP can be utilized for processing the EIGENVAL file and for viewing the band structure.

About the Author

Ling Miao was born in Shanghai, China. She attended Shanghai Kongjiang middle and high school from 1989 to 1996. She studied her Bachelor's degree in Chemical Engineering at Shanghai University from 1996 to 2000, where she was awarded the outstanding student scholarship as one of best students in the university for four continuous years. After that she worked with Professor Zhu on green technology optimum for benzaldehyde production in the Chemical Engineering Department and completed her Master's Degree of Applied Chemistry in 2002.

She began pursuing her Ph.D. degree in the Chemical Engineering Department at University of South Florida in 2002. During the study in USF, She presented her work in many conferences and she won one grand price and two honorable mention awards. She has one paper published in Physical Review B and one accepted in Journal of Physical Chemistry B before completing this dissertation.